2016

Development of new electrode materials for lithium ion batteries and lithium oxygen batteries

Jun Wang
University of Wollongong, jw707@uowmail.edu.au

UNIVERSITY OF WOLLONGONG

Institute for Superconducting & Electronic Materials

Development of New Electrode Materials for Lithium Ion Batteries and Lithium Oxygen Batteries

Jun Wang

This thesis is presented as part of the requirements for the

Award of the Degree of Doctor of the Philosophy

University of Wollongong

February 2016

CERTIFICATION

I, Jun Wang, declare that this thesis, submitted in partial fulfilment of the requirements for the award of Doctor of Philosophy, in the Institute for Superconducting & Electronic Materials (ISEM), Faculty of Engineering, University of Wollongong, NSW, Australia, is wholly my own work unless otherwise referenced or acknowledged. This thesis has not been submitted for qualifications at any other academic institutions.

Jun Wang

February 2016

ACKNOWLEDGEMENTS

It is my pleasure to convey my gratitude to my supervisors, Prof. Huakun Liu, Prof. Jiazhao Wang, and Dr. Shulei Chou, for their continuous support, patience, academic guidance, and great encouragement in various ways during my PhD studies in the Institute for Superconducting & Electronic Materials (ISEM) at the University of Wollongong (UOW), Australia.

I would like to acknowledge the Chinese Scholarship Council (CSC) for the living allowance scholarship for my PhD study in ISEM. I would also like to acknowledge the University of Wollongong for providing a Free Tuition Scholarship for me during my PhD study.

I also would like to thank Prof. Chuanqi Feng (Hubei University) for his important contributions in the publications on which we collaborated during my PhD study. Special thanks should be given to Dr. Tania Sliver for critical reading of manuscripts and Mrs. Narelle Badger for her help in official matters.

Technical assistance from Dr. Gilberto Casillas (TEM), Dr. Patricia Hayes (Raman spectroscopy), Dr. Dongqi Shi (XPS), Dr. Germanas Peleckis (XRD), Dr. Konstantin Konstantinov (TGA and BET), Dr. Tony Romeo (FE-SEM), and Mr. Robert Morgan (technical staff) is highly appreciated.

Dr. Qi Li, Dr. Chao Zhong, Dr. Xuanwen Gao, Dr. Zhijia Zhang, Dr. Zidong Zhang, Dr. Yi Shi, Mrs. Xin Liang, Dr. Yunxiao Wang, Dr. Jiantie Xu, Ms. Weijie Li, Mr. Yuede

Pan, Mr. Wenbin Luo, Mr. Mohammad Rejaul Kaiser, Mr. Zhixin Tai, Ms. Lili Liu, Mr. Boyang Ruan, Mr. Yuyang Hou, Mrs. Fang Li, Mr. Haipeng Guo, Mr. Zhe Hu, Mr. Weihong Lai, Mr Mingzhe Chen, and other staff members and students in ISEM also deserve thanks, for their kindly help and willingness to share knowledge with me during this research.

I would like to express special thanks to my dearest friend Miss Lanling Zhao, especially for her moral support during the whole period of my PhD and for always being there whenever I needed her.

I would like to express my gratitude to my parents for their constant support and love throughout my life. I would never have gone so far without their selfless dedication and unwavering belief.

Finally, I would like to thank everyone who was important to the success of my PhD study in the University of Wollongong. This thesis is dedicated to them.

ABSTRACT

Lithium-ion batteries (LIBs) have been widely used as the power sources for a wide range of portable electronic devices, such as cell phones, laptops, and digital cameras, since their first commercialization in the 1990s. In recent years, enormous ongoing efforts have been made to develop the next generation of LIBs, which feature thinner, smaller sizes, lighter weight, flexibility, higher capacity and rate capability, and longer cycle life. Advanced electrode materials are the key to realizing this goal. High performance anode materials are the key to one of the most important components in LIBs, and they thus have attracted much research attention. In this thesis, nanosized materials, including free-standing germanium (Ge) and single-walled carbon nanotube (SWCNT) composites, as well as lead germanate/graphene nanosheet ($PbGeO_3$/GNS) composites, were prepared and characterized for possible applications as anode materials for LIBs.

Electric vehicles and large-scale applications for renewable energy storage require electrochemical systems with much higher energy density than what can be provided by the most advanced LIBs available today. Li-O_2 batteries (LOBs) are regarded as a promising alternative due to their extraordinarily large theoretical specific energy density of about 11140 Wh kg^{-1}, which is several times higher than that of the LIBs and even close to that of a gasoline energy system. The practical application of LOBs, however, has been inhibited by several severe problems, including high overpotentials, low capacity, low rate capability, and short cycle life, which are mainly caused by the sluggish dynamics of the cathode material during the Li_2O_2 formation and decomposition. Therefore, efficient cathode catalysts, which could offer excellent catalytic activity toward both the oxygen reduction reaction (ORR) and the (oxygen evolution reaction)

OER are highly sought after. In this thesis, graphene nanosheets (GNS)/ manganese dioxide (MnO_2) composites and palladium/porous nitrogen-doped carbon-nanofiber (Pd/PNCNF) composites were synthesized and studied as cathode catalysts for LOBs.

Paper-like free-standing Ge/SWCNT composite anodes for LIBs were synthesized by the vacuum filtration of Ge/SWCNT composites, which were prepared by a facile aqueous-based method. Electrochemical measurements demonstrated that the Ge/SWCNT composite paper anode for LIBs with a Ge weight percentage of 32% delivered a specific discharge capacity of 417 mAh g^{-1} after 40 cycles at a current density of 25 mA g^{-1}, 117% higher than that of the pure SWCNT paper anode. The SWCNTs not only function as a flexible mechanical support for strain release, but also provide excellent electrically conducting channels, while the nanosized Ge particles contribute to improving the discharge capacity of the paper anode.

$PbGeO_3$/GNS composites have been prepared by an efficient one-step, in-situ hydrothermal method and were used as anode materials for LIBs. The $PbGeO_3$ nanowires, around 100-200 nm in diameter, are highly encapsulated in a graphene matrix. Compared with pure $PbGeO_3$ anode, dramatic improvements in the electrochemical performance of the composite anodes have been obtained. In the voltage window of 0.01-1.50 V, the composite anode with 20 wt.% GNS delivers a discharge capacity of 607 mAh g^{-1} at 100 mA g^{-1} after 50 cycles. Even at a high current density of 1600 mA g^{-1}, a capacity of 406 mAh g^{-1} can be achieved. Therefore, the $PbGeO_3$/GNS composite can be considered as a potential anode material for LIBs.

MnO_2 as cathode catalyst material for LOBs has been intensively studied, and GNS is considered to be an effective support to improve the electrocatalytic property of the cathode. GNS have been synthesized using a fast and effective microwave autoclave method, in which MnO_2 nanoflakes are coated on the GNS in situ to form a composite material. Compared with pure GNS cathode, dramatic improvements in the catalytic performances of the composite cathode have been obtained. The GNS not only increase the electrical conductivity of the composite cathode, but also offer enough space for the tri-phase reaction and for buffering the volume changes during cycling. The MnO_2 nanoflakes with intrinsically high catalytic activity could efficiently boost the oxygen reduction reaction and oxygen evolution reaction, improving the electrocatalytic performance of the MnO_2/GNS composite as cathode for LOBs.

Pd/PNCNF composites with a three-dimensional network structure have been prepared by decorating Pd nanoparticles onto the PNCNFs, which were derived from KOH activated polypyrrole nanofibers. The Pd nanoparticles decorated on the walls of the PNCNFs as a bifunctional catalyst can play a key role in the ORR and the OER, as evidenced by the electrochemical results in aqueous solution. With the synergistic effects from the PNCNF matrix with a highly conductive porous structure and the Pd nanoparticles with high electrocatalytic performance, a LOB containing the Pd/PNCNF composite catalyst with 25 wt.% Pd nanoparticles showed notably improved electrocatalytic performance compared to a cell containing its pure PNCNF counterpart, with higher capacities, lower overpotentials, and better cycling stability. Therefore, the Pd/PNCNF composite is proposed as a potential cathode catalyst for LOBs.

TABLE OF CONTENTS

LIST OF FIGURES

LIST OF TABLES

LIST OF ABBREVIATIONS

Abbreviation	Full name
3D	Three-dimensional
APS	Ammonium peroxydisulfate
a.u.	Arbitrary unit
BET	Brunauer Emmett Teller
CCD	Charge-coupled device
cm	Centimeter
CMC	Carboxymethyl cellulose
CNFs	Carbon nanofibers
CNTs	Carbon nanotubes
CTAB	Cetyltrimethylammonium bromide
CV	Cyclic voltammetry
DEC	Diethyl carbonate
EC	Ethylene carbonate
EDS	Energy dispersive X-ray spectroscopy
EIS	Electrochemical impedance spectroscopy
EV	Electric vehicle
FE-SEM	Field emission scanning electron microscopy
FTIR	Fourier transform infrared spectroscopy
GC	Glassy carbon
GNS	Graphene nanosheets
GO	Graphene oxide
HEV	Hybrid electric vehicle

HRTEM	High-resolution transmission electron microscopy
JCPDS	Joint Committee on Powder Diffraction Standards
LIBs	Lithium-ion batteries
LOBs	Lithium-oxygen batteries
LSV	Linear sweep voltammograms
M	Metal element
mm	Millimeter
nm	Nanometer
OER	Oxygen evolution reaction
ORR	Oxygen reduction reaction
PPy	Polypyrrole
PTFE	Poly(tetrafluoroethylene)
PVDF	Polyvinylidene fluoride
Py	Pyrrole
RDE	Rotating disk electrode
SAED	Selected area electron diffraction
SEI	Solid electrolyte interphase
SEM	Scanning electron microscopy
SHE	Standard hydrogen electrode
STEM	Scanning transmission electron microscope
SWCNTs	Single-walled carbon nanotubes
TEGDME	Tetraethylene glycol dimethyl ether
TEM	Transmission electron microscopy
TGA	Thermogravimetric analysis

XPS	X-ray photoelectron spectroscopy
XRD	X-ray diffraction

LIST OF SYMBOLS

Symbol	Name	Unit
ΔG	Gibbs free energy	kJ mol^{-1}
ΔH	Enthalpy	kJ mol^{-1}
2θ	Detection angle in XRD	Degree
C-rate	Charge or discharge rate	mA g^{-1}
D	Diffusion coefficient	m s^{-1}
d	Lattice spacing	nm
E^0	Standard electrode potential	V
ED	Energy density	Wh kg^{-1} or Wh L^{-1}
F	Faraday's constant = 96485	C mol^{-1}
I	Current	A
N	Avogadro's number = 6.022×10^{-23}	mol^{-1}
^oC	Degrees Celsius	-
P	Pressure	Pa
P_0	Saturation pressure	Pa
PD	Power density	W kg^{-1} or W L^{-1}
Q_s	Specific capacity	mAh g^{-1} or mAh cm^{-3}
R_{ct}	Charge transfer resistance	Ω
T	Temperature	K or °C
t	Time	h or s
V_{oc}	Open circuit voltage	V
W	Warburg impedance	Ω
wt.%	Weight percent	-

Z_{re}	Real part of the impedance	Ω
Z_{w}	Warburg impedance	Ω
η_{e}	Coulombic efficiency	%
λ	Wavelength	Å
σ	Ionic conductivity	S cm^{-1}

LIST OF ORGANIZATIONS

Abbreviation	Full name
CSC	China Scholarship Council
ISEM	Institute for Superconducting and Electronic Materials
UOW	University of Wollongong

CHAPTER 1 INTRODUCTION

Currently, with the rapid increasing worldwide need for energy, fossil fuels, such as petroleum, coal, and natural gas, are being exploited on an enormous scale, while their consumption could lead to severe environmental pollution caused by the gas emissions[1, 2]. Moreover, the amounts of these non-renewable resources are limited, so that we will have to face energy supply problems in the future. Renewable energy sources, such as solar power, wind power, tidal power, and hydropower, have been considered as promising alternatives to substitute for fossil fuels[3]. These renewable energy sources, however, could be achieved depending on the natural conditions. Therefore, the choice of power storage systems is very important.

Batteries can efficiently convert chemical energy into electrical energy and have been proved to be the best system for efficient energy utilization up to the present. Lithium-ion batteries (LIBs) have aroused the most interest with an entire range of commercialized batteries and have dominated the market for batteries to power portable electric devices[4, 5]. This is because they have many advantages compared to other battery systems, including high energy density of up to 180 Wh kg^{-1}, high working voltage of around 3.6 V, and longer charge retention or shelf life (up to 5-10 years)[6, 7]. Rapid advances in electronic technology have provided the driving force for developing wearable and roll-up devices. Flexible batteries featuring ultra-thinness, light weight, small size, and flexibility are highly desired for related applications, such as bendable devices, active radio-frequency identification tags, integrated circuit smart cards, and implantable medical devices[8]. Furthermore, LIBs have also been proposed to serve as the power sources for large electrical applications especially in electric vehicles (EVs) and hybrid electric vehicles (HEVs)[9, 10]. Their theoretical and practical battery performances,

however, could make them the ideal candidate energy storage system for HEVs, but they are not enough for EVs. Lithium-O_2 batteries (LOBs) are believed to be the best choice for EVs, because they could deliver a theoretical specific energy of 11140 Wh kg^{-1}, which is close to that of the gasoline system[11, 12]. Such high energy density is enough for one long-distance drive employing EVs.

In order to develop next-generation batteries, much more efforts are needed. Typically, both LIBs and LOBs are composed of four main parts, the electrode, electrolyte, binder, and separator. Among these, the electrode significantly determines the battery's electrochemical performance. The current research interest put into advanced materials for LIBs and LOBs could be categorized in terms of the following directions: (1) searching for novel electrode materials for flexible LIBs and high performance LIBs, (2) developing new catalyst materials for LOBs, and (3) improving the electrochemical performance of batteries by applying various electrode material treatments, such as formation of different morphologies, doping with different elements, preparing composites, etc. Therefore, in this thesis, I have mainly focused on developing new anode materials (free-standing and conventional) for LIBs, novel cathode catalyst material for LOBs, and extending our understanding of the dependence of their electrochemical performance on their morphology and structure.

A brief overview of the chapters in this thesis:

Chapter 1 introduces the general background, major problems, some approaches for improving the electrochemical performance of LIBs and LOBs, and the objectives of this study.

Chapter 2 presents a literature review on LIBs and LOBs, including the history of batteries, general principles, basic concepts, and the recent research and development in these areas.

Chapter 3 includes the list of materials used in this thesis, as well as the experimental procedures, synthesis methods, electrode preparation, coin-cell assembly, and physical and electrochemical characterization techniques.

Chapters 4 and 5 investigate the influence of structure, composition, and morphology on the electrochemical performance of two Ge anode materials for LIBs, Ge/SWCNT and $PbGeO_3$/GNS, respectively.

Chapters 6 and 7 discuss the influence of the structure, composition, and morphology on the electrochemical performance of two cathode materials for LOBs, MnO_2/GNS and Pd/PNCNF, respectively.

Chapter 8 contains the general conclusions of this thesis and recommendations for further research based on them, followed by the lists of references and publications during the period of this study.

CHAPTER 2 LITERATURE REVIEW

2.1 Lithium-Ion Batteries

2.1.1 General Background

The development of energy storage and conversion systems has attracted great attention from researchers and companies over the last several decades. Li-ion batteries (LIBs) are highly stable and efficient devices, and they still remain the major energy sources for mobile and portable electronic applications, such as power tools, mobile phones, laptop computers, and cameras. Li is the most electropositive and the lightest metal, with electrochemical potential of -3.04 V (vs. standard hydrogen potential, SHE) and molecular weight of 6.94 g mol^{-1} (specific gravity ρ = 0.53 g cm^{-3}), respectively. Therefore, LIBs deliver energy density 2-3 times higher and power density 5-6 times higher than those of nickel metal hydride (Ni-MH), Ni-Cd, and Pb acid batteries[13].

There are many other advantages of LIBs, mainly including high operating voltage (around 3.6 V), low self-discharge, long cycle life (> 1000 cycles), and no "memory effect"[10]. Although commercial LIBs are widely used, the commercial LIBs still cannot meet all the demands of our society. Advanced LIBs with high performance are actually needed for portable electronic applications with shorter charging time and longer service life, and for expanded applications including power grid storage and electric vehicles (EVs).

2.1.2 Brief History

Figure 2.1 shows the historical timeline for batteries[14], indicating that the first modern electrochemical cell was fabricated by Alessandro Volta in 1800. Afterwards, many kinds

of primary or rechargeable batteries were developed over the centuries, mainly including the lead-acid batteries, Ni-metal batteries, and alkaline batteries. In the 1970s, primary Li batteries were commercialized and are still in use today because of their high capacity and rate capability. In the same period, Whittingham and his co-workers developed Li batteries using titanium (IV) sulfide (TiS_2) as cathode and Li metal as anode [15]. In 1979, the Goodenough group investigated a series of Li_xMO_2 (M = Co, Ni, Mn) compounds as cathode materials, in which Li ions could be inserted and de-inserted electrochemically [16]. In 1981, a Sanyo patent described the reaction mechanisms of Li intercalation in graphite, which has significantly reduced the safety risk of pure Li anode in the batteries[17]. Finally, the first commercial LIBs were fabricated by the SONY Corporation in 1991, using $LiCoO_2$ as cathode and graphite as anode. They could deliver energy densities of 120-150 Wh kg^{-1} with an operational voltage of 3.6 V. From then on, many types of electrode materials have been widely studied as alternatives to $LiCoO_2$ cathode and graphite anode, and the battery performance has been greatly improved. During the past two decades, LIBs have dominated the battery community all over the world and become the first choice among the energy sources for portable electronic devices.

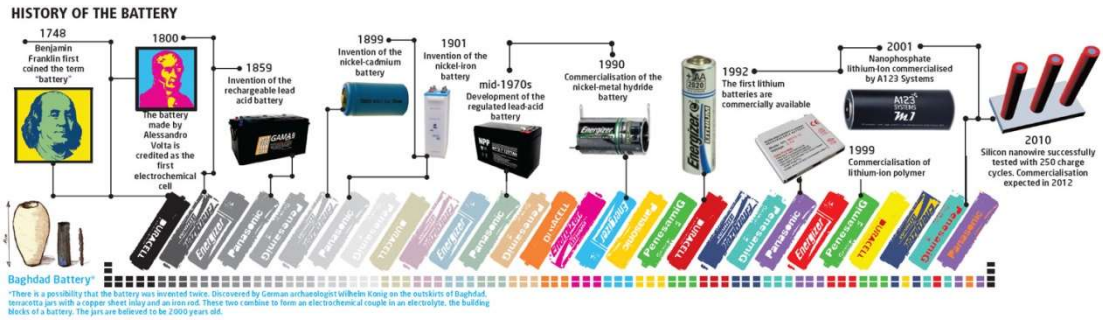

Figure 2.1 Schematic representation of battery development over the centuries[14].

2.1.3 General Principles

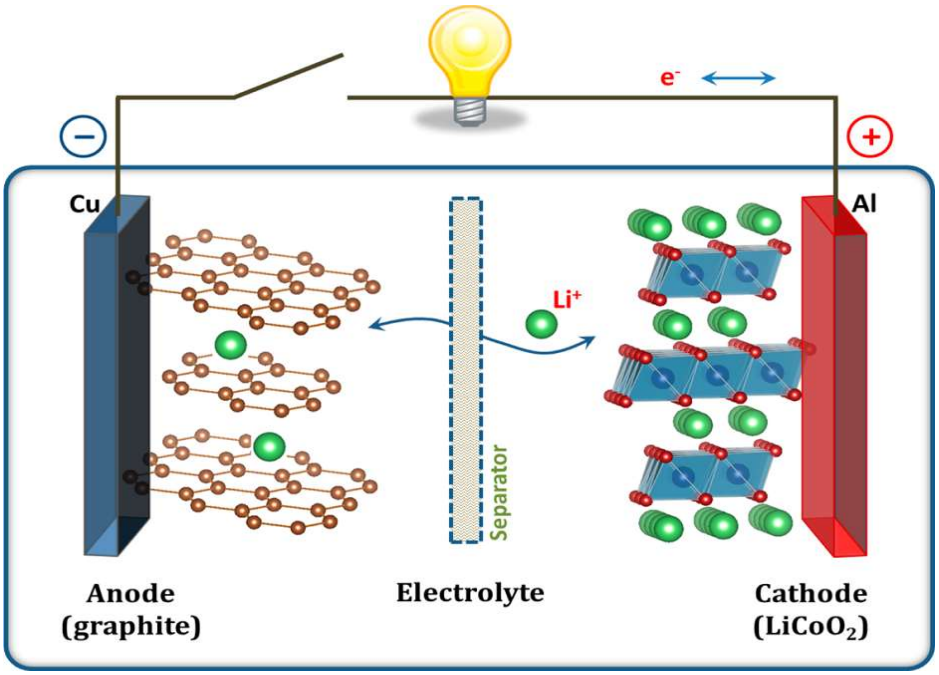

Figure 2.2 Schematic illustration of principles of a rechargeable LIB [18].

A LIB mainly contains four essential components, namely, the anode, the electrolyte, the separator, and the cathode. The LIB is referred to as a rocking-chair battery, because Li ions "rock" back and forth between the anode and the cathode during cycling. A conventional LIB with graphite anode and $LiCoO_2$ cathode is taken as an example in Figure 2.2. Li ions are transferred from the $LiCoO_2$ cathode to the graphite anode through the electrolyte/separator in the charge process and go back again in discharge process. This can enable the conversion of chemical energy into electrical energy, which is stored within the battery. The reaction mechanism is listed in the following reactions:

Cathode $LiCoO_2 \leftrightarrow Li_{1-x}CoO_2 + xLi^+ + xe^-$ (2.1)

Anode $6C + xLi^+ + xe^- \leftrightarrow Li_xC_6$ (2.2)

Overall $LiCoO_2 + 6C \leftrightarrow Li_{1-x}CoO_2 + Li_xC_6$ (2.3)

2.1.4 Basic Concepts

In order to better understand the LIB system, some general concepts are discussed below:

Open circuit voltage (V_{OC}) is the voltage recorded across the terminals of a cell without external current flow. It is normally close to the system thermodynamic voltage and determined by the difference in electrochemical potential between the anode and the cathode.

$$V_{OC} = \frac{(\mu A - \mu C)}{(-n\ )} \tag{2.4}$$

where μA, μC, n, and F are the anode electrochemical potential, the cathode electrochemical potential, the number of electrons involved, and the Faraday constant (96485 C mol^{-1}), respectively.

Operating voltage can be described as:

$$V = V_{OC} - IR \tag{2.5}$$

where I and R are the current and the internal resistance of the cell, respectively.

Capacity (Q) is the total amount of charge on the electrode in the battery for the redox reaction during the discharge/charge.

$$Q = \int_{t1}^{t2} I(t)dt = nzF \tag{2.6}$$

where t, $I(t)$, n, z, and F are the time, the current, the number of ions (mol), the valence of the ions, and the Faraday constant, respectively.

Specific capacity (Q_s) for the charge or the discharge process can be described in terms of gravimetric specific capacity (mAh g^{-1}) or volumetric specific capacity (mAh cm^{-3}). The specific capacity is calculated according to the capacity per unit weight of the active material, or capacity per unit density of the active material.

Irreversible capacity is attributed to the irreversible Li reactions of the active materials during intercalation and deintercalation processes. It is the difference between the charge capacity and the discharge capacity for the *n*th cycle.

Coulombic efficiency (η_e) equals the ratio of the charge capacity to the discharge capacity for the *n*th cycle.

Capacity retention can be calculated from the ratio of the discharge capacity of the last cycle to that of the initial cycle.

Energy density can be described in gravimetric (Wh kg^{-1}) or volumetric (Wh L^{-1}) terms. It is used to compare the energy content between cells.

Power density can be described in gravimetric (W kg^{-1}) or volumetric (W L^{-1}) terms. It is used to assess the rate capability of the cell.

The charge/discharge rate or C-rate is utilized to evaluate how fast Li ions can be transferred. C represents either the theoretical capacity or the nominal capacity of a cell. For example, 0.5 C means fully charging/discharging in 2 hours.

2.1.5 Cathode Materials

Research on cathode materials for LIBs has aroused a great deal of interest since the advent of the commercial LIBs in 1991. Generally, most of the cathode materials are Li-based intercalation compounds, serving as the Li source in the battery, because the anode material is free of Li. $LiCoO_2$ is the most widely employed material in commercial LIBs with a capacity of 140 mAh g^{-1}, and deintercalating and intercalating Li around 4 V. $LiCoO_2$, however, has certain disadvantages including high cost, toxicity, limited capacity, and low working voltage, which could restrict its further development. Therefore, efforts have been paid to explore new cathode materials with high electrochemical performance.

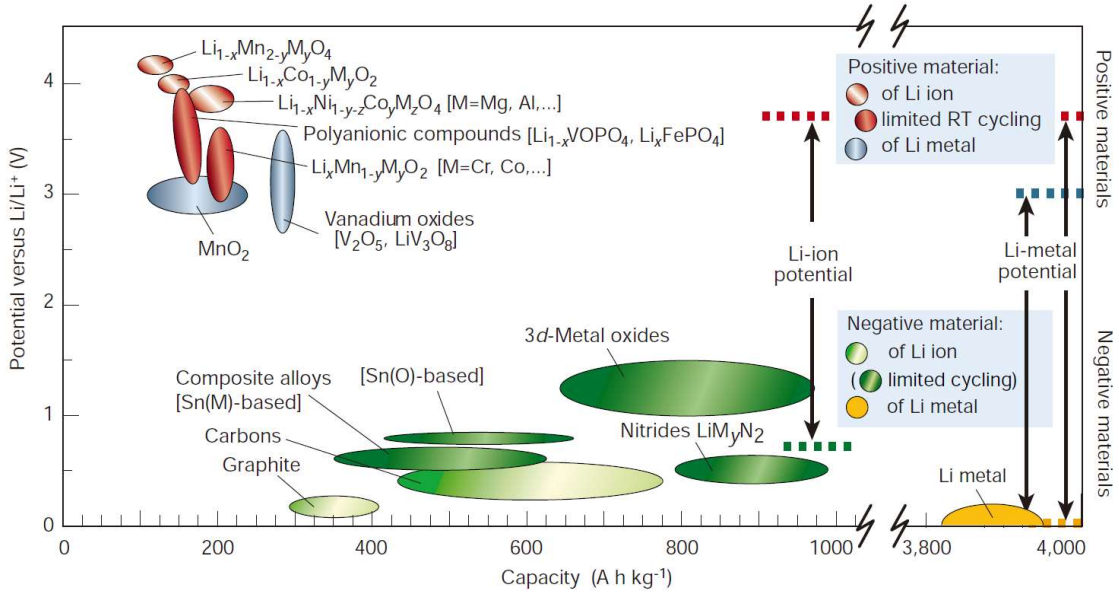

Figure 2.3 Voltage versus capacity for cathode and anode materials in the current LIB technologies[13].

To date, there are three major types of cathode materials for LIBs involving layered, spinel, and olivine structured oxides[13], as can be seen in Figure 2.3. Among them, transition metal oxides such as $LiNiO_2$ and $LiMnO_2$, using cationic doping to stabilise their layered structured framework, could deliver capacity of up to 200 mAh g^{-1}, which is almost 50% higher than that of $LiCoO_2$. Moreover, spinel type transition metal oxides such as $LiMn_2O_4$ have also attracted much attention as a green alternative, although they could only deliver a slightly lower capacity of 120 mAh g^{-1}. Furthermore, Li-free V_2O_5 and its derivatives have also been used in rechargeable Li solid polymer electrolyte batteries and exhibit favourable performance. In addition, polyoxyanionic compounds with olivine structure such as $LiFePO_4$ (170 mAh g^{-1}) are also considered to be promising alternatives, and have been commercialised by A123 Systems. Apart from these cathode materials, Li-excess layered oxides have also been intensively studied due to their high capacity potential[19, 20].

2.1.6 Anode Materials

Li metal was chosen to be the anode material in the early stages of the LIB development during the 1970s and early 1980s, mainly because it could offer a high specific capacity. There is severe safety problem, however, if we take its inflammable property into consideration. Moreover, dendrites are easily formed during cycling in Li batteries, and they could penetrate the separator, resulting in a short circuit[21, 22]. Graphitic carbon as anode material was introduced at the end of the 1980s[23]. Since then, this kind of material has attracted much attention, and it is used as the main anode material in the commercial LIBs. With the increasing demand for LIBs with high power density and energy density, alternative anode materials are urgently required and need to be developed to improve the

Li ion diffusion rate and the specific capacity. Promising anode materials mainly include carbonaceous materials, alloy materials, metal oxides, and metal sulphides, which will be also introduced in detail in the following sections.

2.1.6.1 Carbonaceous Materials

Carbon is one of the most common material on earth, and it has many allotropes mainly including graphite, fullerene, carbon nanotubes, and graphene[24, 25], as shown in Figure 2.4. Among these, graphite, carbon nanotubes, and graphene nanosheets have been intensively studied and have proved to be very promising anode materials for LIBs.

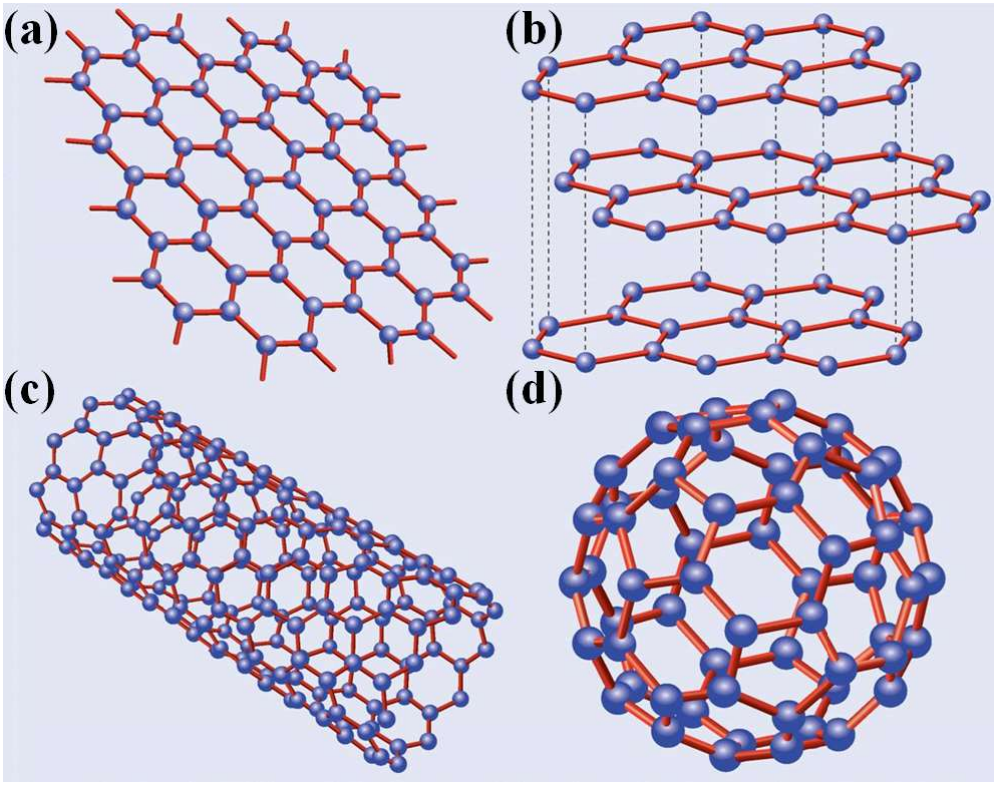

Figure 2.4 Typical allotropes of carbon: (a) graphene, (b) graphite, (c) carbon nanotube, and (d) buckminsterfullerene[26].

Graphite was commercialised by Sony in the early 1990s and still dominates the Li-ion market even now. During cycling, Li could be reversibly intercalated and de-intercalated between the interlayers of graphite, with a low discharge voltage plateau of around 0.1 V (vs. Li^+/Li). When forming LiC_6 compound, the voltage plateau could be close to that of metallic Li. Although the employment of graphite anode obviously reduces the safety risk compared with that of Li anode in the LIBs, it can only deliver a low theoretical capacity of 372 mAh g^{-1}. In addition, the diffusion coefficient of Li ions in graphite is less than 10^{-6} cm^2 s^{-1}, which leads to a low power density[27].

Carbon nanotubes (CNTs) can be classified as single-walled carbon nanotubes (SWCNTs), double-wall carbon nanotubes (DWCNTs), and multi-walled carbon nanotubes (MWCNTs). They possess large surface activity and high surface-to-volume ratios, with their diameters less than 100 nm. The specific capacity of CNT anode have been determined experimentally to have values from 400 - 1000 mAh g^{-1}[28], much higher than that of the graphite anode. This is mainly because Li could be stored between the pseudo-graphitic layers of CNTs. It is believed that strain could be induced on the planar bonds of the carbon hexagons due to the small diameters of CNTs, and this results in electron de-localization and a more electronegative structure compared to that of the regular carbon sheets, which enhances the degree of Li insertion[29]. Recently, enormous research efforts have been devoted to developing soft, ultra-thin, and lightweight small batteries as a further development of modern LIBs. CNTs have been considered to be one of the most suitable candidate materials to prepare free-standing anode, which is free of the need for binders and current collectors[30, 31]. The energy density of the CNT anode is limited, however, due to the low practical capacity and high irreversible charge loss caused by the formation of a solid electrolyte interface (SEI) and other side reactions[32].

Introducing metal or metal oxide onto the walls of the CNTs could greatly enhance the electrochemical performance of this anode material. By forming composites of CNTs with second phase particles, the electrical conductivity of the anode material can be enhanced significantly, which ensures good electron transport and efficient electrochemical reactions in the anode material. Furthermore, CNTs could inhibit the volume expansion and aggregation of the anode material during cycling, relieving the pulverization and exfoliation problems which lead to degradation of the cycling performance.

Graphene nanosheets (GNS) were first prepared utilizing by adhesive tape technique by Andre Geim and Konstantin Novoselov who won the Nobel Prize in 2004 [33]. Graphene can be described as a single atomic layer of carbon in a two-dimensional honeycomb lattice. Due to its extraordinary electrical conductivity, high surface area, good mechanical properties, and chemical stability, GNS have attracted considerable attention from researchers in different fields[34, 35]. A simple oxidation method was applied by Hummers in 1958 to synthesize graphene oxide (GO) from graphite[36], laying the foundation for large-scale production of GNS. The theoretical specific capacity of GNS as an anode material for the LIB is 744 mA h g^{-1} when Li is stored on both sides of the GNS, forming LiC_3 structures. Wang's group fabricated GNS with 2-3 layers in 2009, and the anode containing them could deliver a specific capacity of 650 mAh g^{-1}[37]. In fact, GNS are also used as a matrix combined with metals or metal oxides to achieve improved cycling stability and rate capability[38, 39]. Apart from enhancing the electrical conductivity and mitigating volume expansion and aggregation of the anode material, GNS could be restacked by the distribution of second phase particles between them.

Therefore, high active surface areas could be achieved with more disorder/defects and cavities for Li storage.

2.1.6.2 Alloy Materials

In 1971, Li metal was demonstrated to be electrochemically alloyed with metallic material in an electrochemical system with an organic electrolyte [40]. From then on, Li-alloying reactions with metallic or semimetallic elements have been widely studied to search for alternative materials to carbon as anode in LIBs. The reversible reaction is presented in the following equation, where M is a metal:

$$Li_xM \leftrightarrow M + xLi^+ + xe^- \quad (2.7)$$

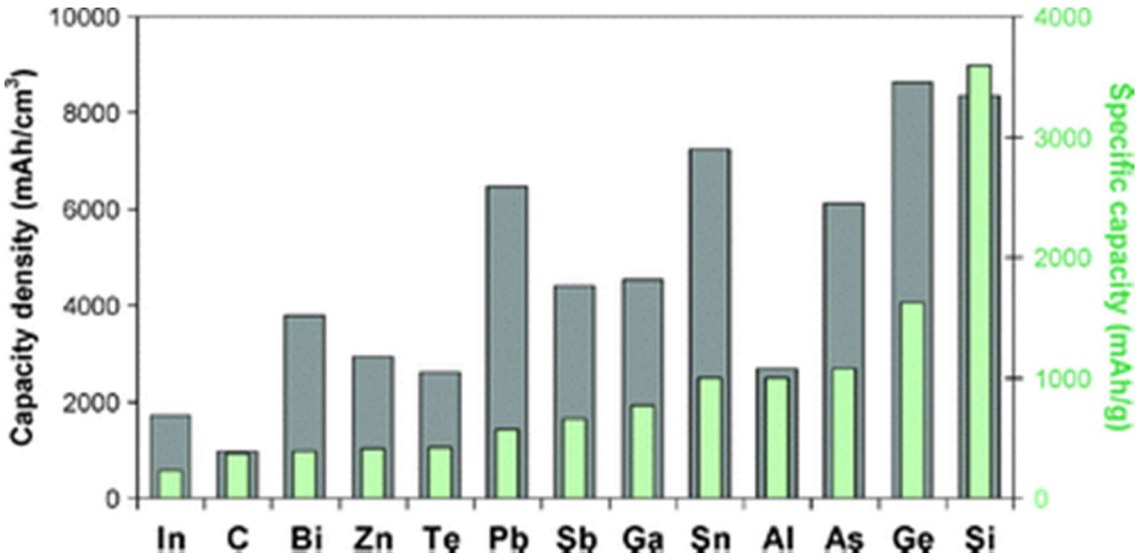

Figure 2.5 Specific densities and capacities for selected alloying reactions[41].

In Figure 2.5, specific densities and capacities for typical materials are listed, and those of the graphite are also included as a reference[41]. As can be seen in the Figure, Si, Ge,

and Sn show superior specific capacities and thus have been regarded as promising anode materials for LIBs.

Sn can be alloyed with Li to form Li_2Sn_5, LiSn, Li_7Sn_3, Li_5Sn_2, $Li_{13}Sn_5$, Li_7Sn_2, and $Li_{22}Sn_5$, based on research on Sn lithiation at elevated temperatures[42]. $Li_{17}Sn_4$ is the actual phase present, and it is believed that Sn could deliver a theoretical capacity of 959.5 mAh g^{-1}, which is about 3 times higher than that of graphite. Its reaction voltage is about 0.5 V vs. Li/Li^+ with several plateaus, which demonstrate the formation of different Li-Sn phases. The volumetric capacity of Sn is around 2000 mAh cm^{-3}, making it a promising anode material, although it has less gravimetric capacity compared to Si and Ge.

Si is another suitable candidate anode material because of its high natural abundance, low cost, and environmental friendliness. It possesses the highest volumetric capacity among the various elements of 8334 mAh cm^{-3} and gravimetric capacity of 4200 mAh g^{-1}, based on $Li_{22}Si_5$[43]. Its alloying with Li passes through $Li_{12}Si_7$, Li_7Si_3, and $Li_{13}Si_4$, to $Li_{22}Si_5$. Its reaction voltage is as low as 0.4 V vs. Li/Li^+, making it easier to assemble cells to work at high voltages[44]. Nevertheless, fully lithiated Si experiences a volume change of 400% in the discharge processes, leading to loss of electrical contact in the anode and thus poor electrochemical performance.

Ge anode have received increasing attention in recent years, because it could deliver a high theoretical volumetric capacity of 7366 mAh cm^{-3} and gravimetric capacity of 1600 mAh g^{-1} by the formation of $Li_{22}Ge_5$ phase[45]. Compared with the well-studied Si, Li ion diffusivity in Ge is 400 times higher, thus offering superior rate performance. Moreover, electron transport in Ge is much faster than in Si, resulting in 104 times higher electrical

conductivity than that of Si[46, 47]. Additionally, the Ge surface is less easily oxidised when exposed to air, unlike the Si surface. In the process of Li intercalation, two obvious potential plateaus can be found, which implies the formation of different Li-Ge intermetallic phases, including Li_9Ge_4, Li_7Ge_2, $Li_{15}Ge_4$, and $Li_{22}Ge_5$ in sequence. Similar to Si anode, Ge anode also displays a rapid capacity loss with low capacity retention after repeated discharge and charge. The main reason also lies in the large Ge volume changes up to 300% during cycling, inducing the pulverization and exfoliation of the anode material from the current collector[48]. In order to solve this problem for the Ge anode, many strategies have been designed and reported, mainly involving reducing the particle size[49, 50], forming porous structures[51, 52] amorphization of the active materials[53, 54], and forming composites of Ge particles with conductive support materials[55, 56].

Currently, various composites containing germanates have been synthesized and used as anode material to mitigate the Ge volume changes in the charge and discharge processes[57-60]. The metal oxides formed in situ after the initial discharge could act as an elastic buffer to restrain the volume changes. Furthermore, because the metals in the compounds are normally abundant elements on earth, such as Fe, Cu, Ca, Zn, etc., employing the germanate anode could apparently lower the cost of using Ge-containing materials. In addition, such a matrix material could further alleviate the volume changes and the particle agglomeration that afflict the active material during cycling, and thus, anode integrity could be well maintained, which is favourable for improving the electrochemical performance of the anode material.

2.1.6.3 Metal Oxides

Metal oxides as anode materials have attracted extensive attention since Poizot's work[61] concerning the high capacity and reversibility of nanosized metal oxides was published. It was reported that there are three groups of metal oxides that can be classified based on the reaction mechanisms during cycling[62]: (1) the Li alloy reaction; (2) the insertion/extraction reaction; and (3) the conversion reaction. Specifically, SnO_2 and TiO_2 are the representative metal oxides in groups (1) and (2), respectively, and group (3) contains a wide range of metal oxides, including Co_3O_4, Fe_2O_3, NiO, etc. In contrast to the metal oxides in groups (1) and (2), the reaction mechanisms of metal oxides in group (3) include the reversible formation and decomposition of Li_2O, accompanying the reduction and oxidation of the metal particles, respectively. As Li_2O involved as an intermediate, metal oxides in group (3) could experience more completely reversible electrochemical reactions in the discharge and charge processes. By preparing metal oxides with different morphology or with carbon coating, their electrochemical performance could be significantly improved, with specific capacities from 500-1100 mAh g^{-1}[63], which are much higher than that of graphite anode, making them promising candidates as anode for LIBs.

2.1.6.4 Metal Sulphides

Metal sulphides were first considered as insertion cathode materials in primary Li batteries[64], and then some of them were used as cathode materials for LIBs[65]. Currently, many metal sulphides, such as MnS and MoS_2, were investigated as anode materials, and they are reported to react by a conversion mechanism to form Li_2S and metal

nanoparticles in the discharge process, which is similar to the mechanisms in primary Li-sulphur batteries[66-68]. Although they could deliver high capacities, the formation of soluble polysulfide intermediates after several cycles leads to severe capacity fading. Therefore, more efforts need to be directed towards improving their electrochemical performance before they can be considered as candidate materials for commercial anode.

2.1.7 Electrolyte

In LIBs, the electrolyte plays the important role of ensuring effective Li ion transport between the electrodes. The electrochemical stability of the electrolyte is closely associated with kinetic rather than thermodynamic factors during cycling. Typically, electrolytes can be classified into several categories, such as organic liquid electrolyte, inorganic liquid electrolyte, ionic liquid electrolyte, organic solid electrolyte, and inorganic solid electrolyte[14]. Among them, typical electrolytes and their key factors can be found in Table 2.1.

Organic liquid electrolytes have been widely investigated in recent years, in which $LiFP_6$ serves as the Li salt and carbonates, such as ethylene carbonate/diethyl carbonate (EC/DEC) and EC/dimethyl carbonate (DMC), as solvents. This electrolyte system is suitable for the LIB industry and typical electrode material testing in the laboratory. In order to achieve superior electrochemical performance, however, the combination of the solvents, Li salts, and additives should be intensively studied. Generally, the following requirements should be considered for an ideal electrolyte in a given system[69]:

(1) Non-flammable and environmentally friendly;

(2) Electronically insulating;

(3) Low cost;

(4) Wide discharge and charge stability window;

(5) High ionic conductivity (σ) (> 10^{-4} S cm^{-1}) and low electronic conductivity (< 10^{-10} S cm^{-1});

(6) Transference number $\sigma_{Li+}/\sigma_{total} \approx 1$ (where σ_{total} includes the conductivities of other ions in the electrolyte and σ_{Li+}).

Table 2.1 Typical electrolytes and their key factors for LIBs[14].

Electrolytes	Classical electrolytes	Ionic conductivity (10^{-3} s cm^{-1}, 25 °C)	Electrochemical Windows vs. Li^+/Li		Remark
			Reduction	Oxidation	
Liquid organic	1M $LiPF_6$ in EC : DEC (1:1)	7	1.3	4.5	Flammable
	1M $LiPF_6$ in EC:DMC (1:1)	10	1.3	> 5.0	
Liquid ionic	1M LiTFSI in EMI-TFSI	2.0	1.0	5.3	Non-flammable
	1M $LiBF_4$ in EMI-BF_4	8.0	0.9	5.3	
Polymer	LiTFSI-(PEO/MEEGE)	0.1	< 0.0	4.7	Flammable
	$LiClO_4$-PEO_8 + 10 wt. % TiO_2	0.02	< 0.0	5.0	
Inorganic solid	$Li_{4-x}Ge_{1-x}P_xS4$ (x = 0.75)	70	< 0.0	> 5.0	Non-flammable
	0.05 Li4SiO_4 + 0.57Li_2S + 0.38 SiS_2		< 0.0	> 8.0	
Inorganic liquid	$LiAlCl_4$ + SO_2	4.2	--	4.4	Non-flammable
Inorganic liquid + Polymer	0.04 $LiPF_6$ + 0.2 EC + 0.62 DMC + 0.14 PAN	3.0	--	4.4	Flammable
	$LiClO_4$ + EC + PC + PVdF		--	5.0	
Ionic liquid + Polymer	1M LiTFSI + P13TFSI + PVdF-HFP	0.18	< 0.0	5.8	Less Flammable
Ionic liquid + Polymer + Liquid organic	56 wt. % LiTFSI-Py24TFSI + 30 wt. % PVdF-HFP + 14 wt. % EC/PC	0.81	1.5	4.2	Less Flammable
Polymer +Inorganic solid	2 vol % $LiClO_4$-TEC-19 + 98 vol% 95 (0.6Li_2S + 0.4Li_2S) + 5Li4SiO_4	0.03	< 0.0	> 4.5	Non-flammable
Ionic liquid + Liquid organic		--	--	--	Non-flammable

2.2 Lithium-Oxygen Batteries

2.2.1 General Background

With the rapid development of our modern society, the global demand for energy has been rising continuously. It is proposed that basic energy needs will easily double within the next 15 years[70]. This will accelerate the exploitation and utilization of finite reserves, such as of oil, coal, and natural gas, and finally lead to their exhaustion. More seriously, heavy consumption of these fossil fuels poses a pollution problem and leads to the well-known greenhouse effect, which is affecting our living environment all the time. In response, clean energy from renewable sources including wind, wave, and solar power as alternative energy sources has been promoted for development [61]. These kinds of power sources, however, are variable and intermittent, depending on the weather conditions. Therefore, large-scale energy storage devices are required to offset this variability. More importantly, it is reported that petroleum, which powers our automobile and light truck applications, accounts for 34 % of the world's total primary energy sources[71]. In order to effectively utilize the renewable energy sources, hybrid electric vehicles (HEVs) and pure electric vehicles (EVs) have been developed and are attracting significantly more interest nowadays.

What kind of energy storage system could be used for powering the HEVs and EVs? Figure 2.6 exhibits the gravimetric energy densities of different types of rechargeable batteries[71] It is clear that Li-air batteries (Li-O_2 batteries) could offer extraordinarily improved energy storage capability, which is comparable to the practical capacity of

gasoline. Notably, it is still possible to greatly enhance the performance of Li-O_2 batteries, resulting in sufficient power storage for longer EV cruising distances per charge.

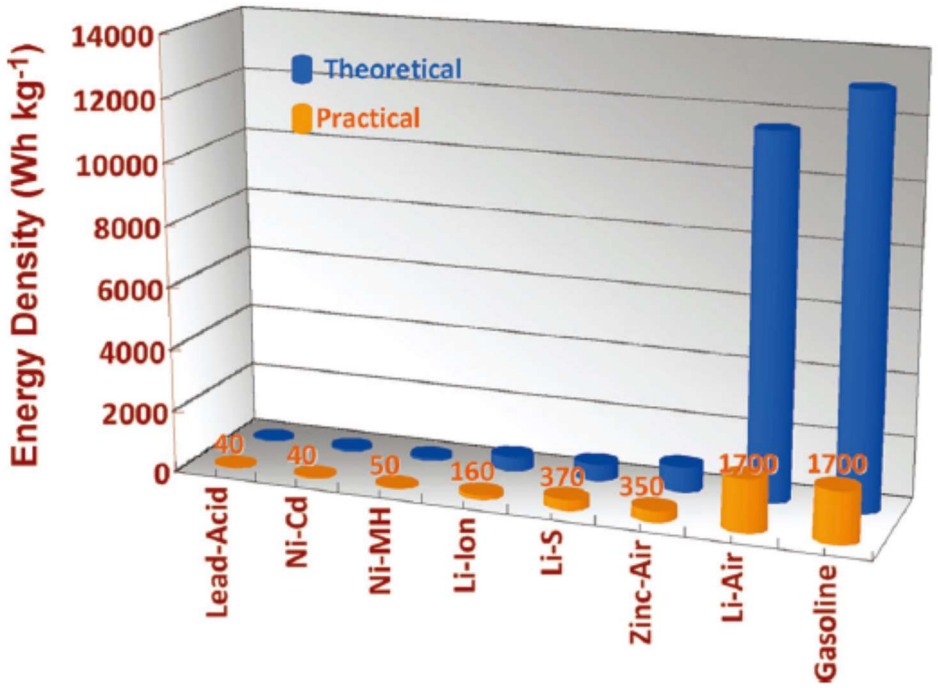

Figure 2.6 Gravimetric energy densities (Wh kg^{-1}) for various types of rechargeable batteries [71].

2.2.2 Brief History

Metal-O_2 batteries could generate electricity by redox reactions between the metal and the oxygen in air. They attracted much research interest a few decades ago, and the first review in 1979 by Blurton and Sammells provided detailed information on primary metal-O_2 batteries[72]. In fact, the authors paid more attention to Zn-O_2 batteries for their practical vehicle applications, instead of LOBs, at that time. Nevertheless, they found that a high theoretical gravimetric energy density of 11140 Wh kg^{-1} with 3V open-circuit

voltage could be reached for the LOBs, if the final discharge product is Li_2O. In 1996, Abraham and Jiang first reported a successful rechargeable LOB containing a Li metal anode, a carbon substrate cathode, and a gel polymer electrolyte[73]. Later, Read et al. probed the effects of ether-based electrolyte and air cathode formulation on the electrochemical performance of aprotic LOBs[74]. In 2006, Bruce et al. reported the reversibility of LOBs via Li_2O_2 as an intermediate, employing a liquid organic electrolyte and a MnO_2 cathode[75] Since then, LOBs have been brought back to the centre of attention and been considered as a technology to deal with the low-energy-density conundrum. During 2009-2010, IBM and several Department of Energy Laboratories established exploratory research programs on Li-air batteries, and the group members have grown exponentially to its present state of hundreds of research participants.

2.2.3 General Principles

The LOB family is composed of four electrocatalytic systems involving non-aqueous, aqueous, all-solid-state, and hybrid systems[76, 77]. All these systems are open systems, in which oxygen from the air serves as the cathode active material, and Li metal is used as the anode material. Catalytic cathode materials are necessary to promote the oxygen reduction (ORR) and oxygen evolution reactions (OER) during the discharge and charge process. The reaction mechanisms of the aqueous and hybrid systems are similar, because the cathodes all use an aqueous electrolyte. It was reported that there are organic electrolyte-based counterpart problems in both cases, which are caused by the clogging of air cathodes and contamination of Li-metal from moisture[78, 79]. For the solid-state systems, the solid electrolytes utilized are found to be unstable[80], and their Li ion conductivity is insufficient[71]. Therefore, the main focus in my doctoral research has been

the non-aqueous LOB system, because it has been demonstrated to have the greatest potential to meet the EV demands and has dominated LOB research efforts in the past decade.

The non-aqueous LOBs have a simple structure similar to that of LIBs, except that the cathode is exposed to air or oxygen. Figure 2.7 displays the working principles of non-aqueous LOBs. Generally, the reactions in non-aqueous LOBs are mainly governed by the cathode materials. In the discharge process, O_2 is reduced by electrons and reacts with Li ions to form the product Li_2O_2 on the cathode material, and the Li_2O_2 decomposes in the charge process with the release of O_2 and Li ions.

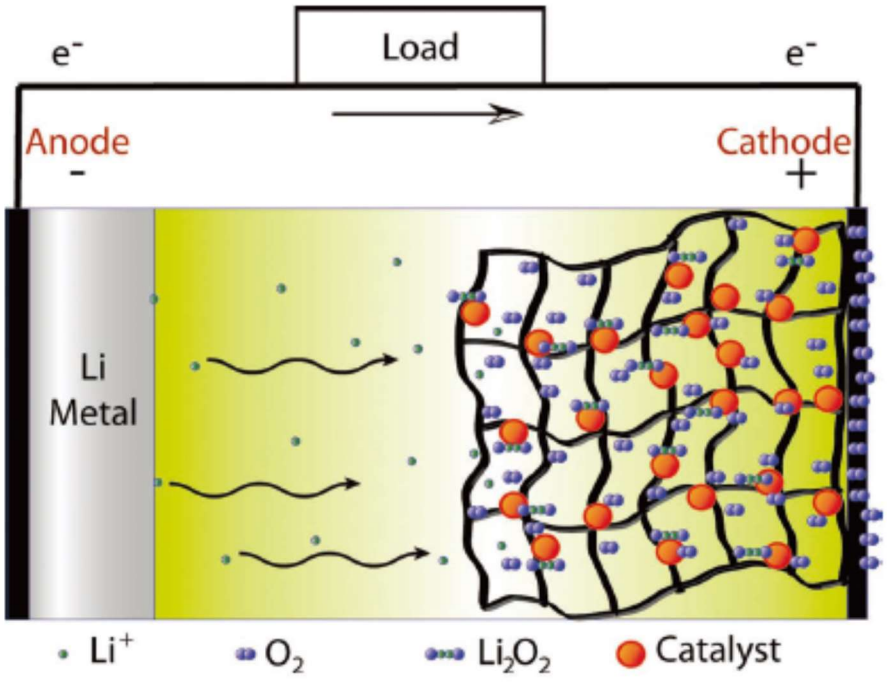

Figure 2.7 Schematic illustration of principles of a rechargeable Li-O_2 battery[70].

Theoretical potentials have been calculated for possible reactions in the following equations[70]:

$2Li + O_2 \rightarrow Li_2O_2$, ΔG^0= -571.0 kJ mol^{-1} (E^0 = 2.96 V) (2.8)

$4Li + O_2 \rightarrow 2Li_2O$, ΔG^0= -562.1 kJ mol^{-1} (E^0 = 2.91 V) (2.9)

Recent research data demonstrate that the half-life of O_2^- is also important for the reactions to form and decompose LiO_2 by a one-electron process. The detailed reactions involved are listed below[81]:

ORR in Cathode:

$O_2 + Li^+ + e^- \rightarrow LiO_2$ (2.10)

$2LiO_2 \rightarrow Li_2O_2 + O_2$ (2.11)

$LiO_2 + Li+ + e^- \rightarrow Li_2O_2$ (2.12)

$Li_2O_2 + 2Li^+ + 2e^- \rightarrow 2Li_2O$ (2.13)

OER in Cathode:

$LiO_2 \rightarrow O_2 + Li^+ + e^-$ (2.14)

$Li_2O_2 \rightarrow O_2 + 2Li^+ + 2e^-$ (2.15)

$Li_2O \rightarrow 0.5O_2 + 2Li^+ + 2e^-$ (2.16)

2.2.4 Basic Concepts

Based on those of the LIB system, some general concepts are supplemented to better understand the LOB system.

Potential is defined as is the electromotive force of a cell constructed from two electrodes. In fact, every electrochemical reaction is associated with a standard electrode potential (E^0), which can be calculated from the Gibbs free energy (ΔG^0) in the following equation:

$$\Delta G^0 = \Delta H^0 - T\Delta S^0 \quad (2.17)$$

where, ΔH^0, T, and ΔS^0 are the enthalpy, absolute temperature, and entropy, respectively. If all the released Gibbs free energy is assumed to be transformed to electrical work, electrode potential (E) could be calculated as follows:

$$E = -\frac{\Delta G}{nF} \quad (2.18)$$

where, n and F are the number of electrons involved in a stoichiometric reaction and the Faraday constant (96485 C mol^{-1}), respectively.

Overpotential can be calculated from the difference between the reduction potential thermodynamically governed by a half-reaction and the practical potential observed in a redox event. The overpotential is actually related to the high-activation barriers sometimes observed in the energy conversion processes, which need extra energy to overcome them. Catalyst materials are always employed in the electrode to lower the activation energy and thus decrease the overpotential of the electrochemical reaction.

Round-trip efficiency is the ratio between the value of the ORR plateau and the OER plateau in the discharge and charge process. It is dominated by the properties of the catalyst materials in the batteries.

2.2.5 Cathode Materials

It is well know that the electrocatalytic performance is strongly determined by the cathode catalyst material, which is undoubtedly regarded as the most important part of the LOBs. By using catalysts in the cathode which are beneficial for both of the ORR in discharge process and the OER in charge process, the round-trip efficiency, specific capacity, cycling stability, and rate capability can be significantly improved. In order to serve as an ideal cathode material for LOBs, the candidate catalyst should have the properties described below[82, 83]:

(1) High electrical conductivity;

(2) High specific surface area, offering high dispersion and utilization of nano-catalysts;

(3) High catalytic activity towards Li_2O_2 formation and decomposition;

(4) Chemically and electrochemically stable under the LOB operating conditions;

(5) Low reactivity with electrolytes in LOB systems.

Many efforts have been devoted to searching for suitable materials for LOBs according to these requirements, and it is concluded that promising cathode catalysts are mainly composed of carbonaceous materials, metals, metal oxides, and perovskites, which will be introduced in detail in the following sections.

2.2.5.1 Carbonaceous Materials

Currently, the applications of carbonaceous materials have been extended from LIBs and fuel cells to LOBs, with growing interest worldwide owing to their fascinating

characteristics. Typically, they can act as conductive additive for the cathodes in non-aqueous LOBs. Some of them, such as GNS and carbon nanotubes/nanofibers, show relatively high catalytic activity and could be used as catalyst materials in the cathode.

GNS have be considered as one of the most promising cathode catalysts due to its high theoretical surface area (2630 m^2 g^{-1}), excellent electrical conductivity (103 to 104 S m^{-1}), high electron transfer rate, and unique three-dimensional (3D) structure[84, 85]. It could provide potentially copious active sites for forming and decomposing Li_2O_2. Moreover, edge sites and defect sites on the GNS surface could also act as sites for the electrocatalytic reactions. Therefore, superior electrocatalytic performance can be achieved using GNS in the cathode for LOBs.

GNS-containing cathode was used by Li et al.[86] in non-aqueous LOBs, displaying a discharge capacity of 8705.9 mAh g_{carbon}^{-1} at a current density of 75 mA g_{carbon}^{-1}, which is much higher than those of the electrodes containing commercial carbon materials (BP-2000 and Vulcan XC-72). It was claimed that the discharge products were deposited on both sides and at the edges of the GNS, which extraordinarily improved the discharge capacity. Xiao et al.[87] prepared a novel hierarchical arrangement of structural and functionalized GNS, and the cathode containing this GNS delivered a discharge capacity of 15000 mA h g^{-1} at a current density of 0.1 mA cm^{-2}, which is the highest value among the reported GNS-based cathodes. This is attributed to the fact that a high density of reactive sites from the defects and functional groups on the GNS surfaces could facilitate the formation of nanosized Li_2O_2 particles to prevent air blocking in the cathode. Furthermore, O_2 could spread rapidly in the microporous channels of the hierarchically porous GNS, ensuring efficient electrocatalytic reactions. Sun et al.[88] utilized S-doped

GNS as cathode material for LOBs, and the results showed that the morphology of its discharge product (nanorods) was obviously different from that of the undoped GNS cathode (particles), leading to an improved charging performance. GNS has also been widely employed as a matrix to support highly catalytic nanoparticles to obtain enhanced battery performance[89-91]. This is because highly conductive GNS could speed up electron transfer in the cathode, increasing the electrochemical kinetics in LOBs. Moreover, high surface area GNS with a 3D framework is an excellent support for sufficient O_2 and electrolyte transport throughout the whole cathode, providing enough sites for the catalytic reactions and adequate space for the discharge products.

Carbon nanotubes (CNTs) and carbon nanofibers (CNFs) have also been applied to form porous gas diffusion cathode materials for non-aqueous LOBs. It was reported that a bare CNT cathode delivered a discharge capacity of about 800 mAh g^{-1} at a current density of 0.4 mA cm^{-2}[92]. Shen et al.[93] fabricated a sponge cathode from pure CNTs, and the results showed that its discharge voltage and specific capacity were 2.45 V and 6424 mAh g^{-1}, respectively, at a current density of 0.05 mA cm^{-2}. Hierarchical CNT fibrils were prepared by Lim et al.[94] and employed as cathode catalyst for LOBs. Owing to the tuned porosity in their woven structure, the CNT fibril cathode could effectively promote the reversible uniform formation and decomposition of Li_2O_2 that occurs among the fibrils. In addition, this structure could make O_2 easily accessible and prevent the pores from clogging, even after 100 cycles. CNTs and nitrogen-doped carbon nanotubes (N-CNTs) as cathode materials were compared in the LOBs, and the data showed that the N-CNT cathode displayed greatly improved discharge capacity and overpotential than those of the CNT cathode, implying that nitrogen-doping is an effective method to enhance the electrocatalytic performance of the carbon material. The all-carbon-fibre cathode was

synthesized by a chemical vapour deposition method using anodized aluminium oxide template[95]. It was claimed to have a gravimetric energy density of about 2500 Wh kg^{-1}. Shui et al. [96] have developed a highly efficient cathode by using vertically aligned nitrogen-doped coral-like carbon fibre arrays on a stainless steel current collector. This cathode showed a low overpotential of 0.3 V between the charge/discharge plateaus, and a high energy efficiency of 90% in a full discharge/charge cycle. With a capacity cut-off of 1000 mAh g^{-1}, it could also show an excellent cycling stability of more than 150 cycles. In fact, (N-)CNTs and (N-)CNFs could also be used as support materials for nanoparticles with high catalytic properties[97-100]. With high surface area, they could offer electrocatalytic sites for the formation and decomposition of the discharge products. Moreover, they are in the form of conductive webs, promoting efficient electron transfer and catalytic reactions throughout the whole cathode. Additionally, the nitrogen doping not only increases the electrical conductivity and catalytic activity of the cathode, but also has benefits for the distribution of catalyst nanoparticles, leading to improved electrocatalytic performance.

2.2.5.2 Metals

Non-precious metals as cathode catalyst materials were studied in the early stages of the LOB development, and the results showed limited electrocatalytic performance[101, 102]. Currently, a great deal of effort has been devoted to the research on precious metals as cathode catalyst materials, owing to the fact that they could significantly lower the ORR/OER overpotentials and increase the specific capacity. Although they are expensive, a small addition of them in the cathode could play an important role in enhancing the battery performances. According to the *d*-band model and the Sabatier principle, the

metals of the Pt family have been regarded as promising cathode catalysts, because of their intrinsic half-filled antibonding states, providing proper adsorption strength between the catalyst and target chemical specie. A free-standing cathode were prepared by Xu et al. by depositing honeycomb-like palladium-modified hollow spherical carbon onto carbon paper[103]. It displayed a discharge capacity of 5900 mAh g^{-1} at a high current density of 1500 mA g^{-1}, and could be discharged and charged for 100 cycles at a current density of 300 mA g^{-1} with a capacity limit of 1000 mAh g^{-1}. Jeong et al.[104] presented a systematic evaluation of Pt, Pd, and Ru nanoparticles supported on GNS as OER electrocatalysts in LOBs. The results demonstrated that all of them could decrease the charge overpotentials, and Ru-GNS hybrids showed the most stable cycling performance and the lowest charge overpotentials. This is mainly because Ru nanoparticles could promote thin-film-like or nanoparticulate Li_2O_2 formation.

Lu et al.[105] investigated the activities of typical metals in the Pt family, and the results are summarized in Figure 2.8, compared with those obtained with Au and glassy carbon (GC). As can be observed in the figure, the ORR activities were found to drop in the order: Pd > Pt > Ru ≈ Au > glassy carbon, which is closely related to the oxygen adsorption energy on their surfaces. This trend is strongly consistent with the results for high-surface-area thin-film catalysts supported on GC electrodes and early discharge voltages of LOBs.

It is reported that some alloy cathodes exhibit superior electrocatalytic performance compared to those of the single metal cathodes. Yin et al.[106] compared the battery performance of a PtAu/C cathode with Au/C and Pt/C cathodes, and the data demonstrated that the fully and partially alloyed PtAu/C catalysts showed higher discharge capacity and limited overpotentials, leading to an improved round-trip

efficiency. Similar results could also be found in the work on $PtCo_3$[107], AuPt[108], Pd_3Fe[109], and PdCu[110] cathodes.

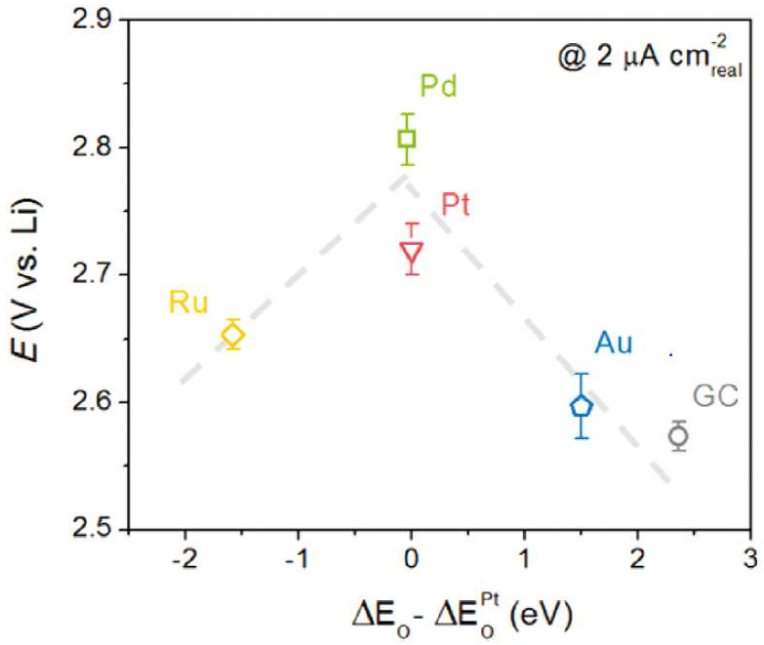

Figure 2.8 Non-aqueous Li-ORR potential at 2 μA cm^{-2} as a function of the calculated oxygen adsorption energy, ΔE^0 (per oxygen atom relative to an atom in the gas phase), relative to that of Pt[105].

2.2.5.3 Metal Oxides

Transition metal oxides as cathode catalyst materials have aroused much more attention since the related work was published in 2008 [111]. In Figure 2.9, various types of manganese oxides as cathode catalysts were investigated to compare their battery performance, and the results showed that α-MnO_2 has the largest capacity and best capacity retention among the manganese oxides involving other MnO_2 polymorphs, Mn_2O_3 and Mn_3O_4. This finding demonstrates that the crystal structure is one of the most

important factors that influence the electrocatalytic performance. Moreover, the cathode containing α-MnO_2 nanowire was proved to outperform its counterpart containing α-MnO_2 bulk, because the nanowires promoted the formation and decomposition of Li_2O_2.

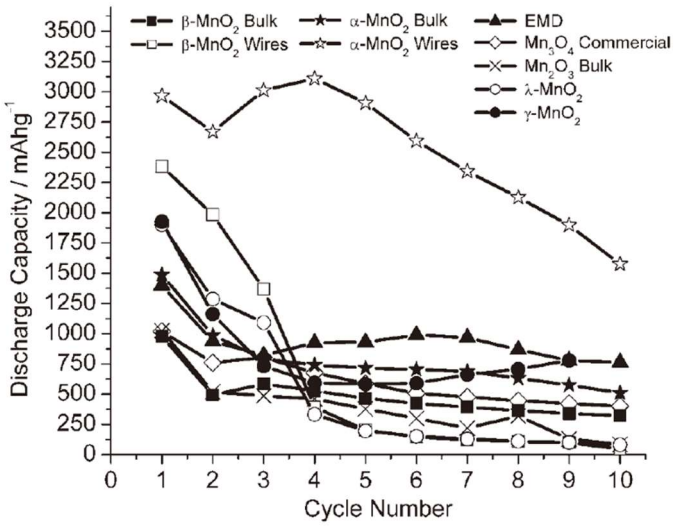

Figure 2.9 Comparison of discharge capacity with cycle number for several cathodes containing manganese oxides[111].

Debart et al.[112] also found that other transition metal oxides such as Fe_3O_4 and Co_3O_4 could offer favourable performance as cathode catalysts. It should be noted that Co_3O_4 exhibited the best performance through a combination of high initial discharge capacity and capacity retention during cycling, as well as having the lowest charging voltage at 4 V. Therefore, Co_3O_4 containing cathode has attracted tremendous interest and has been intensively studied in recent years. Wu et al.[113] prepared a free-standing cathode containing hierarchical Co_3O_4 ultrathin nanosheets on Ni foam. It showed a capacity of 11882 mA h g^{-1} at 100 mA g^{-1} and good cycling stability (at least 80 cycles at 200 mA g^{-1} with fixed capacity of 500 mA h g^{-1}), with a greatly decreased charge voltage of 3.7 V. It was reported that a GNS-Co_3O_4 composite cathode could deliver a specific capacity of

2453 mAh g^{-1} at 0.1 mA cm^{-2} and showed 62 stable cycles with a fixed capacity of 1000 mAh g_{carbon}^{-1}[114]. It was demonstrated that the improved battery performance is related to the unique 3D structure and superior catalytic activity of the cathode. In addition to these transition metal oxides, ruthenium oxide[115, 116] and iridium oxide[117, 118] have also received much attention due to their excellent ability to facilitate the OER in the form of composites with carbon or other conductive substrate materials.

Perovskite oxides are normally present with the archetypal formula of ABO_3 or $AAB'B'O_3$. They have been regarded as a promising candidates as cathode catalysts for LOBs, due to their high electronic/ionic conductivity and high catalytic activity. Typical perovskite oxides, such as $La_{0.75}Sr_{0.25}MnO_3$[119], $LaNiO_3$[120], and $LaNi_{1-x}Fe_xO_3$[121], have been reported to act as bifunctional catalysts to promote both the ORR and OER, offering favorable electrocatalytic performance. The effects of partial substitution in both cation sublattices, however, have not been intensively researched, and the mechanisms are still not clear. Therefore, much more systematic work on perovskite oxide catalysts for LOBs should be conducted in the future.

2.2.6 Anode Materials

Li metal is theoretically regarded as the most promising anode candidate for LOBs because it has the lowest negative potential (-3.04 V vs. SHE) and extremely high specific energy (3860 mAh g^{-1}). Nevertheless, its highly reactive nature could be a severe problem affecting the development of the LOBs. There are two major negative issues associated with using Li metal anode. One is the formation of dendrites, which can cause short-circuits and results in a serious safety issue. The other one is the continuous growth of a

solid electrolyte interphase (SEI) layer, leading to a low coulombic efficiency and limited cycle life[71]. Therefore, unless properly protected or replaced by another ideal anode, Li metal could not be proposed as an anode for commercial battery fabrication.

To deal with this problem, a lithiated Si-C composite was prepared by Hassoun et al.[122] and used as an alternative anode material. The results showed that this anode could be discharged and charged at a capacity of 1000 mA h g^{-1} for at least 15 cycles with low overpotentials. Moreover, Li_xAl/C composite with a uniform SEI film was investigated to serve as an anode material for LOBs[123]. This battery displays a lower voltage gap between charge and discharge compared with that of a battery with a Li metal anode. When ambient air with limited humidity was used as the active material, the Li_xAl/C anode displayed better cycling performance. Furthermore, Liu, et al.[124] fabricated a Li metal anode with a LiF-containing protective film by the fluoroethylene-carbonate treatment method. Significantly improved cycling stability (up to 106 cycles) was obtained, which was more than three times that of a LOB with pristine Li metal as an anode (31 cycles). In addition, a Li-Al-Ge-P glass-ceramics layer[125] and polyvinylidene fluoride-hexafluoro propylene with an Al_2O_3 layer[126] were reported to provide effective protection to the Li metal anode, respectively, and both of them led to greatly improved cycling behaviour.

2.2.7 Non-aqueous Electrolyte

The choice of electrolyte is one of the most important factors in the performance and development of non-aqueous LOBs. Apart from the typical requirements for electrolytes employed in Li-ion batteries (such as high ionic and low electronic conductivity, wide

electrochemical window, and being electronically insulating), electrolytes employed in LOBs should possess the following characteristics[127]:

(1) Stable under oxygen-rich electrochemical conditions;

(2) High boiling point/low vapour pressure;

(3) High oxygen solubility and diffusivity;

(4) Stable towards metallic Li.

Electrolytes for non-aqueous LOBs mainly include carbonate-, ether-, sulfone-, amide-, and ionic liquid based electrolytes, and the main properties of the solvents can be found in Table 2.2[128]. Carbonate-based electrolyte was used in the early stages of LOB development. It was reported that the discharge products are composed of a series of carbonate species with little Li_2O_2, resulting from the electrolyte decomposition[129, 130]. Recently, ether-based electrolytes have been intensively investigated and are widely used in non-aqueous LOBs, because they were proved to have long-term chemical stability towards the intermediate O_2^-[131, 132]. With ether-based electrolytes, Li_2O_2 has been found to be the dominant discharge product in the catalyst cathode during cycling, owing to the fact that these electrolytes with low donor number could facilitate the conversion from O_2^- to O_2^{2-} and O^{2-}[81]. The intermediates and products could also be stabilized in sulfone-based electrolytes, leading to superior electrocatalytic performance as well[133, 134]. Other non-aqueous electrolytes including amides[135, 136] and ionic liquids[137, 138] were also studied, and the obtained data provide a profound understanding of the operation of LOBs, which is beneficial for accelerating the attainment of the intriguing promise offered by LOBs.

Table 2.2 Main properties of solvents mostly used in electrolyte for nonaqueous Li-O_2 batteries[128].

Solvent		Molecular weight	Structure	Dielectric Constant ε (25°C)	Dipole moment (μ)	Donor number (kcal mol^{-1})	Viscosity η (cP) (25 °C)	Oxygen solubility (mM cm^{-3})	Boiling/melting point (°C)	Vapor pressure (kPa, 25°C)	Density (g cm^{-3}, 25°C)
Carbonate	PC	102		64.92	4.94 (18°C)	15.1	2.53	3.2	241.7/-48.8	0.160 (55°C)	1.1951
	EC	88		89.78 (40°C)	4.87 (25°C)	16.4	1.930 (40°C)	1.71	248.2/36.4	3.371 (95.21°C)	1.3383
	DMC	90	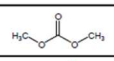	3.107		17.2	0.59 (20°C)	7.29	91/4.6	2160	1.063
	EMC	104	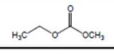	2.958			0.65	7.95	110/-53	0.89	1.006
	DEC	118	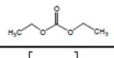	2.820 (20°C)	0.90 (25°C)	16	0.748	7.92	126.8/-74.3	1.3 (23.8°C)	0.96926
Ether	TEGDME	222	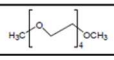	7.79		16.6	4.05	4.43	275/-30	<1.33	1.009
	DME	90	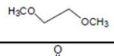	7.2	1.71 (25°C)	20	0.455	9.57	84.5/-58	6.4 (20°C)	0.86370
Sulfone	DMSO	78	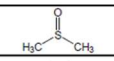	46.45	4.06 (25°C)	29.8	1.991	2.1	189/18	56	1.1
	TMS	120						1.59	285/28	1.33	1.261
Amide	DMF	73		36.71	3.24 (25°C)	26.6	0.802		153/-61	0.49	0.94387
	DMA	87		37.78	3.71 (30°C)	27.8	0.927		166.1/-20	0.17	0.936337
Ionic liquid	[C4mim][Ntf2]	419.36	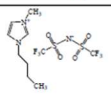				44		/-1		1.429
	[C4mim][BF4]	226.02	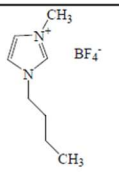				92		/-71		1.26

CHAPTER 3 EXPERIMENTAL

3.1 List of Materials

The list of materials and chemicals used during my study for the synthesis and characterization of materials is summarized in Table 3.1.

Table 3.1 Description of chemicals and materials used in this study.

Materials/Chemicals	Formula	Purity	Supplier
Ammonium peroxydisulfate	$(NH_4)_2S_2O_8$	98%+	Sigma-Aldrich
Carbon black	C	Super P	Timcal Belgium
Cetyltrimethylammonium bromide	$C_{19}H_{42}BrN$	99%+	Sigma-Aldrich
Electrolyte	$LiPF_6$-EC/DEC	BG	Guotai-Huarong
Ethanol	C_2H_5OH	Reagent	Q-Store Australia
Germanium(IV) oxide	GeO_2	99.99%+	Aldrich
Graphite	C	n/a	Fluka
Hydrochloric acid	HCl	37%	Sigma-Aldrich
Hydrogen peroxide	H_2O_2	30%	Sigma-Aldrich
Isopropanol	$(CH_3)_2CHOH$	99.7%+	Sigma-Aldrich
Lead(II) acetate trihydrate	$Pb(CH_3COO)_2 \cdot 3H_2O$	99.99%+	Sigma-Aldrich
Lithium foil	Li	BG	Ganfeng
Lithium hexafluorophosphate	$LiPF_6$	99.99%	Sigma-Aldrich
Lithium trifluoromethanesulfonate	$LiCF_3SO_3$	99.995%	Sigma-Aldrich

Nafion	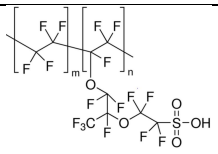	5% in water and isopropanol	Sigma-Aldrich
Palladium chloride	$PdCl_2$	99%	Sigma-Aldrich
poly(tetrafluoroethylene)	$(C_2F_4)_n$	n/a	Sigma-Aldrich
Poly(vinylidene) fluoride	$(CH_2CF_2)_n$	n/a	Sigma-Aldrich
Polypropylene	$(C_3H_6)_n$	Celgard 2500	Hoechst Celanese
Potassium permanganate	$KMnO_4$	99%+	Sigma-Aldrich
Pt on Vulcan XC-72	Pt/C	20 wt.%	E-Tek
Pyrrole	C_4H_5N	98	Sigma-Aldrich
Single-walled carbon nanotube	C	85%+	Unidym
Sodium borohydride	$NaBH_4$	99%+	Fluka
Carboxymethyl cellulose (MW=90000)	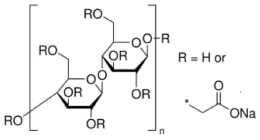	n/a	Sigma-Aldrich
Sodium hydroxide	NaOH	98%+	Sigma-Aldrich
Potassium hydroxide	KOH	90%+	Sigma-Aldrich
Sodium nitrate	$NaNO_3$	99%	Sigma-Aldrich
Sulphuric acid	H_2SO_4	95-98%	Sigma-Aldrich
Tetraethylene glycol dimethyl ether	$CH_3O(CH_2CH_2O)_4$	99%+	Sigma-Aldrich
Triton X-100	$(C_2H_4O)_n{\cdot}C_{14}H_{22}O$	n/a	Sigma-Aldrich

3.2 Experimental Procedures

The logical framework of the experimental procedures in this thesis is summarized in Figure 3.1. Materials were synthesized via different kinds of preparation methods and identified through various physical techniques. Electrochemical properties were

characterized, including the application of the electrode materials, in linear sweep voltammetry (LSV) measurements, LIBs, and LOBs. Ex-situ characterizations were conducted to investigate the structural and morphology changes after electrochemical cycling.

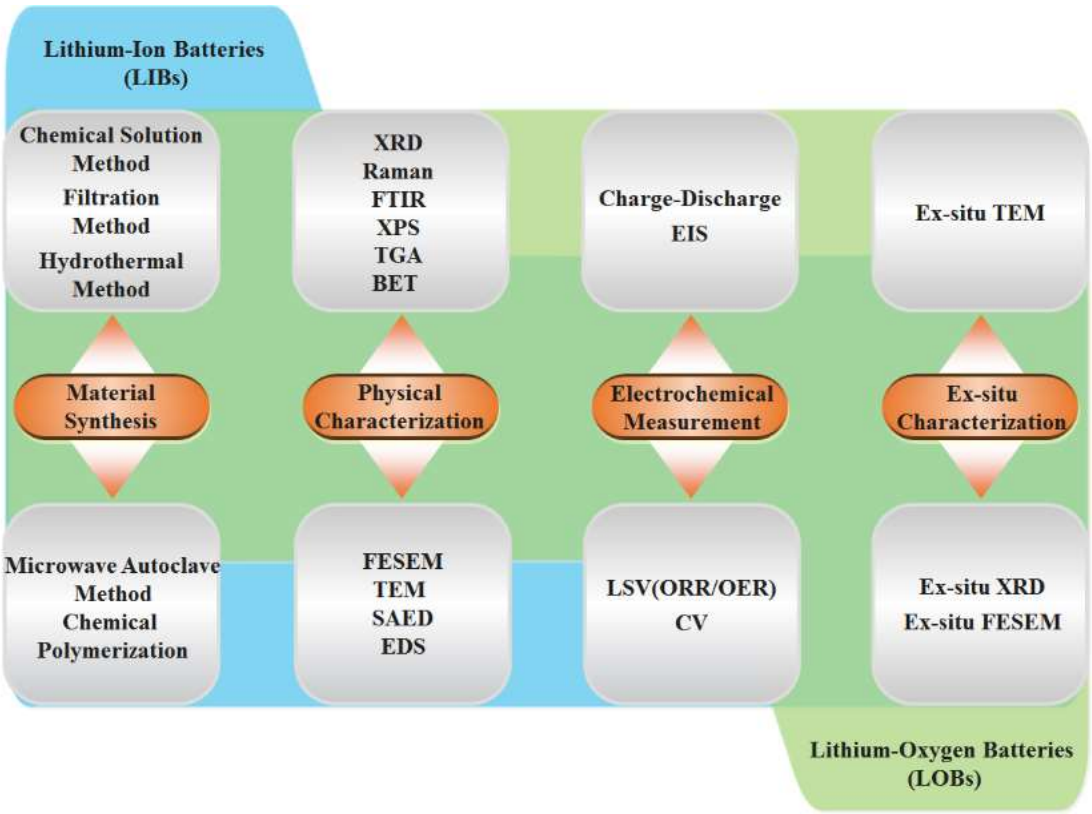

Figure 3.1 Outline of the experimental procedures.

3.3 Materials Preparation

3.3.1 Chemical Solution Method

Solution phase is an important medium for chemical reactions, and the solution is a homogeneous mixture including two or more substances. The substance in lesser amount

in the solution is called the solvent, whereas the substance in the minor proportion is called the solute. The solute is dispersed homogeneously throughout the solvent, and it is also possible that the solution contains several solutes. Typically, the solution has an even composition and properties, because it is an intimate and random homogeneous mixture of atomic-size chemical species, ions, or molecules. Therefore, the reactants in the solution could make full contact with each other, which is helpful for uniform and stable chemical reactions with rapid reaction rates. Based on these considerations, the chemical solution method is believed to be very suitable for acquiring the control over the particle size, shape, and composition of the final products.

In Chapters 4 and 7, the chemical solution method was utilized to synthesize the Ge/SWCNT and the Pd/PNCNF composites. In an alkaline medium, the Ge and Pd precursors were reduced by $NaBH_4$ on the single walled carbon nanotube (SWCNT) and porous nitrogen doped carbon nanofiber (PNCNF) substrates in the preparation processes, forming the Ge/SWCNT and the Pd/PNCNF composites with unique three-dimensional (3D) structure, respectively.

3.3.2 Filtration Method

The filtration method is an effective way to prepare free-standing electrodes. High suction caused by the strength of the pump under a positive pressure of 400 kPa was applied to draw liquid through the filter paper, forming product films in the funnel. Because the products are nanosized materials, poly(vinylidene fluoride) (PVDF) membranes 47 mm in diameter with 0.22 μm pore size were employed. The vacuum filtration unit for preparing the free-standing electrodes can be seen in Figure 3.2.

Figure 3.2 Vacuum filtration unit for preparing the free-standing electrodes.

The thickness of the films is closely related to the amount of suspension passing through the filtration process. Surfactants, in some cases, are needed to stabilize the solution. To achieve uniform SWCNT-based suspensions, Triton-X 100 is widely used to enhance their dispersibility in aqueous solutions. Afterwards, the suspensions could be filtered to gain a consistent batch of free-standing films. The remaining surfactants were removed by repeated washing with distilled water and ethanol.

In Chapter 4, the vacuum filtration method is adopted to fabricate the free-standing Ge/SWCNT composite anodes. The as-prepared Ge/SWCNT composites were poured into the funnel and filtered by suction through porous membranes to form the composite

anodes. These anodes without current collector supports and binders in them could be directly used in LIBs.

3.3.3 Hydrothermal Method

The hydrothermal method is a widely used wet-chemical treatment to crystallize substances from high-temperature aqueous solutions at high vapour pressures. By utilizing this technique, extremely efficient crystal growth and nanomaterial synthesis can be realised. The advantages mainly include preparation of novel phases, stabilization of new complexes, and synthesis of various material morphologies for specific applications. There are many factors affecting the composition, morphology, and crystal structure of the final products, such as the solvent type, the amount and concentration of the precursor solution, the temperature, the pH value, and the use of surfactant.

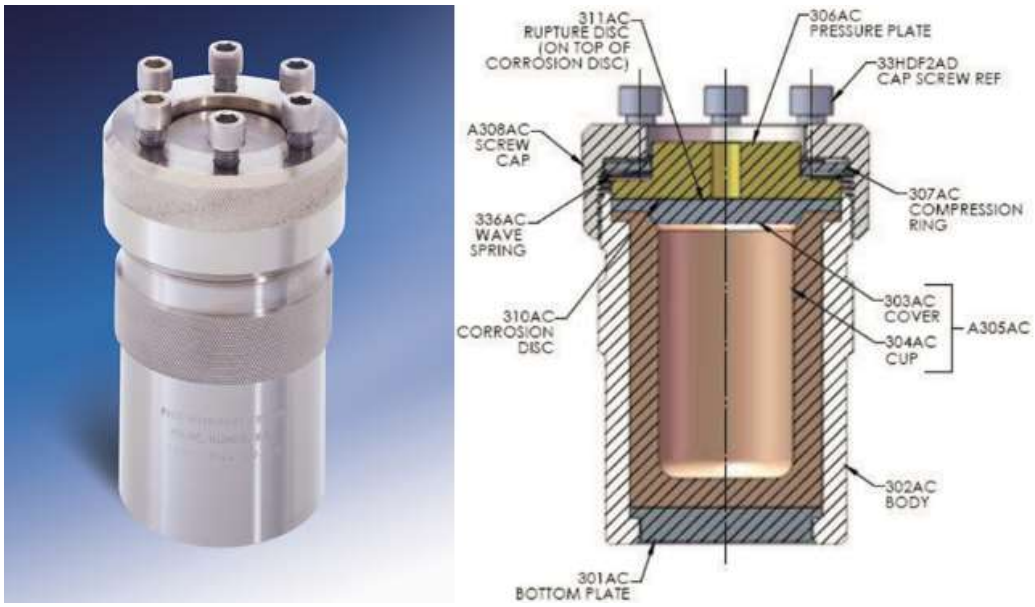

Figure 3.3 Hydrothermal autoclave (Acid Digestion Bombs 4748) from Parr Instruments (left) with a cross-sectional view (right).

The hydrothermal reaction vessels employed are autoclaves, and the autoclaves used in this PhD work were 4748 Acid Digestion Bombs with 125 ml capacity from the Parr Instrument Company (Figure 3.3). They are mainly composed of polytetrafluoroethylene (PTFE) vessels on the inside and stainless steel protectors on the outside. The autoclaves are normally kept in a conventional oven with a programmed temperature and duration of time. The precursor volume limit is 2/3 of the volume of the PTFE vessel in order to ensure safety. The maximum working temperature is 250 ^{o}C, and the pressure can reach up to 1900 psi.

In Chapter 5, the hydrothermal method was used to synthesize the $PbGeO_3$-GNS composites from the precursor solution containing $Pb(CH_3COO)_2 \cdot 3H_2O$, GeO_2, and GO. In the composites, $PbGeO_3$ nanowires with diameters in the range of 100-200 nm were formed in situ in the conductive and interconnected GNS networks.

3.3.4 Microwave Autoclave Method

The working principles of the microwave autoclave method are similar to those of the conventional hydrothermal method. The key difference is that the heat is provided internally by the microwave irradiation in the microwave autoclave method, instead of being generated from an external heating source as in the hydrothermal method. Moreover, the reactions in the hydrothermal method usually lasts from half a day to several days, and their electric power requirement is over a thousand watts. In contrast, equivalent conditions in the microwave autoclave method require several seconds to hours and hundreds of watts, respectively[139]. This mean that the microwave autoclave method is a

promising technique for the synthesis and processing of electrode materials because of its notably shorter reaction times and lower power consumption.

Figure 3.4 MicroSYNTH microwave system (Milestone) with a working frequency of 2.45 GHz controlled by a Labthermal 800 controller.

In this thesis, a MicroSYNTH microwave system (Milestone) controlled by a Labthermal 800 controller was used, as shown in Figure 3.4. Its frequency is 2.45 GHz and the maximum power is up to 500 W. It is equipped with a 45 mL quartz vessel where the reaction temperature and pressure must be less than 250 ^{o}C and 40 bar, respectively. The vessel is fixed in a safety shield that possesses built-in pressure control by a preloaded spring with a vent and resealing mechanism. The reaction conditions could be preset via a monitoring and software programming system.

In Chapter 6, the microwave autoclave method was applied to prepare MnO_2/GNS composites. The composites were effectively fabricated in a fast and energy saving way, and the MnO_2 nanoflakes were uniformly grown in situ on the surfaces of the 3D GNS skeleton.

3.3.5 Chemical Polymerization

Polymerization occurs by the combination of the starting monomer molecules in a chemical reaction to form polymer chains or three-dimensional networks[140]. The reaction mechanisms for the polymerization vary in complexity because of the functional groups present in reacting compounds and their inherent steric effects. In more straightforward polymerization, the relatively stable alkenes with σ bonding between carbon atoms form polymers by relatively simple radical reactions; in contrast, more complex reactions such as those that include substitution at the carbonyl group require more complex synthesis due to the way in which reacting molecules polymerize[141, 142].

The monomer molecules could be all alike, or they could represent two or more different compounds. In general, at least 100 monomer molecules must be reacted to form a polymer that can offer some distinct physical properties-such as high tensile strength, elasticity, or the ability to form fibers. There are a variety of polymerization route involving different reactions. Typically, polymers such as polyvinyl chloride are known as “homopolymers”, because they are composed of repeated long chains or structures of the same monomer unit (Equation 3.1), whereas polymers that consist of more than one molecule are referred to as copolymers (Equation 3.2)[143]:

Homopolymers: A + A + A⋯→ AAA⋯ (3.1)

Copolymers: A + B + A⋯→ ABA (3.2)

In Chapter 7, the polypyrrole (PPy) nanofibers were synthesized via the chemical polymerization route. Pyrrole (Py) monomer and the surfactant Cetyltrimethylammonium bromide (CTAB) were dispersed in a cool acid solution. Ammonium peroxydisulfate (APS) serving as the initiating agent was then added into the as-prepared solution to enable the polymerization reaction. The polymerization precursor solution is allowed to react for 24 h, and polypyrrole (PPy) nanofibers were obtained.

3.4 Electrode Preparation and Coin-Cell Assembly

3.4.1 Electrode for Lithium-Ion Cells

A mixture of 80 wt. % active materials, 10 wt. % conductive carbon (carbon black), and 10 wt. % binder [carboxymethyl cellulose (CMC)] with the solvent (distilled water) were added into a rotary mixer to make a homogenous slurry. The slurry was spread onto the current collector (copper foil) by a roller coating technique, and it was then dried in a vacuum oven for 12 h. After a rolling-press procedure, the disk electrodes (0.95 cm in diameter) were cut out by a precision punch. The free-standing electrodes were cut into a 1×1 cm^2 square size from the films prepared by the filtration method. Finally, the working electrodes were ready to be assembled into LIB coin cells in a glove box filled with argon gas.

The cells were assembled in an argon-filled glove box (Mbraun, Unilab, Germany) with O_2 and H_2O levels less than 1 ppm. CR2032 coin type cells were utilized in the battery

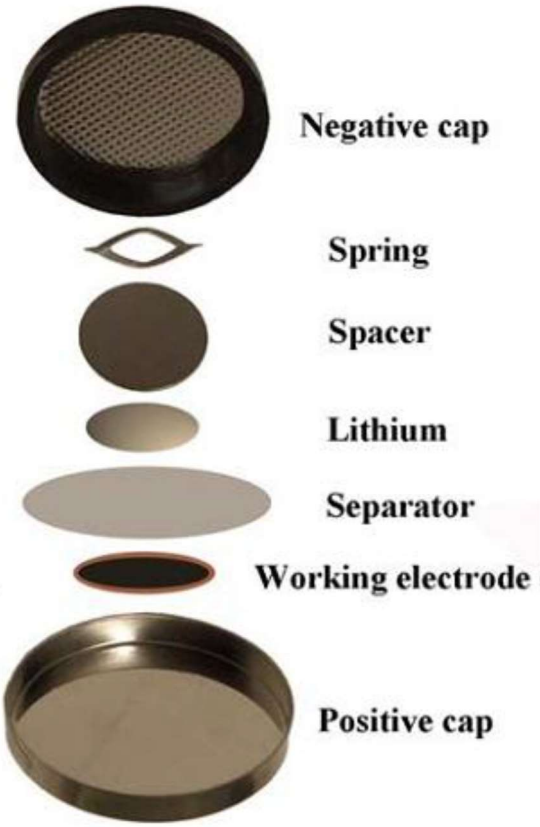

Figure 3.5 Stacking components of a CR2032 coin cell[144].

tests. Apart from the working electrode, these cells also contain a porous Celgard polypropylene membrane as separator, Li foil as counter electrode, and 1 M $LiPF_6$ in a 50 : 50 (v/v) mixture of ethylene carbonate (EC) and diethyl carbonate (DEC) as the electrolyte. The coin-cell components for LIBs are shown in Figure 3.5 in their stacking sequence.

3.4.2 Electrode for Lithium-Oxygen Cells

A homogenous slurry was prepared by mixing 90 wt. % catalyst materials and 10 wt. % binder (PTFE) with the solvent (isopropanol). It was pasted onto carbon paper and dried at 120 ºC in a vacuum oven for 12 h. The typical loading of the slurry for the punched disk electrode (0.95 cm in diameter) was about 1.0±0.1 mg cm^{-2}. The electrodes were then transferred into a glove box filled with argon gas for LOB coin cell assembly.

The cells were assembled in an argon-filled glove box (Mbraun, Unilab, Germany) with O_2 and H_2O levels less than 1 ppm. CR2032 coin type cells with holes in the cathode parts were used in the battery tests. A glassy fiber separator was applied to separate the cathode as the working electrode from the Li foil as the counter electrode. 1 M Li trifluoromethanesulfonate ($LiCF_3SO_3$) in tetraethylene glycol dimethyl ether (TEGDME) was utilized as the electrolyte. The coin-cell components for LOBs are shown in Figure 3.6 in their stacking sequence.

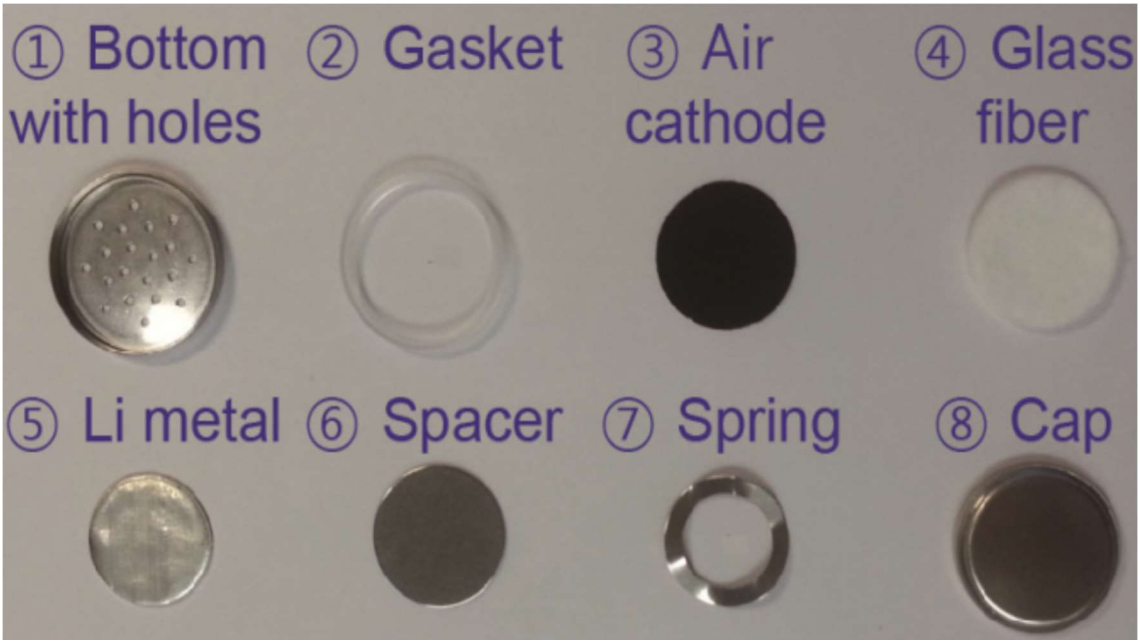

Figure 3.6 Stacking components of a CR2032 coin cell[107].

3.5 Physical and Structural Characterization

3.5.1 X-Ray Diffraction

XRD is a basic tool to study the crystallographic structure, crystallite size (grain size), and preferred orientation in polycrystalline or powdered solid samples. X-ray radiation is a kind of electromagnetic wave with a wavelength in the range of 0.01 to 10 nm, on the same order as the atomic plane *d*-spacing in crystals, which are regular arrays of atoms. Therefore, the X rays can be scattered by each set of lattice planes of the crystals at a characteristic angle, and the scattering patterns are collected and analysed. The patterns are associated with the crystal structure, because every crystal features a set of unique *d*-spacings. Bragg's law (Eq. 3.1) describes the diffraction condition from planes with spacing *d*:

$$n\lambda = 2d\sin\theta \tag{3.1}$$

Where n is an integer, λ is the wavelength of the incident X-ray beam, d is the lattice spacing of the crystal, and θ is the angle of the incidence.

In this thesis, all the XRD measurements were conducted using a GBC MMA X-ray generator and diffractometer with Cu Kα radiation (λ = 1.5406 Å). The powdered material is coated on a disk holder with a flattened surface. The holder is placed on the axis of the diffractometer at an angle θ. The detector rotates around the diffractometer on an arm at the corresponding angle 2θ. The working voltage and current were programmed at 40 kV and 25 mA, respectively.

3.5.2 Raman Spectroscopy

Raman spectroscopy is an important characterization technique to investigate the vibrational, rotational, and other low frequency modes in a structure. Laser light from the monochromatic light source in the Raman tests is employed to irradiate the material, leading to both elastic scattering (Rayleigh scattering) and inelastic scattering (Stokes and anti-Stokes Raman scattering). In contrast to Rayleigh scattering, both the Stokes and anti-Stokes Raman scattering display energy shifts from the incident radiation, which is called the Raman effects. These energy shifts are detected and collected in the form of frequency or wavelength, and the corresponding spectra can provide the information on the chemical composition and structure of the sample materials.

Generally, a Raman system contains the excitation source (laser), the illumination system and light collection optics, the wavelength selector filter (filter or spectrophotometer), and the detector, which includes a photodiode array and charge-coupled device (CCD), or a photomultiplier tube. The material is illuminated with a laser beam in the ultraviolet, visible, or near infrared range. A lens is used to collect the scattered light, which is then delivered through an interference filter to yield the Raman spectrum.

The Raman spectroscopy was performed using a JOBIN YVON HR 800 Horiba Raman spectrometer with a laser at 632.8 nm excitation on a 300 lines/mm grating and a charge-coupled detector CCD. A neutral density filter is applied to adjust the laser intensity in the measurement.

3.5.3 Fourier Transform Infrared Spectroscopy

Fourier transform infrared spectroscopy (FTIR) is a commonly used method to determine the absorption, emission, photoconductivity or Raman scattering in the infrared spectrum of a material. In the testing process, IR radiation interacts with the material, through which the infrared radiation is transmitted or absorbed. The spectral pattern of molecular absorption and transmission can give information on the chemical bonds in the molecules of the sample material.

FTIR spectra were collected on a Shimadzu IRPresting-21 model Fourier transform infrared spectrometer. Before the measurement, the sample materials were mixed with potassium bromide (KBr) powder and pressed in a die with a barrel. KBr acts as the background file.

3.5.4 X-Ray Photoelectron Spectroscopy

X-ray photoelectron spectroscopy (XPS) is a surface-sensitive quantitative spectroscopic method to study the elemental composition, empirical formula, chemical state, and electronic state of the elements within a material. In the measurement, a beam of X-rays is employed to interact with the sample material, while the kinetic energy and number of electrons that escape from the top surface of the material (0-10 nm) are simultaneously monitored, from which the XPS spectra are obtained. Based on the characteristic binding energies associated with electrons in their orbitals, the valence states of elements can be determined, and the ratios of the valence states could be also gained from the spectra. In

this thesis, XPS analysis was conducted on a VG Scientific ESCALAB 2201XL system using Al Kα X-ray radiation and fixed analyzer transmission mode.

3.5.5 Thermogravimetric Analysis

Thermogravimetric analysis (TGA) is a type of analysis for detecting changes in weight in relation to changes in temperature. This technique is widely utilized to study some of the material characteristics reflected by the precise weight changes caused by decomposition, oxidation, or loss of volatiles (such as moisture) with increasing temperature. In this thesis, TGA was used to determine the carbon content in composite materials by heating them to a high temperature of 800 or 900ºC with a heating rate of 10 $^{o}C\ min^{-1}$ in air atmosphere. Here, a SETARAM Thermogravimetric Analyzer was employed. The loading amount of the sample material in the aluminium oxide crucible is 2-20 mg, depending on the density of the material.

3.5.6 Brunauer-Emmett-Teller Analysis

Brunauer-Emmett-Teller analysis is an effective tool for evaluating the specific surface area and pore size distribution of the sample material. It is based on the theory of physical adsorption of gas molecules on a solid surface. Using the Saito-Foley (SF) method, the pore size distribution curve of the sample material can be determined from the N_2 isotherms. In this thesis, to gain more accurate results, the sample has to be degassed before analysis, so as to remove trace H_2O in the sample. The measurements were performed at 77 K on a Quantachrome Autosorb-IQ MP instrument.

3.5.7 Scanning Electron Microscopy

Scanning electron microscopy (SEM) is applied primarily to produce images of electrode surface morphology or the topography of the powder materials. During SEM observation, the sample material is bombarded with a focused beam of electrons, and the electrons interact with atoms in the sample material. This could generate various signals which can be collected by the detector to provide information on the topography, composition, and other properties of the sample surface. The types of signals produced by SEM include those from secondary electrons, back-scattered electrons, characteristic X-rays, specimen currents, and transmitted electrons. The detectors for secondary electron are installed in all SEM systems, and SEM can offer images with resolution better than 1 nm when optimized.

The materials were observed with a field-emission scanning electron microscope (FE-SEM, JEOL JSM-7500FA, 15 kV). The samples for SEM observation were directly coated onto carbon conductive tape, which was mounted on an aluminium holder. For less conductive samples, their surfaces needed be sputter loaded by a highly conductive layer of platinum or gold to ensure the charge build up.

3.5.8 Transmission Electron Microscopy

Transmission electron microscopy (TEM) is a microscopy technique to study the morphology, lattice spacing, crystal orientation, and electronic structure of sample materials. During the observation, a beam of electrons is transmitted through an ultra-thin

sample, and the image is formed based on the interaction. TEM is capable of significantly higher resolution imaging than light microscopes, because of the small de Broglie wavelength of the beam electrons. Selected area electron diffraction (SAED) is a crystallographic experimental technique which is usually carried out inside the TEM. Here, the high-energy electrons behave in a wave-like, rather than a particle-like manner. For these electrons, the atoms in the crystalline sample act as a diffraction grating. Therefore, a portion of the electrons pass through the sample without deflection, and other electrons are scattered to particular angles, which are determined by the crystal structure of the material. From the scattering signal, a characteristic pattern of diffraction spots can be formed, with each spot related to a satisfied diffraction condition of the crystal structure.

In this thesis, the observations were conducted on a JEOL 2011 TEM (200 keV) and a JEOL ARM-200F TEM (200 keV). The TEM samples were ultrasonically dispersed in ethanol and loaded onto a holey carbon support film on a copper grid. The grid was then transferred onto a sample holder, which was paired with the specimen stage.

3.5.9 Energy-Dispersive X-Ray Spectroscopy

Energy-dispersive X-ray spectroscopy (EDS, EDX, or XEDS) is a complementary technique for the elemental analysis of a sample. It can identify the different elements, due to the fact that each element features a characteristic atomic structure. To stimulate the emission of unique X-rays from a specimen, a high-energy beam of electrons, X-rays, or protons is focused onto the sample being studied. In this thesis, EDX results in the SEM observations were collect by a Bruker X-Flash 4010 SSD energy-dispersive X-ray

spectrometer, and EDX data in the SEM observations were collected by a Centurio SSD energy-dispersive X-ray spectrometer. Detailed information on the morphology, elemental composition, and elemental mapping of the samples was yielded by the resulting spectra and images.

3.6 Electrochemical Characterization

3.6.1 Cyclic Voltammetry

Cyclic voltammetry (CV) is an electrochemical testing method to probe the thermodynamics and kinetics of the electron transfer during the reactions in an electrochemical cell. Typically, the CV curve is a function of potential versus the current response. In the process of a CV measurement, the working electrode potential is ramped linearly versus time, and the associated current is collected. Once a redox reaction takes place, an obvious peak can be found in the forward or reverse scans owing to the variations in the current value.

In this thesis, CV was used to demonstrate the reaction mechanisms of the electrodes composed of different materials. CV testing of coin cells is built on the two-electrode model, in which Li foil serves as both reference electrode and counter electrode. CV testing for rotating disk electrode system is built on the three-electrode model, in which a KCl saturated Ag/AgCl electrode and a platinum wire serve as the reference electrode and the counter electrode, respectively. CV results for the LIBs were recorded on a Biologic VMP-3 electrochemical workstation with a scan rate of 0.1 mV s^{-1} from 0 to 1.50 V. CV data for the LOB work were acquired on Princeton 2273 and 636 instruments

(Princeton Applied Research) with a scan rate of 10 mV s^{-1} in O_2 saturated 0.1 M KOH solution from 0.10 to -0.90 V and in Li-O_2 cells with the electrolyte consisting of 1 M $LiCF_3SO_3$ in TEGDME from 2.35 to 4.35 V.

3.6.2 Galvanostatic Charge and Discharge Measurement

The capacity and cycling stability of the electrodes for LIBs and LOBs were studied by galvanostatic charge/discharge tests using constant current mode. The charge or discharge capacity, which is the total electron charge in each process, was calculated from the applied current and the total accumulated time used to fully charge or discharge the cell. All the measurements were carried out on Land battery testers in air atmosphere for LIB measurements from 0 to 1.50 V (2.00 V) or in oxygen atmosphere for LOB measurements from 2.35 V to 4.35 V at room temperature. Rate performance could also be evaluated by applying various current densities over a number of cycles.

3.6.3 Electrochemical Impedance Spectroscopy

Electrochemical impedance spectroscopy (EIS) is a common technique to investigate electrochemical processes as a function of frequency, such as electron transfer, mass transport, and chemical reactions. EIS measurements could be carried out in potentiostatic (PEIS) or galvanostatic (GEIS) mode. In PEIS mode, impedance tests are performed by applying a sine wave around a potential E. Its value could be set to a constant value or a value that is associated with the equilibrium potential of the working electrode over a range of frequencies. Commonly, an impedance spectrum contains a high frequency semicircle corresponding to the kinetic processes and a low frequency tail related to the

diffusion processes, as shown in Figure 3.7. R_e, R_{ct}, C_{dl}, and W represent the uncompensated resistance, the charge transfer resistance, the constant phase angle element, and the Warburg impedance, respectively [145]. The GEIS mode is very similar to the PEIS mode, but its current is controlled instead of the potential.

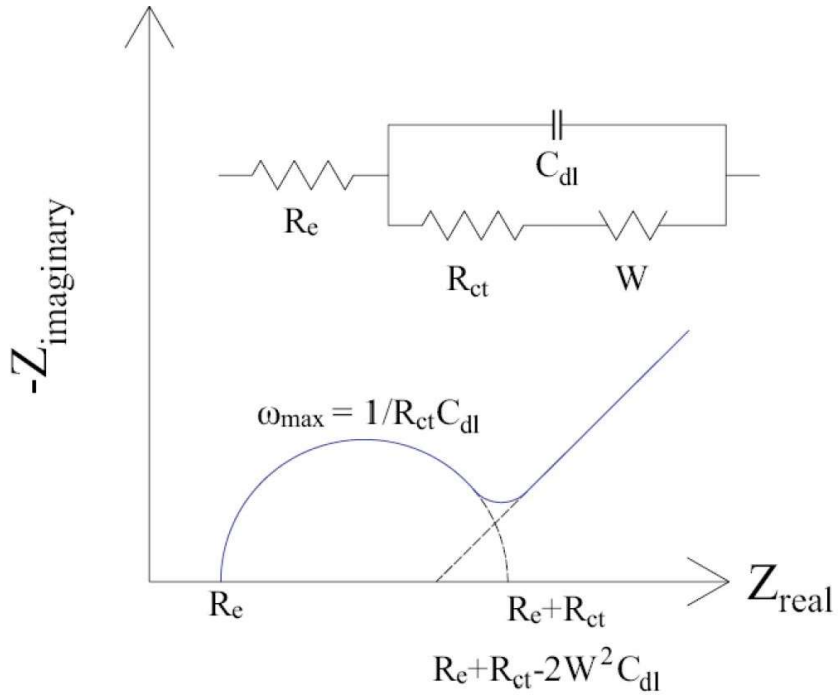

Figure 3.7 Typical schematic illustration of EIS and the related equivalent circuit for LIBs (inset) [145].

In this thesis, EIS data were recorded in PEIS mode on a CHI 660B electrochemical workstation with the Power Suite software package. The amplitude of sine wave used was 10 mV, and the frequency range was from 100.00 kHz to 0.01 Hz. The equivalent circuit has been evaluated by Zview software.

3.6.4 Linear Sweep Voltammetry

Linear sweep voltammetry is a voltammetric technique involving a single unidirectional voltage sweep. Similar to CV, LSV can detect the electric response at a constant rate when a voltage or series of voltages are applied to the electrode. In this thesis, the LSV method was utilized to acquire the steady state polarization curves of the catalyst material towards ORR and OER in 0.1 M KOH electrolyte with a scan rate of 10 mV s^{-1}.

3.6.5 Rotating Disk Electrode Measurement

The rotating disk electrode (RDE) technique is a powerful tool to investigate the characteristics and mechanisms of the redox reactions during the measurement. A three electrode system was used for this hydrodynamic voltammetry. The working electrode contains a conductive disk embedded in an inert non-conductive polymer or resin. It is connected to an electric motor that has very fine control of the electrode's rotation rate. The disk is commonly made of a noble metal or glassy carbon, but any conductive material can be used, based on specific needs. When the working electrode is rotated with certain angular velocity, the solution is dragged along by the rotating disk and the resulting centrifugal force flings the solution away from the centre of the electrode. The solution moves upwards from the bulk, perpendicular to the electrode, to replace the boundary layer. The overall outcome is laminar flow of the solution towards and across the electrode. The flow rate of the solution can be adjusted by the electrode's angular velocity and modelled mathematically. This flow can quickly achieve conditions in which the steady-state current is controlled by the solution flow rather than diffusion. By

applying RDE technique, many information on the characteristics and mechanisms of the reactions could be obtained, mainly including multi-electron transfer, the kinetics of a slow electron transfer, and adsorption/desorption steps.

In this thesis, an RDE system was applied to investigate the ORR and OER on Princeton 2273 and 636 instruments (Princeton Applied Research) in a standard three electrode cell at room temperature. The reference electrode and the counter electrode were a KCl saturated Ag/AgCl electrode and a platinum wire, respectively. The working electrode was prepared by mounting the samples onto a pre-polished GC electrode (5 mm in diameter).

CHAPTER 4 GERMANIUM/SINGLE-WALLED CARBON NANOTUBE COMPOSITE PAPER AS A FREE-STANDING ANODE FOR LITHIUM-ION BATTERIES

4.1 Preface

Because of their environmental friendliness, large energy density, high operating voltage, and long cycling lifetime, LIBs have become one of the most heavily employed mobile energy sources in today's world[146, 147]. Recently, consumer demand has been driving research efforts on small, thin, lightweight, and bendable LIBs to meet the various design and power needs of modern flexible electronic devices, such as roll-up displays, active radio-frequency identification tags, integrated circuit smart cards and implantable medical devices[148-150]. As an important part of LIBs, the anode consists of a metal substrate coated with a mixture of an active material, an electrical conductor, a binder, and a solvent. This type of anode is not suitable for flexible or bendable LIBs because it suffers from serious cracking and damage caused by the weak bonding between the metal substrate and the other materials during frequent bending. To avoid this drawback and lower the cost of LIBs, the development of free-standing anode materials is required[151, 152].

The pure single-walled carbon nanotube (SWCNT) paper anode has shown favourable flexibility and conductivity, and hence, is very suitable for producing free-standing anodes[153, 154]. Current research to develop free-standing SWCNT paper anode takes advantage of its unique electrical and structural properties, such as light weight, high conductivity, good cycling stability, and high mechanical strength in Li cells[155, 156].

Although SWCNT paper anode has several advantages, its energy density is limited due to the low practical capacity. Therefore, the hybridization of an active second phase with SWCNTs is expected to introduce high capacity and good cycleability.

Composites with SWCNTs, such as Si/SWCNT[157, 158], Fe_2O_3/SWCNT[159, 160], SnO_2/SWCNT[161], and MnO_x/SWCNT[162] have been reported as paper anode materials. Although electrochemical performance achieved by these already studied composite paper anodes was attractive, most of the preparation routes are too complicated or require high reaction temperature, limiting their industrial implementation. Therefore, it is of great interest to synthesize a new composite paper anode material by a green and efficient method at a low temperature.

I designed and prepared a novel free-standing Germanium (Ge)/SWCNT composite paper anode based on the following ideas:

(i) SWCNTs could serve as a highly electrical conductive and flexible matrix, which not only provides good electrical contact for the whole paper anode, but also effectively accommodates huge volume changes of the Ge particles during the cycling.

(ii) Ge as the electrochemically active second phase (1600 mAh g^{-1} theoretical capacity) could play an important role in improving the capacity of the SWCNT composite paper anode. In addition, Ge has been intensively studied recently due to its 400 times faster Li diffusivity and 104 times higher electrical conductivity than the commonly and widely studied silicon[46, 163, 164]. This makes it a promising candidate for composites with SWCNTs for use as a free-standing anode.

(iii) Utilizing a simple and efficient method to prepare a free-standing Ge/SWCNT composite paper without current collector and any binder could be useful for the fabrication of bendable batteries.

R. A. DiLeo's group[165] has reported a free-standing Ge/SWCNT anode prepared by depositing Ge onto SWCNT paper using an electron-beam evaporation method, and the results show a stable discharge capacity within 10 cycles. This method may cause high energy consumption and present a safety risk, however. Moreover, the thin film anode with bilayer structure tends to suffer from contact problems, and its electrical conductivity thus decreases, which leads to poor electrochemical performance.

In this work, a facile preparation method was developed to construct a three-dimensional architecture from a combination of nanostructured Ge particles and SWCNTs. The paper anode with good Ge nanoparticle distribution in the SWCNT network offers better electrical contact, which aids in improving the capacity and cycling stability for superior anodes in LIBs.

4.2 Experimental

4.2.1 Preparation of the Ge/SWCNT Composite Papers

To prepare the Ge/SWCNT composites, SWCNTs (purchased from UnidymTM) and 1 wt.% Triton X-100 surfactant were first added into 50 mL distilled water and ultrasonically treated for 2 h. The suspensions were then mixed with 10 mL 0.15 M NaOH solutions with GeO_2 dissolved in them, followed by constant stirring for 30 min.

Subsequently, the pH of the homogeneous solutions was adjusted to 7 using 0.5 M HCl. The solutions were added dropwise into 10 mL 0.32 M icy cold $NaBH_4$ solutions (~ 4 ºC) under continuous magnetic stirring, and then transferred to water baths at 60 ºC for 3 h. By using this method, three Ge/SWCNT composites were fabricated using 24, 36 and 54 mg GeO_2 precursor with the same amount of SWCNT (25mg). Specifically, these GeO_2 could be theoretically converted to 17, 25, 38 mg Ge, calculated based on the ratio between the molecular weight of Ge and GeO_2. The designed Ge percentages in the Ge/SWCNT composites above correspond to 40, 50, and 60 wt.%, which are designated as Ge/SWCNT-1, Ge/SWCNT-2, and Ge/SWCNT-3, respectively. The pure Ge particles used in the characterization for reference were synthesized by the same method without SWCNTs.

To make uniform papers, the as-prepared composite suspensions were filtered through porous polyvinylidene fluoride (PVDF) membranes by positive pressure provided by a vacuum pump. As the solvent could pass through the pores, the Ge/SWCNT composites were trapped on the membrane surfaces, forming entangled mats. The mats were washed twice with distilled water, followed by ethanol to remove the remaining surfactant. The mats were allowed to dry at 60 ºC overnight in a vacuum oven. Finally, they were peeled off from the PVDF membranes, and the Ge/SWCNT composite papers were obtained. For comparison, the pure SWCNT paper was prepared by the same method without Ge precursor.

4.2.2 Physical Characterization

XRD (GBC-MMA) patterns were collected from the samples with Cu Kα radiation at a scanning rate of 5° min^{-1} within the 2θ range from 20° to 80°. Raman spectroscopy

(JOBIN YVON HR800 Confocal system with 632.8 nm diode laser excitation) was conducted using a 300 lines mm^{-1} grating in the range of 200 to 2000 cm^{-1} at room temperature. The morphologies of the samples were examined by FE-SEM (JEOL 7500, operated at an acceleration voltage of 1.5 kV) and TEM (JEOL EM 2010). The sample for TEM observation was prepared by dispersing a small piece of the Ge/SWCNT composite paper onto a holey carbon support.

4.2.3 Electrochemical Measurements

The 1×1 cm square anodes were cut out from the as-prepared papers. The electrochemical cells (CR 2032 coin-type cells) were assembled in an argon gas filled glove box (Mbraun, Germany) by stacking a porous polypropylene separator between the paper anode as the working anode and the Li foil as the counter and reference electrode. The electrolyte was 1 M $LiPF_6$ in a 50:50 (v/v) mixture of ethylene carbonate (EC) and diethyl carbonate (DEC). The electrochemical cells were galvanostatically discharged and charged using a Land battery tester within a voltage range of 0.01 to 2.00 V at a current density of 25 mA g^{-1} and a temperature of 25 ºC. Electrochemical impedance spectroscopy (EIS) was carried out utilizing a CHI 660B electrochemical workstation.

4.3 Results and Discussion

XRD patterns for the pure SWCNT paper, the typical Ge/SWCNT composite paper and the pure Ge particles are shown in Figure 4.1(a). The diffraction peaks for SWCNTs at 2θ of 23° and 45° could be indexed as the (002) and (101) reflections[161]. The diffraction peak of the (002) diffraction is related to the typical random arrangement of CNTs, with

a d_{002} of 0.38 nm calculated based on Bragg's equation. The two broad diffraction peaks for the as-prepared Ge particles indicate the nanosized structure. The diffraction pattern of the Ge/SWCNT-2 paper contains two broad peaks as well, which is presumably attributable to the overlapping of SWCNT peaks with the Ge peaks. Raman spectroscopy, as shown in Figure 4.1(b), was used to further confirm the presence of Ge particles and SWCNTs in the paper. The Raman spectrum of SWCNTs shows characteristic bands in the radial breathing modes (RBM) region of the low frequency range below 290 cm^{-1}, the disorder induced phonon mode (D-band) at about 1306 cm^{-1}, and the tangential modes (G-band) with G^- and G^+parts at 1554 cm^{-1} and 1593 cm^{-1}. In the Raman spectra of the composite paper, Ge bands located in 298 cm^{-1} can be identified, together with the typical SWCNT bands. This implies that the Ge/SWCNT composite papers could be successfully prepared via the method mentioned above.

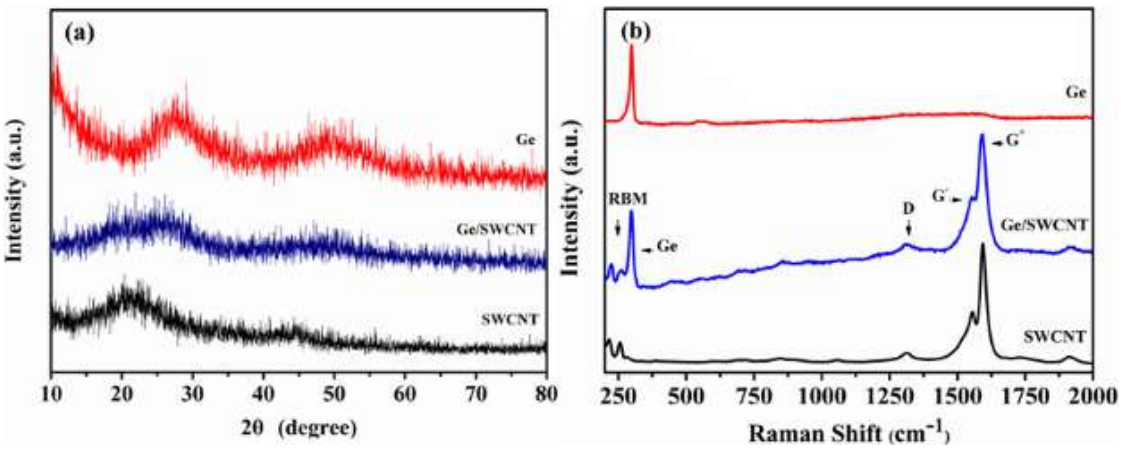

Figure 4.1 XRD patterns (a) and Raman spectra (b) of the pure SWCNT paper, the Ge/SWCNT-2 paper and the pure Ge particles.

FE-SEM images of the pure SWCNT paper and the Ge/SWCNT-2 paper are shown in Figure 4.2. In the surface morphology of the SWCNT paper (Figure 4.2(a)), the SWCNTs

appear as a web of bundled and well-packed nanotubes, forming a three-dimensional network structure. Ge particles are deposited onto the SWCNT matrix in the form of both individual particles (about 10-30 nm in diameter) and clusters of particles, as shown in Figure 4.2(b). The cross-sectional view of the Ge/SWCNT composite paper (Figure 4.2(c) and (d)) demonstrates that it is composed of very dense, closely connected multilayers, and the total thickness is around 34 μm. The Ge nanoparticles which are distributed on the SWCNT matrix can be seen clearly. The Ge/SWCNT composite paper can be rolled up or bent freely (inset of Figure 4.2c), indicating its good flexibility and mechanical property.

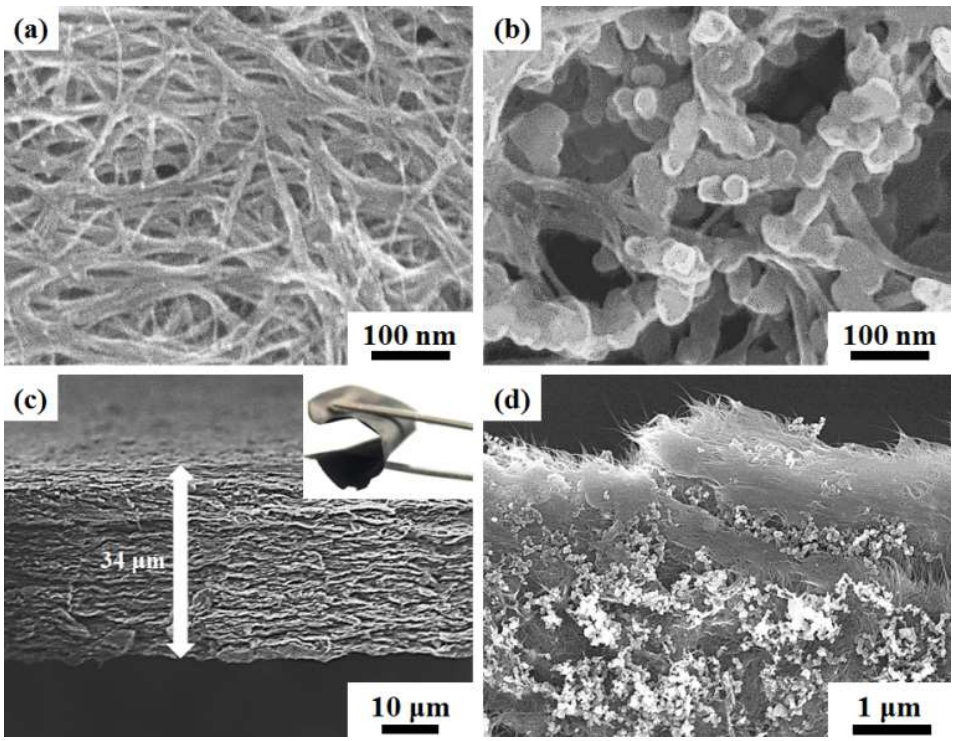

Figure 4.2 FE-SEM images the pure SWCNT paper and the Ge/SWCNT-2 paper: top views of the pure SWCNT paper (a) and the composite paper (b); cross-sectional views of the composite paper at low magnification (c) and at high magnification (d); inset of (c) is a photograph of the composite paper.

A FE-SEM image with the corresponding EDS spectrum and EDS mapping images for the Ge/SWCNT-2 paper is presented in Figure 4.3. The EDS spectrum (Figure 4.3(b)) shows the presence of SWCNTs (C) and Ge in the Ge/SWCNT-2 paper, and the percentage of Ge is 32 wt.%. O is detected from the oxygenated functional groups, and Fe is the catalyst in the SWCNTs. The percentages of Ge in the Ge/SWCNT-1 paper and Ge/SWCNT-3 paper were also analysed from EDS spectrum to be 22 and 45wt.%, respectively. The coloured points in the EDS mapping images (Figure 4.3(c) and (d)) confirm the presence of the elements Ge and C, respectively. Furthermore, the results show the good distribution of Ge in the paper, which demonstrates that the Ge nanoparticles have been homogeneously coated onto the surface of the SWCNTs.

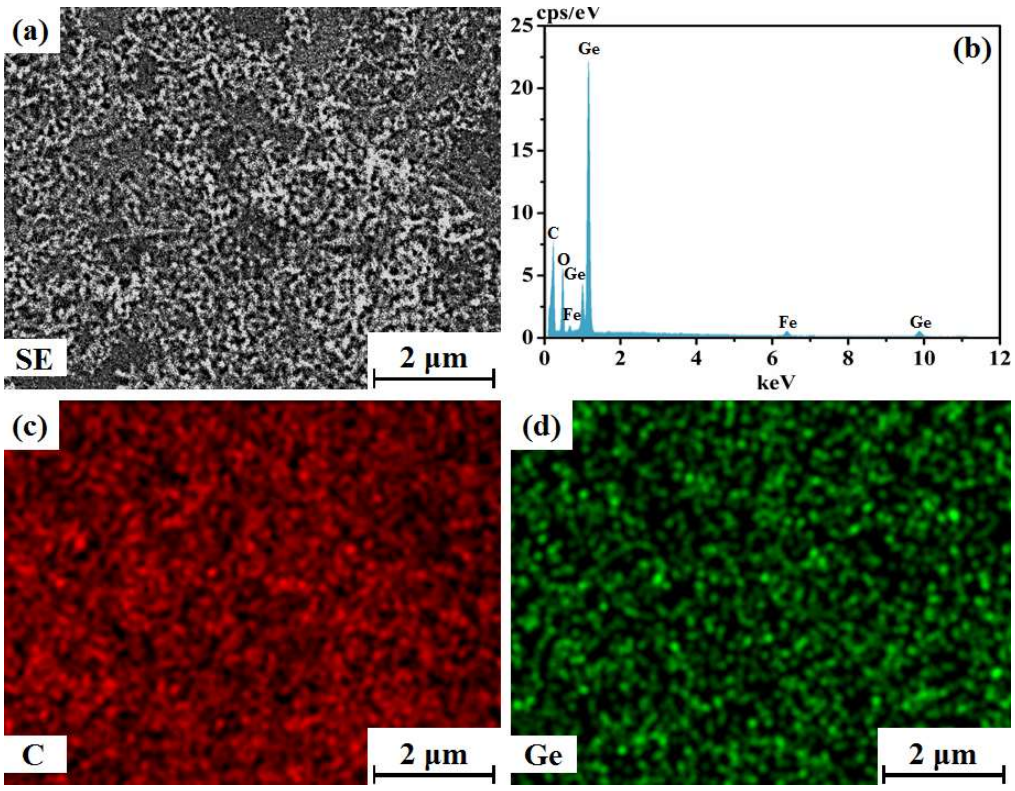

Figure 4.3 FE-SEM image of the Ge/SWCNT-2 paper (a) with EDS spectrum (b), and corresponding EDS mapping of carbon and Ge (c, d).

TEM investigations (Figure 4.4) revealed information on the morphology and structure of the Ge/SWCNT-2 paper. The low magnification image in Figure 4.4(a) gives further support to the observation that the surfaces of the SWCNTs are fully covered by Ge nanoparticles. The corresponding selected area electron diffraction (SAED) pattern is shown in Figure 4.4(b). The indexed fine spotty rings in the SAED correspond to structural characteristics of cubic Ge, indicating that the growth directions of the Ge nanoparticles are parallel to the (111), (220), and (311) planes (JCPDS NO.: 65-0333). The high magnification TEM image (Figure 4.4(c)) clearly shows a Ge particle, the SWCNTs, and the boundary between the Ge particle and the SWCNTs. The SWCNT interplanar distance was measured to be 0.35 nm, in agreement with the (002) planes of SWCNTs. Figure 4.4(d) displays lattice fringes of a typical Ge particle with a lattice spacing of 0.20 nm, corresponding to the spacing of the (220) planes of Ge.

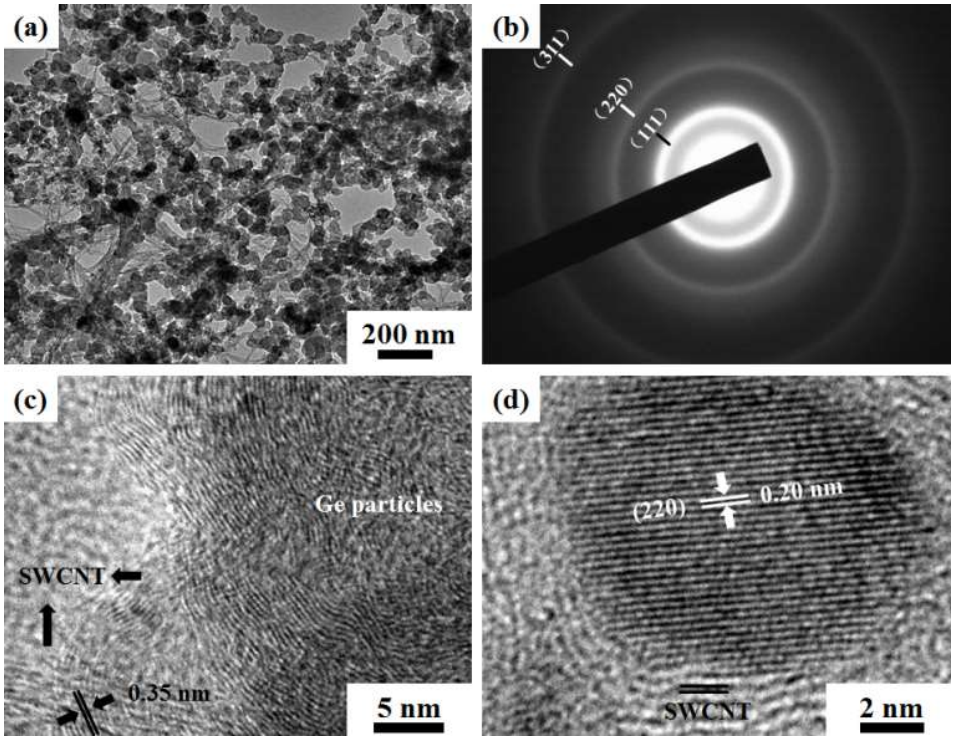

Figure 4.4 TEM images obtained from the Ge/SWCNT-2 paper: low magnification image (a) and associated SAED pattern (b); high magnification TEM image showing the lattice

and interface between a Ge nanoparticle and SWCNTs (c), and lattice resolved high magnification TEM image of a Ge nanoparticle on SWCNTs (d).

Figure 4.5 shows selected charge-discharge curves and their corresponding differential profiles for the sample anodes in coin cells at a current density of 25 mA g^{-1} between 0.01 and 2.00 V vs. Li/Li^+. Here, the result for the Ge/SWCNT-2 paper anode is selected as the typical composite data to compare with that for the pure SWCNT paper anode. As can be seen in Figure 4.5(a), the initial discharge and charge capacities of SWCNT paper anode are 1307 and 289 mAh g^{-1}, respectively, with a coulombic efficiency of 22%. The irreversible capacity loss is mainly due to the reduction of dioxygen molecules or oxygenated functional groups on the surface of the SWCNT paper anode, the formation of a solid electrolyte interphase layer, and further side reactions[30]. Subsequently, the pure SWCNT paper anode shows a relatively stable discharge capacity after the 2nd cycle, with an average coulombic efficiency of > 97 % up to 40 cycles.

The peak at 0.8-0.9 V in the first discharge differential plot (Figure 4.5(b)) corresponds to the voltage plateau in the first discharge cycle, which is associated with electrolyte decomposition and the formation of the SEI layer mentioned above. The pronounced potential below 0.4 V is attributed to the insertion of Li ions into the graphitic-type layers, which has been confirmed by previous reports[166-168]. No evident peak can be traced in the following cycles, indicating the irreversible reaction. As can be seen in Figure 4.5(c), the Ge/SWCNT composite paper anode exhibits an initial discharge capacity of 2024 mAh g^{-1}, with a coulombic efficiency of 33%, which is calculated based on the total mass of the paper anode. The paper anode delivers a discharge capacity of 752 mAh g^{-1} in the

second cycle, and the capacity loss mainly arises from the irreversible Li ion insertion into the paper anode and the formation of the SEI layer. Three peaks can be observed in

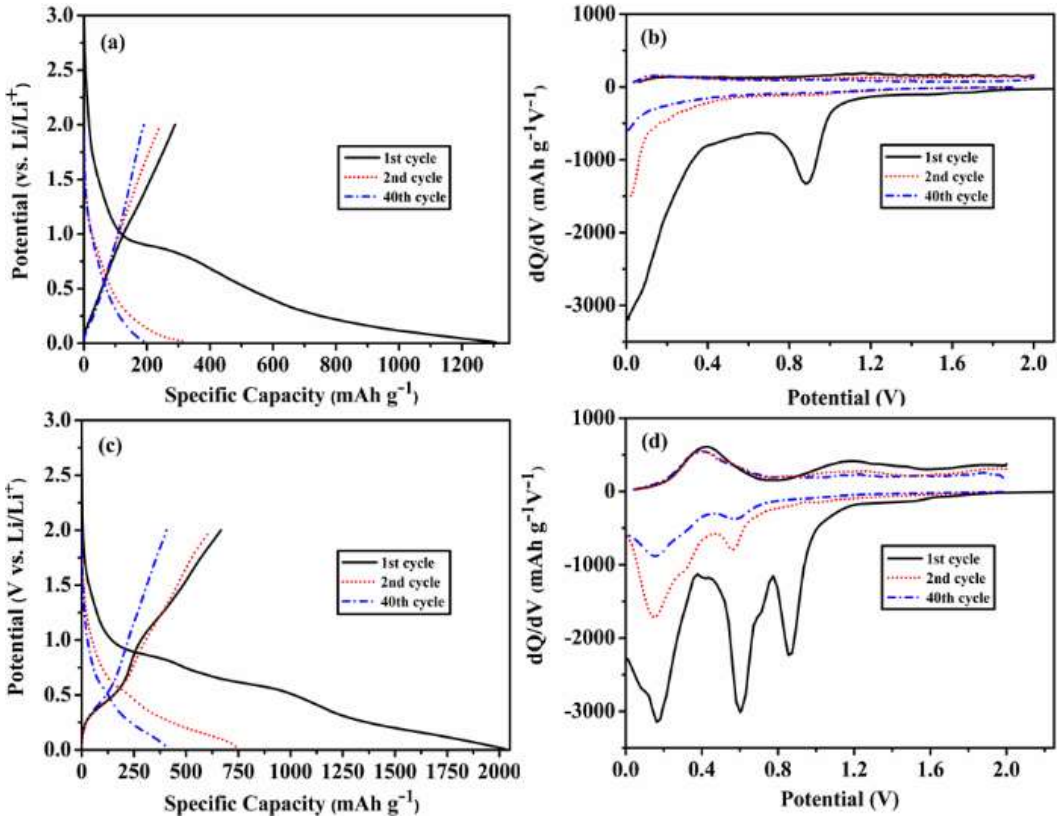

Figure 4.5 Charge-discharge curves for selected cycles and their differential profiles for the pure SWCNT paper anode (a, b) and the Ge/SWCNT-2 paper anode (c, d) at current density of 25 mA g^{-1}.

the differential curve (Figure 4.5(d)) of the first discharge cycle. The SEI layer formation occurs at the same voltage of 0.8-0.9 V as that in the SWCNT paper anode, and the other two peaks at 0.5-0.6 V and 0.1-0.2 V represent the stepwise Li alloying reaction to form different Li_xGe alloys. The differential curves of the subsequent charge cycles show a broad anodic peak at about 0.45 V, corresponding to the delithiation voltage of Li_xGe species[169-171]. Multiple sharp peaks in typical cycles still exist up to 40 cycles, though the intensity of the peaks have been much reduced, suggesting that the paper anode could

maintain good kinetic activity towards Li ion intercalation/ deintercalation during the cycling.

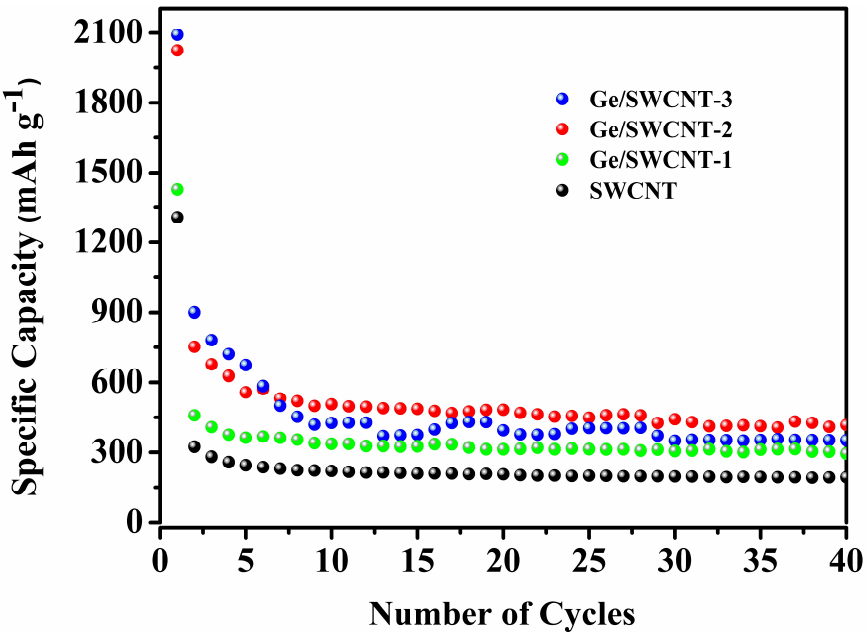

Figure 4.6 Cycling stability of the pure SWCNT paper anode and different Ge/SWCNT composite paper anodes at current density of 25 mA g^{-1}.

To study the synergic effects between the electrical conductive SWCNTs and second active phase Ge nanoparticles, the cycling stability of the pure SWCNT paper anode and the paper anodes with various Ge weight percentages were examined as shown in Figure 4.6. The discharge capacities of the Ge/SWCNT-1, Ge/SWCNT-2, Ge/SWCNT-3 paper anodes are 295, 350, 417 mAh g^{-1} after the 40 cycles, respectively. Among different Ge/SWCNT composite paper anodes, it is noted that the Ge/SWCNT-2 paper anode delivers the highest discharge capacity, which is 117% higher than that of the SWCNT paper anode (192 mAh g^{-1}). The main reason is that proper percentage Ge nanoparticles in the composite paper anode could serve as an electrochemically active second phase to

effectively increase its discharge capacity. Moreover, mechanically robust SWCNTs in the paper anode can keep the Ge nanoparticles in good contact and mitigate the material failure caused by the volume changes of Ge nanoparticles. In addition, due to the excellent ion and electron transfer properties of SWCNTs, the accessibility to Li ions and the electrical conductivity of the paper anode could also be maintained.

The Ge/SWCNT-1 paper anode shows lower discharge capacity because of less active material Ge loading. The Ge/SWCNT-3 paper anode also delivers lower discharge capacity and unstable cycling performance, which could possibly be due to inefficient ion and electron transfer in the paper anode and mechanical issues attributable to the volume changes of Ge particles during cycling. Therefore, the optimum Ge nanoparticle content in the composite paper anode is 32 wt.%. Similar synergic effects were also observed in other composite paper systems[148, 150].

Electrochemical impedance spectroscopy (EIS) measurements for the pure SWCNT paper anode and the Ge/SWCNT-2 paper anode were conducted using a sine wave of 10 mV amplitude over a frequency range of 100 kHz-0.01 Hz. To maintain uniformity, the impedance measurements were performed after running charge-discharge for 5 cycles and 40 cycles in the fully charged state. The Nyquist plots and the fitting model using an equivalent circuit are depicted in Figure 4.7(a), with the equivalent circuit as the inset. Both plots display one compressed semicircle in the high frequency region and a sloping line in the low frequency regime. The intercept on the Z_{real} axis in the high frequency region represents the total resistance of the electrolyte, separator, and electrical contacts. The semicircle in the high frequency range indicates the charge transfer resistance (R_{ct}), which is associated with the charge transfer reaction at the electrode/electrolyte interface.

The inclined line in the low frequency region represents the Warburg impedance (Z_w), related to the ion diffusion process in the anode materials[172, 173].

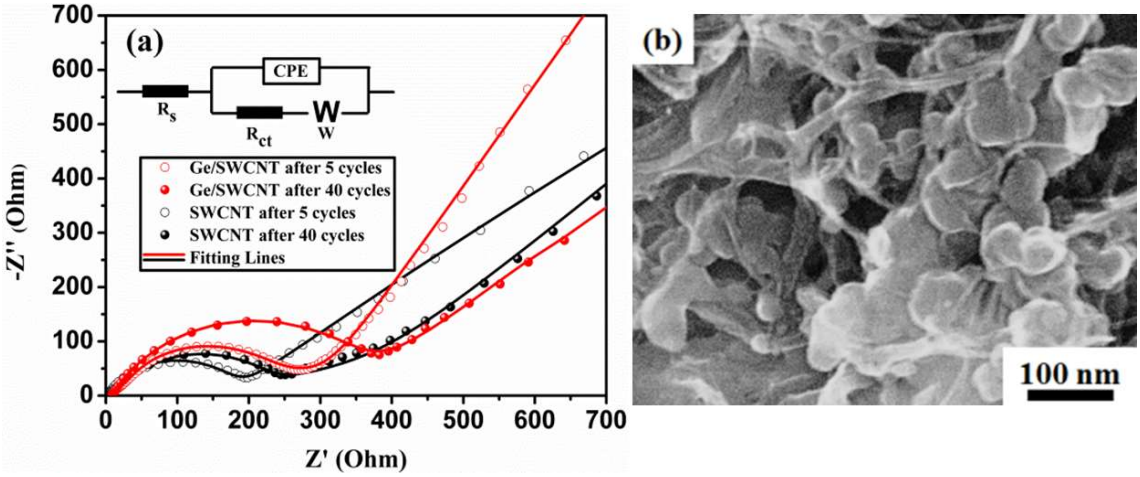

Figure 4.7 Impedance spectra for the pure SWCNT paper anode and the Ge/SWCNT-2 paper anode after 5 cycles and after 40 cycles, with the inset containing the equivalent circuit model (a). FE-SEM image of the Ge/SWCNT-2 paper anode after 40 cycles (b).

Apparently, the diameters of the semicircles for the pure SWCNT paper anode are smaller than those for the Ge/SWCNT composite paper, indicating lower charge transfer resistance of the SWCNT paper anode after 5 (211.3 Ω) and 40 cycles (279.2 Ω). This result further confirms that the SWCNTs could serve as a highly electrical conductive matrix and provide three-dimensional electron pathways for the paper anode. The Ge/SWCNT-2 paper anode also shows a low charge transfer resistance after 5 cycles (290.3 Ω). This is because good dispersion of the electrochemically active phase Ge nanoparticles at the surface of the SWCNTs could enable efficient charge transport at the electrode/electrolyte interface as well, and the SWCNTs in the paper anode possess a large surface area, which could relieve the volume changes of Ge nanoparticles during the charge and discharge processes. After 40 cycles, agglomerates are found to have

formed on some parts of the Ge/SWCNT-2 paper anode (shown in Figure 4.7(b)), and this will reduce the area of the interparticle contact between the Ge nanoparticles and the SWCNTs, resulting in higher charge transfer resistance (413.5 Ω) of the Ge/SWCNT composite paper anode.

4.4 Conclusions

In the Ge/SWCNT composite papers, SWCNTs form robust three-dimensional architectures with nanosized Ge particles uniformly deposited on the surface of SWCNTs. Compared with previous works of SWCNT-based paper anodes, the Ge/SWCNT composite paper anode with a relatively low active phase content (32 wt.%) was synthesized by a simpler and low temperature route, and delivers a satisfactory reversible discharge capacity of 417 mAh g^{-1} after 40 cycles. The improved electrochemical performance of the Ge/SWCNT composite paper anode can be attributed to the good distribution of high capacity Ge in the SWCNT network, which increases the paper anode's electrical conductivity, provides void space to buffer the Ge nanoparticle volume changes, so as to enable more efficient channels for the Li insertion and deinsertion during the charge-discharge processes.

CHAPTER 5 IN-SITU ONE-STEP HYDROTHERMAL SYNTHESIS OF A LEAD GERMANATE-GRAPHENE NANOSHEET COMPOSITE AS A NOVEL ANODE MATERIAL FOR LITHIUM-ION BATTERIES

5.1 Preface

LIBs have been mainly used for portable electronics, but their use is now being extended to large-scale energy storage, such as in power tools and vehicle electrification[174-176]. In order to further improve the performance of LIBs, high energy density materials are desired, since graphite, the commercial anode, possesses low practical capacity. Ge has been intensively researched as an alternative anode material, owing to its high theoretical capacity (1600 mAh g^{-1}), low working potential, and high Li ion diffusivity (400 times higher than that of the well-studied Si)[31, 47]. This makes Ge a promising anode material for both high energy and high power applications. Pure Ge anode suffers from rapid capacity loss, however, accompanied by a huge irreversible capacity. The main reason is that the dramatic Ge volume changes and agglomeration during Li insertion/extraction processes lead to the pulverization and exfoliation of the active material, electrically isolating the particles from the current collector and degrading their cycling performance[170, 177].

Tremendous efforts have been made to address this issue, including reducing the anode material to the nanoscale, construction of porous architectures, and amorphization of the anode material[53, 178-180]. Recently, it has been proposed that preparing metal germanate nanowires or nanobelts could be a strategy to mitigate these problems[59, 181, 182]. The metal

oxide matrix could provide an elastic buffer to accommodate the volume changes and prevent the agglomerations of nanosized Ge particles formed *in-situ* in the matrix after the initial discharge process, which could be helpful for improving the electrochemical performance of this material. Pb is a highly abundant element around the world, and its compounds exhibit good electrochemical performance as anode for LIBs[183, 184], making $PbGeO_3$ an anode candidate to satisfy the growing demand for various energy-storage technologies. Although Pb is heavy and toxic, its negative effect could be avoid by strictly following the widely-used Lead-Acid battery collection and recycling rules in force in most countries. Since $PbGeO_3$ is actually an alkaline earth metal oxide, it is low in electrical conductivity, and its electrochemical performance is limited. $PbGeO_3$/PPy composites were reported to be prepared via a hydrothermal polymerization-coating method[185]. This technique is quite complicated and time-consuming, however, and the cycling stability and rate capability of the composites need to be improved. Therefore, it is still necessary to explore simple synthesis methods and an effective matrix for the formation of $PbGeO_3$ nanocomposite anode materials.

Graphene nanosheets (GNS), as two-dimensional macromolecular sheets of carbon atoms with a strongly bonded carbon network, have aroused explosive interest for energy-storage applications because they feature superior electrical conductivity, large theoretical specific surface area, and chemical tolerance, as well as remarkable structural flexibility[186-188]. In the light of its fascinating advantages, it has been suggested that GNS could be an ideal substrate for the growth of functional nanomaterials for Li storage. The hydrothermal method for preparing oxides and their composites with GNS is widely utilized because it allows control of the chemical composition, particle shape, and crystallite size in a simple and efficient way[58, 189-191]. The *in-situ* one-step hydrothermal

method can produce an *in-situ* coating of $PbGeO_3$ nanowires on wrinkled GNS and also simplify the synthesis method to reduce the cost and energy consumption.

Herein, a facile one-step hydrothermal method is employed to synthesize $PbGeO_3$-GNS composite as a novel anode material for LIBs. The metal oxides formed *in situ* after the initial discharge could help to alleviate the volume expansions during the Li ion uptake/release. Moreover, the reversible reaction between Ge and Li_2O is presumed to improve the Li storage performance. Furthermore, the combination with the GNS enables fast electron migration for the Li-ion uptake/release in $PbGeO_3$, contributing to enhanced Li storage kinetics. In addition, embedding $PbGeO_3$ nanowires in the GNS matrix could also maintain the structural integrity of the composite anode by preventing large volume changes and particle agglomerations during cycling. Consequently, the composite anode exhibits superior electrochemical properties in terms of specific capacity, cycling stability, and rate capability compared to the pure $PbGeO_3$ anode.

5.2 Experimental

5.2.1 Synthesis of the $PbGeO_3$-GNS Composites

GO was synthesized from natural graphite powder (Fluka) according to a modified Hummers method, as reported elsewhere[192]. To prepare the $PbGeO_3$-GNS composites, 50 mg GO and $Pb(CH_3COO)_2 \cdot 3H_2O$ were first added into 50 mL distilled water and ultrasonically treated for 1 h. The suspension was then mixed with 10 mL GeO_2 solution, followed by constant stirring for 30 min. The mixed solution was then transferred into a 100 mL autoclave with a Teflon liner. The autoclave was maintained at 180 °C for 24 h, and then rapidly cooled to room temperature in air. The final products ware collected,

washed with deionized water and ethanol three times, and dried in a vacuum oven at 60 °C for 12 h. By using this method, three $PbGeO_3$-GNS composites were fabricated using 0.15, 0.3 and 1.5 mmol $Pb(CH_3COO)_2 \cdot 3H_2O$, respectively, and GeO_2 precursor solution with the same amount of GO (50 mg). The composites above are designated as $PbGeO_3$-GNS1, $PbGeO_3$-GNS2, and $PbGeO_3$-GNS3, respectively. The pure GNS and the $PbGeO_3$ were also synthesized by the same method for comparison without the precursor solution and the GO, respectively.

5.2.2 Characterization

XRD patterns were collected on a GBC MMA generator and diffractometer with Cu Kα radiation. IR spectroscopy was conducted using a Shimadazu IRPrestige-21 Fourier transform IR (FT-IR) spectrometer with KBr as the background file. The morphologies of the samples were examined by FE-SEM (JEOL 7500) and TEM (JEOL ARM-200F). High-angle annular dark-field (HAADF) STEM images and corresponding element mapping images were collected with the same TEM equipped with a Centurio SSD EDS detector. TGA was performed using a SETARAM Thermogravimetric Analyzer (France).

5.2.3 Electrochemical Measurements

CR 2032 coin-type cells with the working electrode containing 80 wt.% active materal, 10 wt.% carbon black, and 10 wt.% carboxymethyl cellulose (CMC) on copper foil were assembled in an Ar-filled glove box (Mbraun, Unilab, Germany), using Li metal foil as the counter electrode. The electrolyte used in assembling the cells and washing the electrodes for ex-situ XRD was $LiPF_6$ (1 M) in a 50:50 (v/v) mixture of ethylene

carbonate (EC) and diethyl carbonate (DEC). Cyclic voltammetry (CV) was conducted on an electrochemistry workstation (Biologic VMP-3). The specific capacities were calculated based on the amount of active material in the electrode. Electrochemical impedance spectroscopy (EIS) was carried out utilizing a CHI 660B electrochemical workstation.

5.3 Results and Discussion

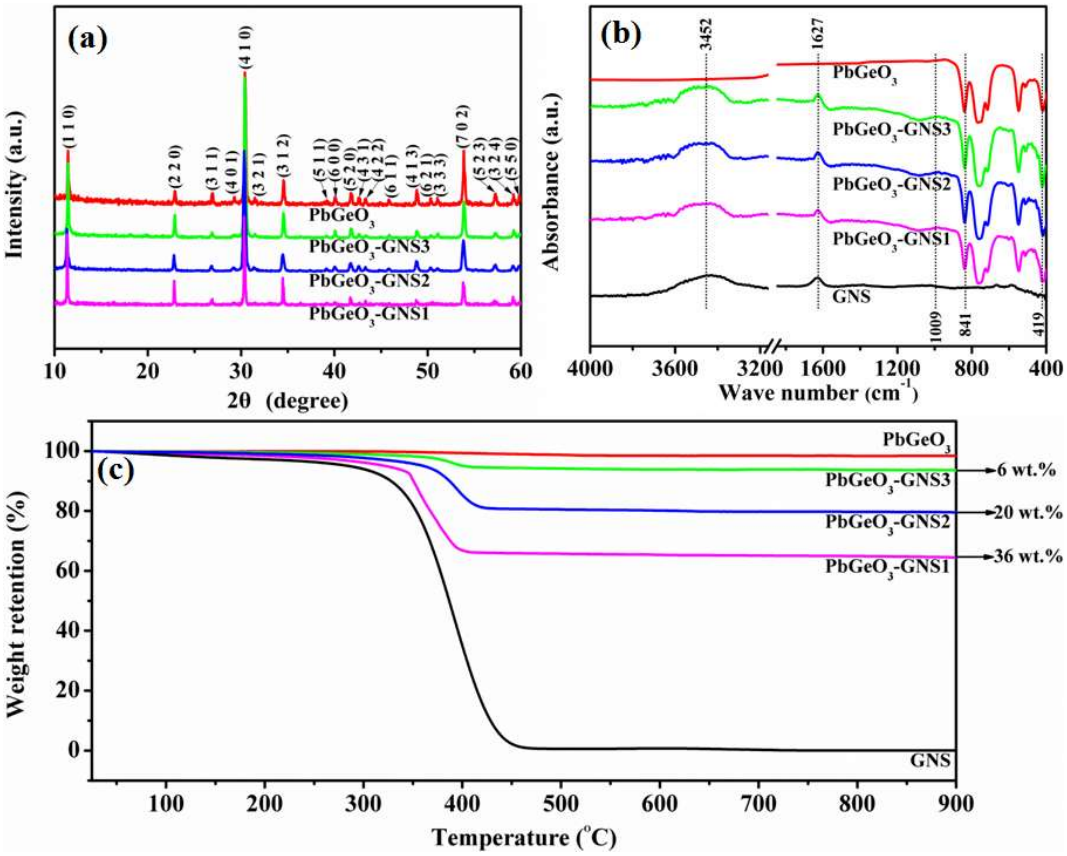

Figure 5.1 (a) XRD patterns of the pure $PbGeO_3$ and the $PbGeO_3$-GNS composites; (b) FT-IR spectra of the pure $PbGeO_3$, the $PbGeO_3$-GNS composites, and the GNS; and (c) TGA curves of the pure $PbGeO_3$, the $PbGeO_3$-GNS (36, 20, and 6 wt.% of GNS) composites, and the GNS.

XRD patterns and FT-IR spectra for the pure $PbGeO_3$ and the $PbGeO_3$-GNS composites are presented in Figure 5.1(a, b). The XRD patterns of the composites show that all the diffraction peaks can be well assigned to the hexagonal phase with lattice constants a = 1.57 nm and c = 0.724 nm (JCPDS 38-1035). The strong and clear peaks indicate the high crystallinity of the $PbGeO_3$ in the composites. Further information on the pure $PbGeO_3$, the $PbGeO_3$-GNS composites, and the GNS was provided by the associated FT-IR spectroscopy. In the spectrum of the composites, the vibrations (transmittance peaks) located at 3452 cm^{-1} are related to the O-H stretching mode of intercalated water, and the vibrations (transmittance peaks) at around 1627 cm^{-1} can be ascribed to the C skeletal vibrations[193, 194]. In the range of 400-1000 cm^{-1}, the vibrations (absorbance peak) are attributed to the characteristic mode of $PbGeO_3$, and the vibrations at around 841 and 419 cm^{-1} correspond to Ge-O and Pb-O bonds, respectively[185]. It should be noted that the transmittance peaks centred at around 1009 cm^{-1} appear in all the composites, but they cannot be traced in the $PbGeO_3$ and GNS. This is because they are associated with the stretching vibration of C-O, which cannot be reduced due to its interaction with the growth sites of $PbGeO_3$[195, 196], indicating that $PbGeO_3$ is successfully anchored on the GNS by chemical bonds in the composites via the method mentioned above.

The weight percentages of the GNS in the $PbGeO_3$-GNS composites were obtained by means of TGA, as shown in Figure 5.1(c). The TGA was carried out from 25 to 900 ℃, with a heating rate of 10 ℃min^{-1} in air. Owing to the thermal stability of $PbGeO_3$, the pure $PbGeO_3$ remains stable, while the GNS was all burned out during the heating process. Therefore, the weight loss mainly results from the decomposition of the GNS, and the weight percent of the residue after 900 ºC is that of $PbGeO_3$ in the composite. Therefore,

the GNS contents of the samples denoted as $PbGeO_3$-GNS1, $PbGeO_3$-GNS2, and $PbGeO_3$-GNS3 can be estimated to be approximately 36, 20, and 6 wt.%, respectively.

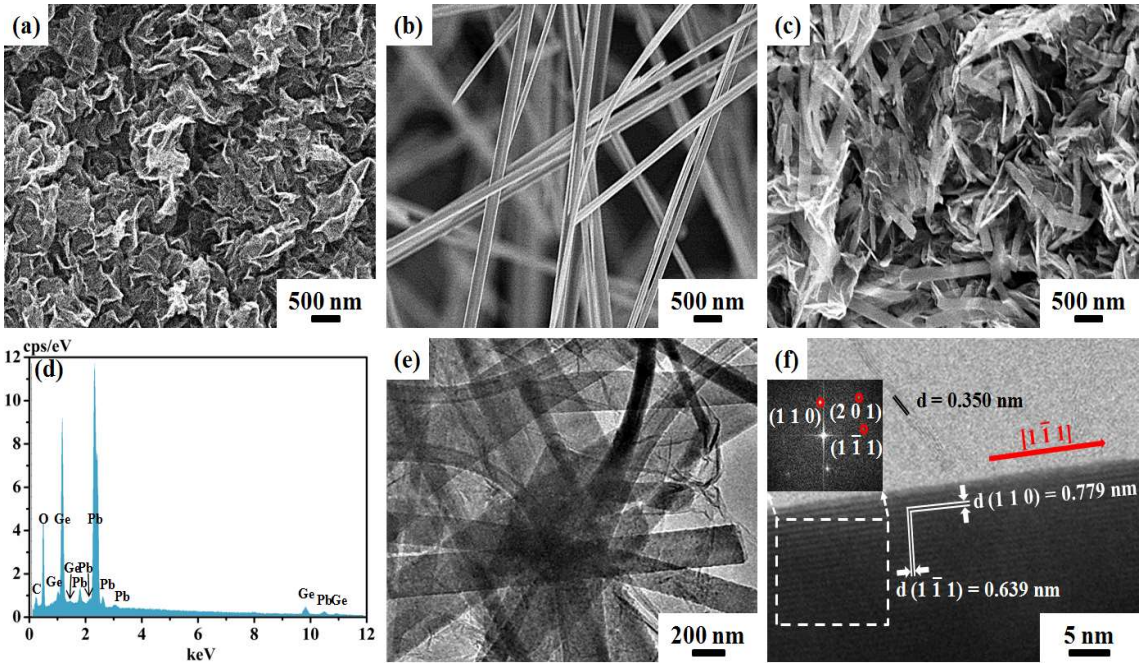

Figure 5.2 FE-SEM images of (a) the GNS, (b) the pure $PbGeO_3$, and (c) the $PbGeO_3$-GNS2 (20 wt.%) composite; (d) the corresponding EDS for (c); (e) large area TEM image of the $PbGeO_3$-GNS2 composite; and (f) HRTEM image of the $PbGeO_3$-GNS2 composite taken along a $PbGeO_3$ nanowire wrapped with GNS (inset is the fast Fourier transform diffractogram of the selected area).

To investigate the morphology of the materials obtained, FE-SEM was performed on the pure $PbGeO_3$, the $PbGeO_3$-GNS composite, and the GNS. Here, the observations for the $PbGeO_3$-GNS2 (20 wt.%) composite is included as the typical composite results. By comparing with pure GNS and the $PbGeO_3$ [Figure 5.2(a, b)], it can be seen clearly in Figure 5.2(c) that the $PbGeO_3$ nanowires with a diameter of about 100 to 200 nm and the GNS form a sandwich-like structure, in which the GNS restack and the $PbGeO_3$

nanowires are homogeneously distributed on or between the GNS. Figure 5.2(d) shows the associated EDS of the $PbGeO_3$-GNS2 composite. Only the elements Pb, Ge, O and C were detected in the composite, which further proves that there are no other impurities in the sample.

The transmission electron microscope (TEM) images in Figure 5.2(e) confirmed the FE-SEM results and showed that the $PbGeO_3$ nanowires were uniformly dispersed in the GNS to form the composite. The typical high-resolution TEM image in Figure 5.2(f) demonstrates that the $PbGeO_3$ nanowire was coated on the GNS with lattice spacing of 0.350 nm. The indexed diffraction spots in the fast Fourier transform pattern of the $PbGeO_3$ selected area can be indexed to the (110), (201), and $(1\bar{1}1)$ planes of the hexagonal phase, respectively, and it can be seen that the preferential growth of the $PbGeO_3$ is along the $[1\bar{1}1]$ direction. There is also evidence that the $PbGeO_3$ lattice stripes are separated by 0.779 and 0.639 nm, corresponding to the (110) and $(1\bar{1}1)$ planes, respectively.

Figure 5.3(a, b) shows cyclic voltammograms (CVs) of the $PbGeO_3$-GNS2(20 wt.%) anode and the pure $PbGeO_3$ anode. The $PbGeO_3$-GNS2 anode displays similar peak voltages to those of the pure $PbGeO_3$ anode during the first 5 cycles, where it is presumed that same charge and discharge reactions take place in the two anode materials. It can be seen, however, that the current density of the composite anode is much higher than that of the $PbGeO_3$ anode, and the CV curve of the $PbGeO_3$-GNS2 anode also exhibits better overlapping. That is because the $PbGeO_3$-GNS2 anode offers better kinetic properties, resulting from the GNS wrapping, which greatly improves the electronic interparticle connections and prevents agglomeration during cycling[39, 194].

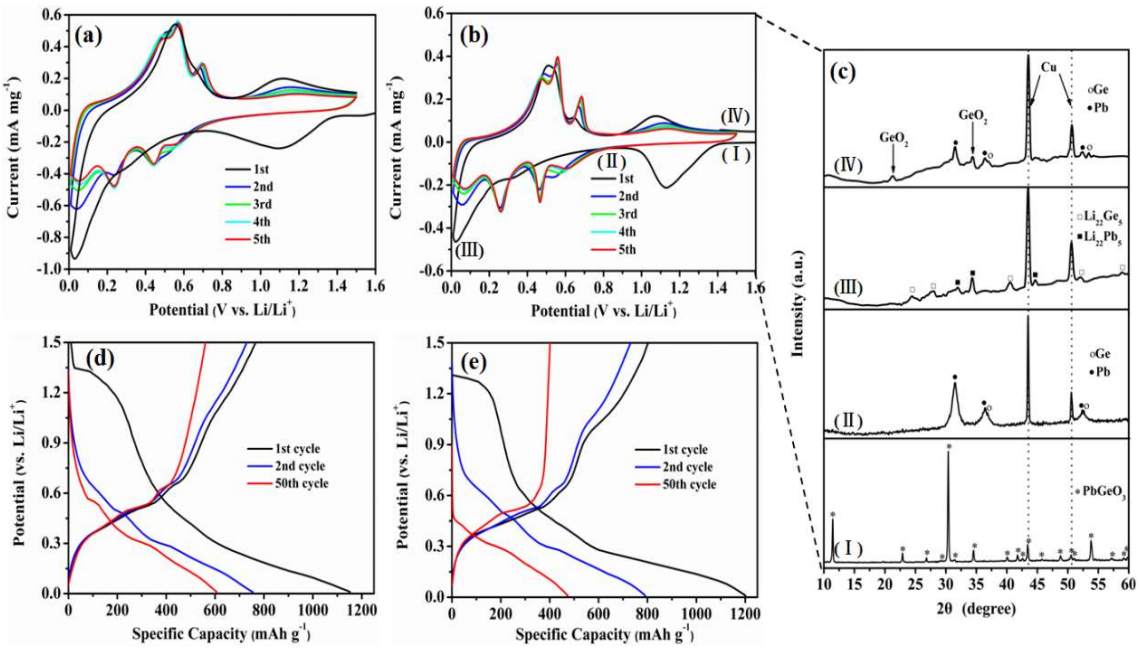

Figure 5.3 Cyclic voltammograms for the first 5 cycles of (a) the $PbGeO_3$-GNS2(20 wt.%) anode and (b) the pure $PbGeO_3$ anode; (c) ex-situ XRD patterns of the pure $PbGeO_3$ anode: (I) as-prepared, (II) first discharge to 1.0 V, (III) fully discharged to 0.01 V, and (IV) fully charged to 1.50 V; charge-discharge curves of (d) the $PbGeO_3$-GNS2 anode and (e) the pure $PbGeO_3$ anode for selected cycles.

Because the $PbGeO_3$ nanowires in the $PbGeO_3$ anode and $PbGeO_3$-GNS anodes are likely to be subject to the same Li storage mechanism, ex-situ XRD data on the $PbGeO_3$ anode were collected to identify it in detail, as shown in Figure 5.3(c). Based on these results and the discharge-charge mechanisms of metal germanate, Pb and, Ge[59, 163, 177, 181, 182, 197-202], the Li ion intercalation and de-intercalation reactions of $PbGeO_3$ anode are proposed as the following reaction Equations (5.1)-(5.4):

$$PbGeO_3 + 6Li^+ + 6e^- \rightarrow Pb + Ge + 3Li_2O \quad (5.1)$$

$$Pb + xLi^+ + xe^- \rightarrow Li_xPb\ (0 < x \leq 4.4) \quad (5.2)$$

$$Ge + yLi^+ + ye^- \rightarrow Li_yGe\ (0 < y \leq 4.4) \quad (5.3)$$

$$Ge + 2Li_2O \rightarrow GeO_2 + 4Li^+ + 4e^- \quad (5.4)$$

Remarkably, the first CV sweep is substantially different from the subsequent ones. Within the initial cathodic sweep, the broad peak between 1.4 and 1.0 V is related to the decomposition of $PbGeO_3$ into Pb, Ge, and Li_2O, accompanied by the formation of a SEI layer as well[58, 182]. During the following scans, the broad decomposition peak disappears, and other evident peaks can be traced to processes that are activated after the 1st cycle. Specifically, three anodic peaks are associated with the de-alloying reactions of Li-Ge at 0.47 V[6] and Li-Pb at 0.47, 0.56, and 0.68 V[197], respectively. Partial oxidation of Ge by the Li_2O amorphous matrix to GeO_2 occurs from 1.0 to 1.3 V, and GeO_2 is then reversibly converted to Ge within the voltage range from 0.8 to 0.6 V in the anodic sweep[198, 199]. It is well known, however, that Pb is relatively stable and cannot undergo a partially reversible reaction with Li_2O[200, 201]. The alloying reactions of Li-Ge and Li-Pb occur at 0.46 and 0.26 V, respectively, followed by their further alloying reactions below 0.2 V[163, 198, 202]. Pb and Ge diffraction peaks can be detected in the ex-situ XRD patterns after the first discharge to 1.0 V. When the anode is fully discharged to 0.01 V, the diffraction peaks of $Li_{22}Ge_5$ and $Li_{22}Pb_5$ are observed due to the alloying reactions. The peaks are indexed to the formation of Pb, Ge, and GeO_2 at the fully charged stage, and no PbO peak can be found, implying that Pb was not oxidized by Li_2O. These results are well consistent with the CV data discussed above.

Selected galvanostatic charge-discharge profiles of $PbGeO_3$-GNS2(20 wt.%) anode and the pure $PbGeO_3$ anode at the current density of 100 mA g^{-1} from 0.01 to 1.50 V are shown in Figure 5.3(d, e). As can be seen from these profiles, the voltage trends of the

pure $PbGeO_3$ anode and the $PbGeO_3$-GNS2 anode are in good agreement with their CV curves. The obvious irreversible capacity loss can be traced in both the pure $PbGeO_3$ anode and the $PbGeO_3$-GNS2 anode, which is mainly attributable to the reduction of $PbGeO_3$ to Pb, Ge, and Li_2O, together with the formation of a SEI layer[26]. After 50 cycles, the $PbGeO_3$-GNS2 anode possesses 92 % coulombic efficiency (607 mAh g^{-1} discharge capacity and 561 mAh g^{-1} charge capacity), much higher than 85% of those of the pure $PbGeO_3$ anode (474 mAh g^{-1} discharge capacity and 401 mAh g^{-1} charge capacity). Multiple clear plateaus in typical cycles still exist up to 50 cycles, suggesting that the composite anode could maintain good kinetic activity towards Li ion intercalation/de-intercalation during cycling, which is responsible for the improved coulombic efficiency.

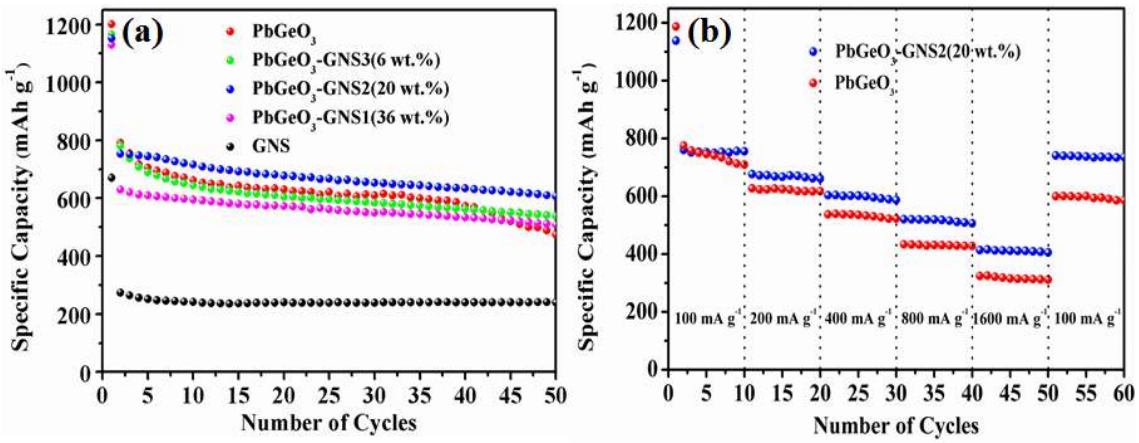

Figure 5.4 (a) Cycling stability of the pure $PbGeO_3$ and the $PbGeO_3$-GNS anodes, and (b) rate capability of the pure $PbGeO_3$ and the $PbGeO_3$-GNS2(20 wt.%) anode.

Figure 5.4(a) demonstrates the cycling stability of the $PbGeO_3$-GNS composite anodes at the current density of 100 mA g^{-1} from 0.01 to 1.50 V, and the results for pure $PbGeO_3$ anode and for GNS anode are also included for comparison. In the first cycle, the discharge capacity of the pure $PbGeO_3$ is about 1201 mAh g^{-1}, and it gradually drops to

474 mAh g^{-1} after 50 cycles, which is about 39% of the initial capacity. Remarkably, the $PbGeO_3$ nanowires, after being decorated on the GNS, show improved cyclic performance. To be specific, the discharge capacities of the $PbGeO_3$-GNS3(6 wt.%) anode and the $PbGeO_3$-GNS1(36 wt.%) anode are about 538 and 508 mAh g^{-1} after 50 cycles, respectively, still showing 45 % and 46 % capacity retention. The $PbGeO_3$-GNS2(20 wt.%) anode delivers a reversible capacity of 607 mAh g^{-1}, which is 53 % of its initial capacity and 28 % higher than that of the pure $PbGeO_3$ anode. The $PbGeO_3$-GNS1 and $PbGeO_3$-GNS3 anodes show lower discharge capacity after 50 cycles due to less $PbGeO_3$ active material and less GN conductive matrix loading, respectively. Therefore, the optimum $PbGeO_3$ content in the composite paper anode is 80 wt.%. Similar synergic effects were also observed in other composite anode systems[173, 203].

The current density was also varied to investigate the rate capability of the anodes made from the pure $PbGeO_3$ and $PbGeO_3$-GNS2(20 wt.%) composite in Figure 5.4(b). The $PbGeO_3$-GNS2 anode shows larger capacity at each individual current density and 406 mAh g^{-1} at a current density of 1600 mA g^{-1}. After cycling at high current densities, the $PbGeO_3$ and the composite anode were galvanostatically discharged and charged at a current of 100 mA g^{-1} again. Unlike the discharge capacity of the $PbGeO_3$ anode, the discharge capacity of the composite anode recovers to 736 mAh g^{-1}, almost the same as its initial reversible capacity.

The improvements in the electrochemical performance of the $PbGeO_3$-GNS anodes over the pure $PbGeO_3$ anode materials can be ascribed to the uniform encapsulation of the $PbGeO_3$ nanowires in the composite anode in the electrochemically active GNS and the good contact that they maintain with each other. These structural characteristics could

enable more efficient Li diffusion channels for the Li insertion and de-insertion. Moreover, the GNS could increase the electrical conductivity of the anodes by forming a three-dimensional electrically conductive network. Furthermore, the GNS could provide enough void spaces to limit the Ge particle volume changes and agglomeration, maintaining the structural integrity of the composite anode during the charge-discharge processes.

Electrochemical impedance spectroscopy (EIS) results for the pure $PbGeO_3$ anode and the $PbGeO_3$-GNS2(20 wt.%) anode were collected using a sine wave of 10 mV amplitude over a frequency range of 100 kHz-0.01 Hz, as shown in Figure 5.5. To maintain uniformity, the impedance measurements were performed in the fully charged state after running charge-discharge for 50 cycles. The equivalent circuit obtained from the four fitting modes for the Nyquist plots are shown in the inset. All plots exhibit one compressed semicircle in the high frequency region and a sloping line in the low frequency regime. The intercept on the Z_{real} axis in the high frequency region reveals the entire resistance of the electrolyte, separator, and electrical contacts. The semicircle in the high frequency range indicates the charge transfer resistance (R_{ct}), which is related to the charge transfer reaction at the electrode/electrolyte interface. The inclined line in the low frequency region represents the Warburg impedance (Z_W), determined by the ion diffusion process in the anode material[204, 205].

It should be noted that considerable differences can be observed on comparing the EIS data for the $PbGeO_3$-GNS2(20 wt.%) anode to the data for the pure $PbGeO_3$ anode. On the one hand, the R_{ct} values for the $PbGeO_3$-GNS2 anode before cycling and after 50 cycles are both lower than those of the $PbGeO_3$ anode, respectively. It can be assumed

that the GNS in the composite could serve as a highly electrically conductive matrix and enable efficient charge transport at the electrode/electrolyte interface, resulting in suppression of the interparticle resistance of the anode by incorporating the GNS in a composite with $PbGeO_3$.

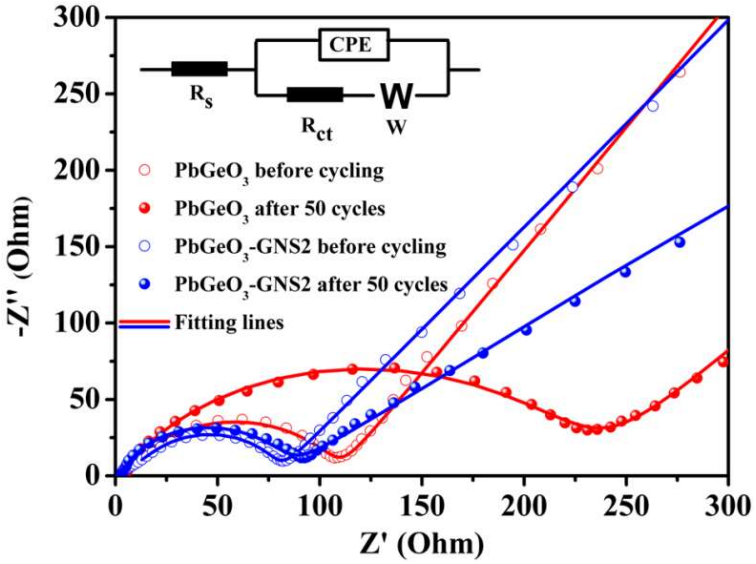

Figure 5.5 Impedance spectra for the pure $PbGeO_3$ anode and the $PbGeO_3$-GNS2(20 wt.%) anode before cycling and after 50 cycles, with the inset showing the equivalent circuit model.

On the other hand, the R_{ct} value after 50 cycles is increased by 130 % (from 109 to 251 Ω) for the pure $PbGeO_3$ anode, while there is only an increase of approximately 14 % (from 83 to 95 Ω) for $PbGeO_3$-GNS2 anode. Due to the alleviation of Ge volume changes and the particle agglomeration by the GNS in the composite anode during cycling, the electrode integration can be well maintained, which could significantly restrain the increase of R_{ct}.

To characterize the changes in the structure of the $PbGeO_3$-GNS2 composite before and after cycling, a morphological study was conducted on the composite after 50 cycles, and the TEM image is shown in Figure 5.6(a). The cycled composite shows a similar morphology to the $PbGeO_3$-GNS2 composite before cycling [see Figure 5.2(e)], illustrating that the nanowire structure was retained after 50 cycles. The element distribution in the anode was analysed by EDS over the rectangular region in Figure 5.6(b).

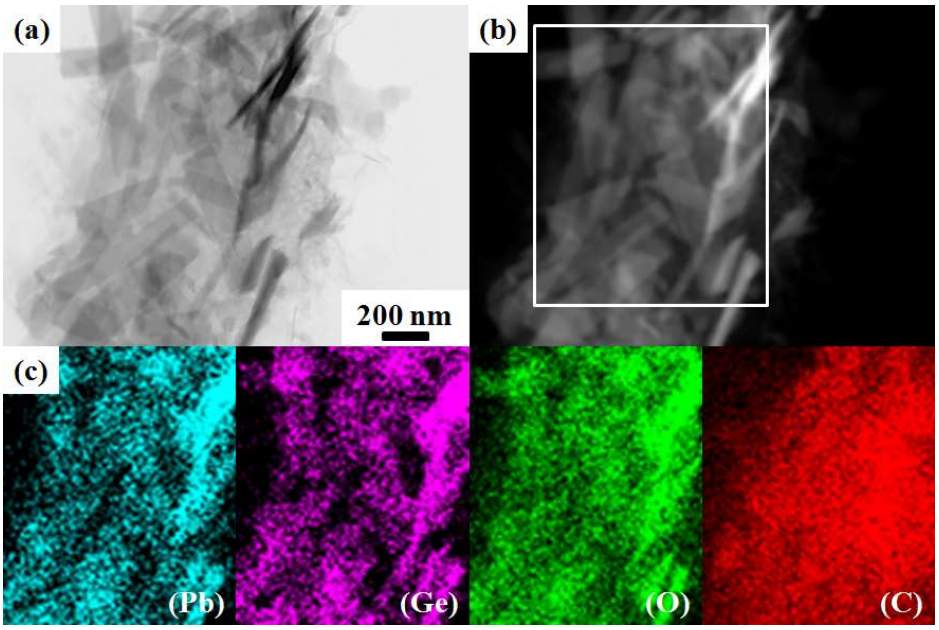

Figure 5.6 (a) TEM, (b) STEM, and (c) corresponding element mapping images of the $PbGeO_3$-GNS2(20 wt.%) anode after 50 cycles.

The obtained distributions of different elements are shown in Figure 5.6(c). The EDS mapping indicates that Pb, Ge, and O are uniformly distributed on the nanowires, and the structural stability of the $PbGeO_3$-GNS2 anode was further confirmed. It was reported previously that germanate nanowire anode could ensure fast Li-ion insertion/removal during cycling, offering excellent electrochemical performance[58, 59]. Additionally, the 1-D nanowires are robust enough to maintain the initial morphology, minimizing the strain

of the Ge volume change. More importantly, the conductive GNS matrix not only acts as an elastic buffer spacer to further accommodate the Ge volume change, but also prevents the nanowires from agglomerating and restacking during the Li-ion insertion/extraction processes, which is favourable for improving the electrochemical performance of the anode material.

5.4 Conclusions

In conclusion, novel $PbGeO_3$-GNS composites have been synthesised by a simple and effective in situ hydrothermal method, in which $PbGeO_3$ nanowires with diameters in the range of 100-200 nm are embedded in conductive and interconnected GN networks. The charge-discharge mechanism during cycling is recognized to originate from the decomposition of $PbGeO_3$ into Pb, Ge, and Li_2O, leading to reversible lithiation and de-lithiation for Pb and Ge, accompanied by a partial Ge oxidation reaction by Li_2O. The $PbGeO_3$-GNS anodes exhibit superior cycling performance compared to the pure $PbGeO_3$ anode, delivering enhanced discharge capacities after 50 cycles and displaying obviously improved rate capability. The improvements can be attributed to the GNS matrix in the composites, which increases the electrical conductivity of the composite anodes, maintains the structural integrity of the composite anodes by alleviating volume changes and particle agglomeration, and provides more efficient paths for Li diffusion in the composite anodes, so as to enhance electrochemical activities towards Li insertion and de-insertion during cycling.

CHAPTER 6 A MICROWAVE AUTOCLAVE SYNTHESIZED MANGANESE DIOXIDE/GRAPHENE NANOSHEET COMPOSITE AS A CATHODE MATERIAL FOR LITHIUM-OXYGEN BATTERIES

6.1 Preface

With the increasing concerns on environmental pollution and energy exhaustion, a great deal of effort has been devoted to exploring green energy and high efficiency energy sources as alternatives to fossil fuels. Recently, the rechargeable LOBs, utilizing an unlimited supply of oxygen from the air, have attracted extensive attention[206-208]. Based on the reversible reduction of O_2 on a cathode host to form Li_2O_2, the LOBs deliver high theoretical energy density and power density, which are larger than those of the conventional Li batteries and almost equal to those of gasoline[128, 209, 210]. Based on these facts, they could potentially be the most promising power source system for large-scale energy storage and electric vehicles.

To achieve outstanding electrochemical performance from the LOBs, the critical factor is to employ an efficient catalyst cathode material. Manganese oxides have been intensively examined because they are regarded as offering a favorable trade-off among electrocatalytic activity, cost, easy preparation, and environmental friendliness[211, 212]. Among these, MnO_2 catalyst exhibits excellent round-trip efficiency, specific capacity, cycling stability, making it a suitable cathode candidate to satisfy the requirements for LOBs[111, 213, 214]. MnO_2 typically exhibits low electronic conductivity, however, which definitely limits its electrochemical

performance. Therefore, hybridization of the MnO_2 with conductive substrate materials is commonly needed to solve this problem.

GNS, in the form of a few layers of carbon atoms bonded in a hexagonal lattice, feature excellent electrical conductivity, large theoretical specific surface area, and good chemical stability[215, 216]. Such advantages suggest their suitability for wide employment in energy-storage applications, including supercapacitors, LIBs, fuel cells, etc.[217-219]. Notably, GNS have also been applied in LOBs, and the data demonstrate that they could serve as a matrix material for the catalyst cathode[87, 220, 221]. The MnO_2/GNS composite is thus expected to provide favorable electrocatalytic performance for LOBs.

In this work, the MnO_2/GNS composite was prepared in situ via an eco-friendly and fast microwave autoclave route. FE-SEM and TEM observations show that the thin MnO_2 nanoflakes are uniformly distributed on the three-dimensional (3D) GNS architecture. Electrocatalytic measurements were conducted on LOBs with MnO_2/GNS cathode, and the results demonstrate that this MnO_2/GNS composite cathode delivers notably superior electrocatalytic performance in comparison to that of its pure GNS cathode counterpart, with higher capacity, lower overpotential, and better cycling stability. These improvements can be ascribed to the synergetic effects of the MnO_2 nanoflakes and the GNS in the composite. The GNS matrix forms a highly electrically conductive network, which could increase the electrical conductivity of the composite, provide enough space for the tri-phase (solid-liquid-gas) reaction, and act as a volume change buffer during cycling. The well dispersed MnO_2

nanoflakes on the GNS matrix could make full use of their high catalytic activity and facilitate more efficient O_2/Li_2O_2 conversion on the surfaces of the composite.

6.2 Experimental

6.2.1 Preparation of the MnO_2/GNS Composite

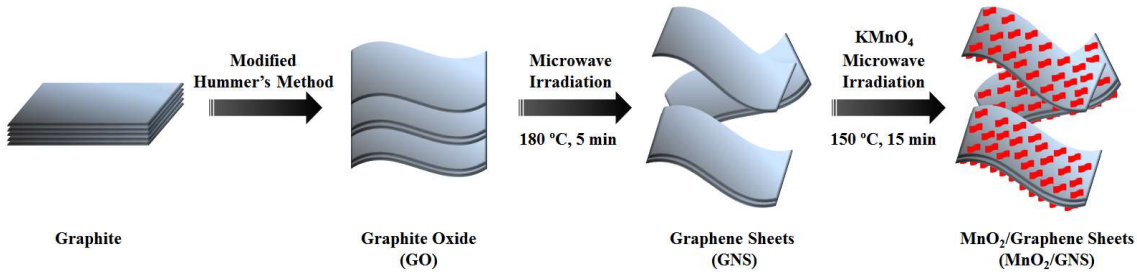

Figure 6.1 Schematic illustration of the preparation process for the MnO_2/GNS composite.

The synthetic procedure for the MnO_2/GNS composite is shown in Figure 6.1. GO was fabricated according to a modified Hummers method[192] from natural graphite powder (Fluka). To prepare the GNS, a microwave autoclave method was applied at 180 ºC for 5 min[187]. Subsequently, 40 mg as-prepared GNS were added to 160 mL deionized water, followed by 1 h ultrasonication to make a homogeneous suspension. The suspension was mixed with 240 mg $KMnO_4$ under continuous stirring, which was continued for 30 min. The suspension was divided into 8 sealed Teflon vessels (20 mL each) and reacted at 150 ºC for 15 min in a Milestone Microsynth Microwave Labstation. The precipitates were collected and washed with distilled water and ethanol. The MnO_2/GNS composite was obtained after drying in a vacuum oven at 80 ºC overnight.

6.2.2 Physical Characterization

XRD patterns were performed on a GBC MMA generator and diffractometer with Cu Kα radiation. Raman spectroscopy was conducted on a JOBIN YVON HR800 Confocal system with 632.8 nm diode laser excitation using a 300 lines mm^{-1} grating. TGA was carried out using a SETARAM Thermogravimetric Analyzer (France). FE-SEM images were collected with a JEOL 7500 microscope, and transmission electron microscope (TEM) images were obtained with a JEOL JEM 2010 microscope.

6.2.3 Electrochemical Measurements

To prepare the cathodes for LOB testing, 90% catalyst and 10% PTFE were added into isopropanol to make a slurry. The slurry was pasted onto a carbon paper and dried at 120 ºC overnight in a vacuum oven. The cathodes were sealed in the CR 2032 coin-type cells with holes in the positive top covers in an Ar-filled Mbraun glove box (Germany). Li foil as the counter electrode was separated from the cathode as the working electrode by a glassy fiber separator. 1 M $LiCF_3SO_3$ in TEGDME was used as the electrolyte. Cyclic voltammetry (CV) was conducted on a Biologic VMP-3 electrochemistry workstation. The Li-O_2 cells were galvanostatically discharged and charged via a LAND CT 2001A multi-channel battery tester in an O_2-saturated box with activated molecular sieves. The specific capacities were determined according to the amount of catalyst in the cathode.

6.3 Results and Discussion

XRD patterns for the graphite, the GO, the GNS, and the MnO_2/GNS composite are presented in Figure 6.2(a). The sharp diffraction peak at 26.4º for graphite cannot be

found in the graphite oxide pattern, although a broad peak appears at around 11.0°[38], implying the successful oxidation of the commercial graphite to GO. As for the GNS diffraction pattern, the peaks located at around 24.5° and 43.1° are related to the graphite-like (002) and (100) structures, respectively[187]. All the peaks in the XRD pattern of the MnO_2/GNS composite are consistent with those of the monoclinic birnessite phase (JCPDS 42-1317), indicating the formation of δ-MnO_2 in the composite [222, 223].

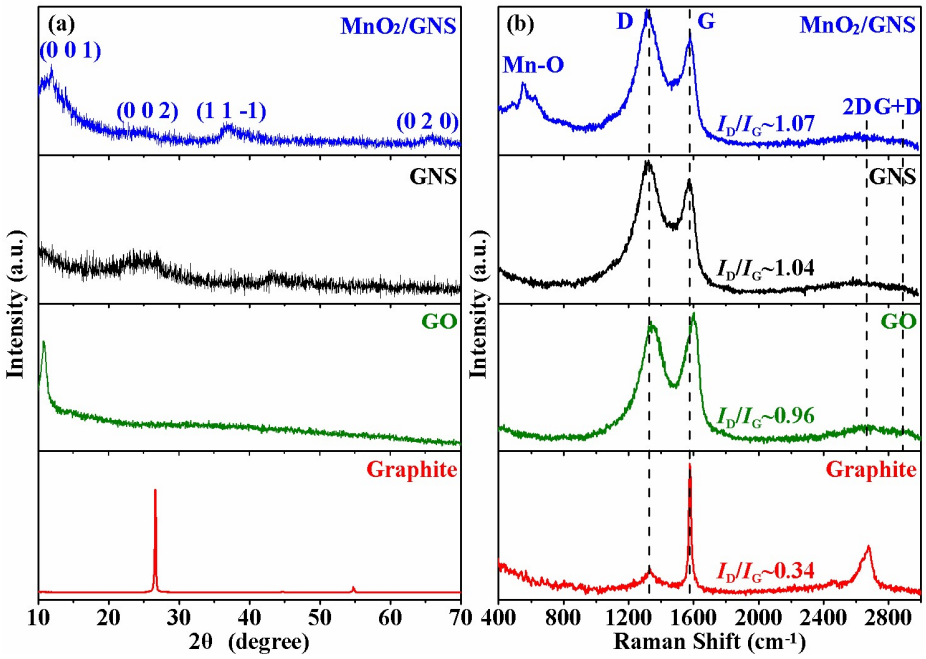

Figure 6.2 (a) XRD patterns and (b) Raman spectra of the graphite, the GO, the GNS, and the MnO_2/GNS composite.

Raman spectroscopy was further conducted to investigate the components of the different samples in Figure 6.2(b). All the Raman spectra of the graphite, the GO, and the GNS displayed two prominent peaks, which are assigned to the D and G bands. The D band is identified as due to the defects and disorder in the graphitized structure, while the G band is associated with the in-plane stretching vibration of sp^2-bonded carbon atoms[224, 225]. The intensity ratio of the D band to the G band (I_D/I_G) can be used to index the degree of

disorder of carbon materials[226]. It is clear that the D band and G band peaks of the graphite are located at 1352 and 1576 cm^{-1}, respectively. The D band peak of the GO becomes more prominent and broader, compared with that of the graphite, which is due to the reduction in size of the in-plane sp^2 domains and the increase in structural distortion[227]. Moreover, the G band peak of GO is blue shifted to 1592 cm^{-1}, because of the presence of isolated double bonds with a higher resonance frequency after chemical oxidation[228]. Evidently, the G band and D band peaks are located at around 1354 and 1580 cm^{-1} for GNS, and its ID/IG is ~1.04, higher than those of graphite (~0.34) and GO (~0.96), which demonstrates a decrease in the size of the in-plane sp^2 domains and the partially ordered crystal structure of the GNS[229]. In addition, feeble and broad peaks could be found in the GO, GNS, and MnO_2/GNS composite samples in the range of 2600-3000 cm^{-1}, corresponding to the combination of 2D and G+D bands, which matches well with the reported results for GO and GNS prepared by the microwave-assisted method [230, 231]. In the results for the MnO_2/GNS composite, the structural characteristics of the GNS are retained, although this sample has a higher ID/IG value of 1.07, and the Mn-O vibration modes of manganese oxide can also be observed in the range of 400-700 cm^{-1}[222, 223]. This demonstrates that the MnO_2/GNS composite was successfully synthesized by the method described above.

Surface element analysis was carried out on the MnO_2/GNS composite using XPS. The XPS survey spectrum in Figure 3(a) displays signals related to the elements Mn, O, K, and C, implying that the MnO_2/GNS composite had been successfully prepared. The high-resolution Mn 2p spectrum in Figure 3(c) exhibits two peaks with binding energies of 641.7 eV (Mn $2p_{3/2}$) and 653.3 eV (Mn $2p_{1/2}$), with a spin energy separation of 11.6 eV, which is consistent with the reported results for MnO_2 [232, 233]. The high-resolution K 2p

spectrum in Figure 3(b) displays two peaks centered at 292.6 eV (K $2p_{3/2}$) and 295.5 eV (K $2p_{3/2}$), suggesting the formation of K-birnessite MnO_2[234]. These results further confirm the presence of δ-MnO_2 in the composite.

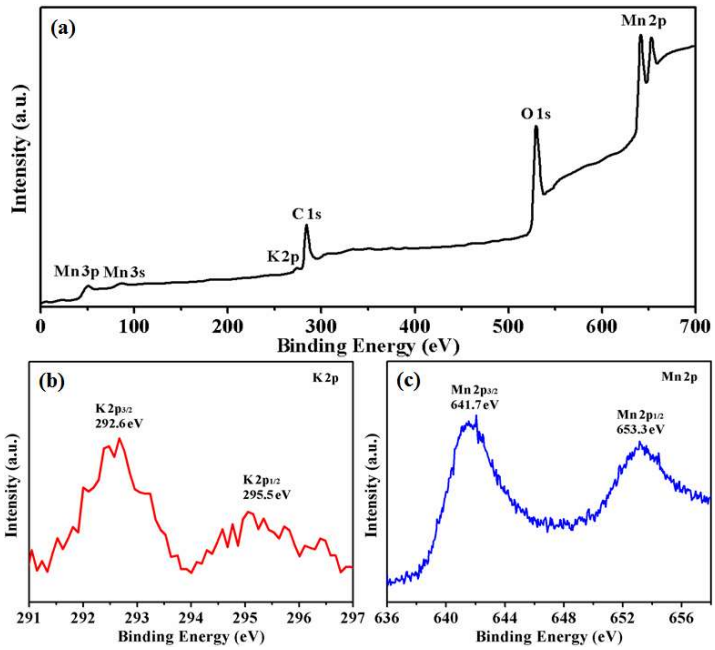

Figure 6.3 (a) XPS survey spectrum of the MnO_2/GNS composite; high-resolution (b) K 2p and (c) Mn 2p XPS spectra of the MnO_2/GNS composite.

The weight percentage of the MnO_2 in the MnO_2/GNS composite was obtained by TGA from 25 to 800 ℃ with a heating rate of 10 ºC min^{-1} in air. Figure 6.4 presents the weight

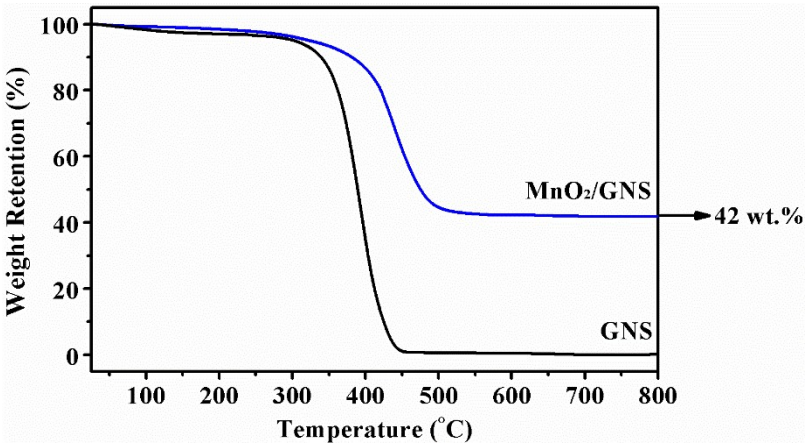

Figure 6.4 TGA curves of the GNS and the MnO_2/GNS composite.

loss of the MnO_2/GNS composite along with that of the GNS. It is worth noting that MnO_2 is reported to remain stable during the heating process[235, 236], while the GNS in the composite sample was all burned out. Therefore, the weight loss of the composite is entirely from the oxidation of the GNS, and the weight retention of 42 wt.% corresponds to the weight percentage of the MnO_2 in the composite.

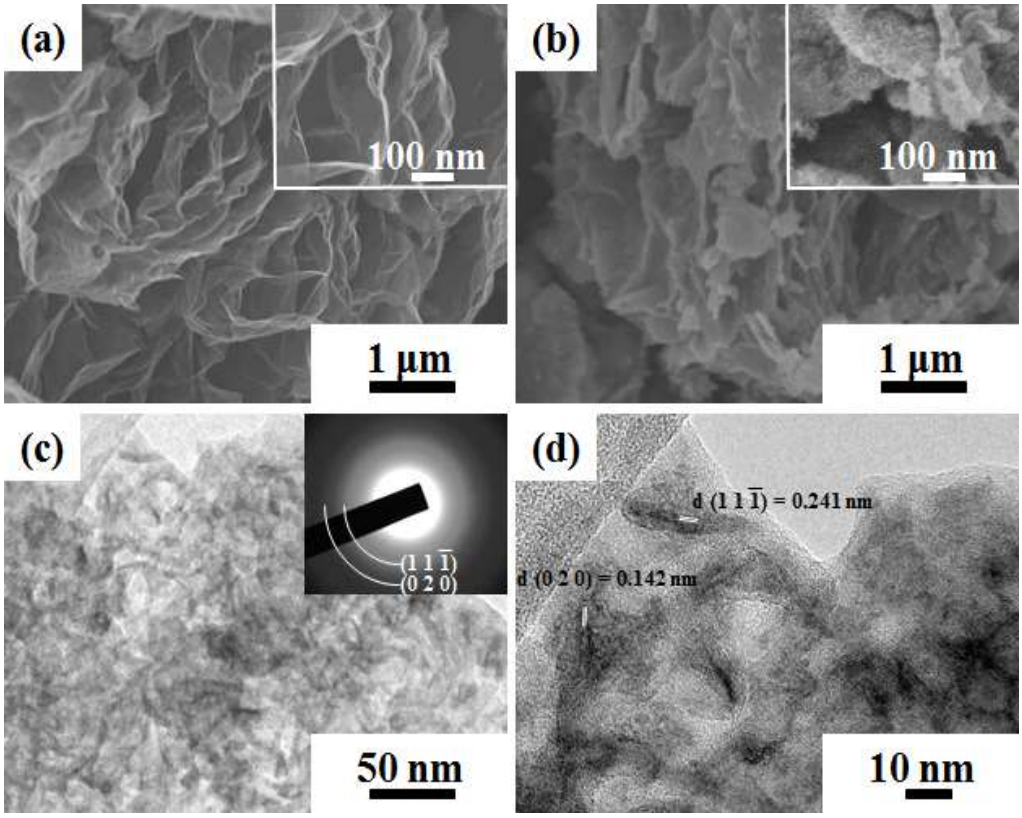

Figure 6.5 FE-SEM images of (a) the GNS and (b) the MnO_2/GNS composite, with an enlarged area in the inset; (c) TEM image of the MnO_2/GNS composite, with associated SAED pattern in the inset; (d) high resolution TEM of the MnO_2/GNS composite.

FE-SEM was carried out to characterize the morphology of the GNS and MnO_2/GNS composite. In Figure 6.5(a), the GNS appears to have the morphology of a thin and wrinkled structure, forming a three-dimensional layered framework. In Figure 6.5(b), the MnO_2/GNS composite displays a sandwich-like structure, in which the MnO_2 nanoflakes are homogeneously distributed on or between the GNS, as evidenced by the inset of

Figure 6.5(b). The TEM image of the MnO_2/GNS composite in Figure 6.5(c) shows that the size of the MnO_2 nanoflakes is in the range of 20-25 nm. The indexed diffraction rings in the selected area electron diffraction pattern (SAED) in the inset of Figure 6.5(c) are related to the structural characteristics of MnO_2 with $(11\bar{1})$ and (020) planes. The high-resolution TEM image in Figure 6.5(d) reveals the lattice fringes of typical MnO_2 nanoflakes, with lattice spacing of 0.241 and 0.142 nm, corresponding to the spacing of the $(11\bar{1})$ and (020) planes, respectively. These results agree well with the XRD results and confirm the formation of MnO_2 nanoflakes in the composite.

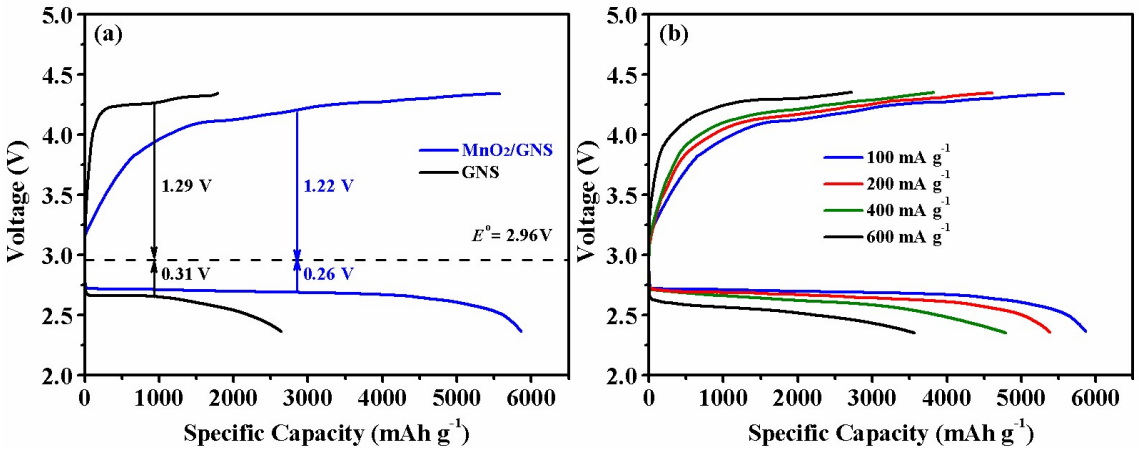

Figure 6.6 Comparison of the initial discharge/charge curves of the Li-O_2 cells from 2.35 to 4.35 V for (a) the GNS and the MnO_2/GNS composite cathodes at 100 mA g^{-1}, and (b) the MnO_2/GNS composite cathode at different current densities.

The electrocatalytic performance of the GNS, and the MnO_2/GNS composite cathodes was investigated in Li-O_2 cells, and the results are presented in Figure 6.6. Figure 6.6(a) shows the initial galvanostatic discharge/charge curves at a current density of 100 mA g^{-1} within a voltage window of 2.35 to 4.35 V vs. Li^+/Li. The discharge and charge capacities of the GNS cathode are 2644 and 1791 mAh g^{-1}, with the overpotentials of 0.31 and 1.29 V, respectively, compared with the thermodynamic potential of Li_2O_2 (E^0 = 2.96 V). Its round-trip efficiency (the ratio of the discharge voltage of 2.65 V to the charge voltage of 4.25 V) is calculated to be 62 %. After coating MnO_2 on the GNS architecture,

the MnO_2/GNS composite cathode delivers improved discharge/charge capacities and round-trip performance. To be specific, the initial discharge and charge capacities of the MnO_2/GNS cathode are 5862 and 5572 mAh g^{-1}, with 3218 and 3781 mAh g^{-1} representing increased performance over that of the GNS cathode, respectively. It should also be noted that the discharge and charge overpotentials drop to 1.22 and 0.26 V, resulting in a round-trip efficiency of 65 %. In Figure 6.6(b), the current density was varied to 200, 400, and 600 mA g^{-1} to evaluate the rate performance of the MnO_2/GNS composite cathode. It can be found that with increasing current density, the MnO_2/GNS composite cathode exhibits favorable discharge/charge capacities of 5385/4611, 4794/3826, and 3566/2720 mAh g^{-1}, respectively.

The improved specific capacity, round-trip efficiency, and high rate performance are owing to the unique design of the MnO_2/GNS composite as the cathode catalyst material. It is believed that highly conductive GNS could promote easy electron transfer in the composite, while keeping the GNS matrix and MnO_2 nanoflakes in good contact, and improving the electrochemical kinetics in the batteries. Furthermore, 3D-structured GNS acts as an ideal support to enable sufficient O_2 and electrolyte transport throughout the whole electrode, ensuring enough tri-phase sites to allow the catalytic reactions and providing adequate space to accommodate the discharge products. More importantly, the MnO_2 nanoflakes on the GNS could offer excellent catalytic activity, efficiently promoting the deposition and decomposition of discharge and charge products. Therefore, it is concluded that the synergistic effects from the combination of the MnO_2 nanoflakes and the GNS network account for the superior ORR and OER performances of the composite cathode for the LOBs.

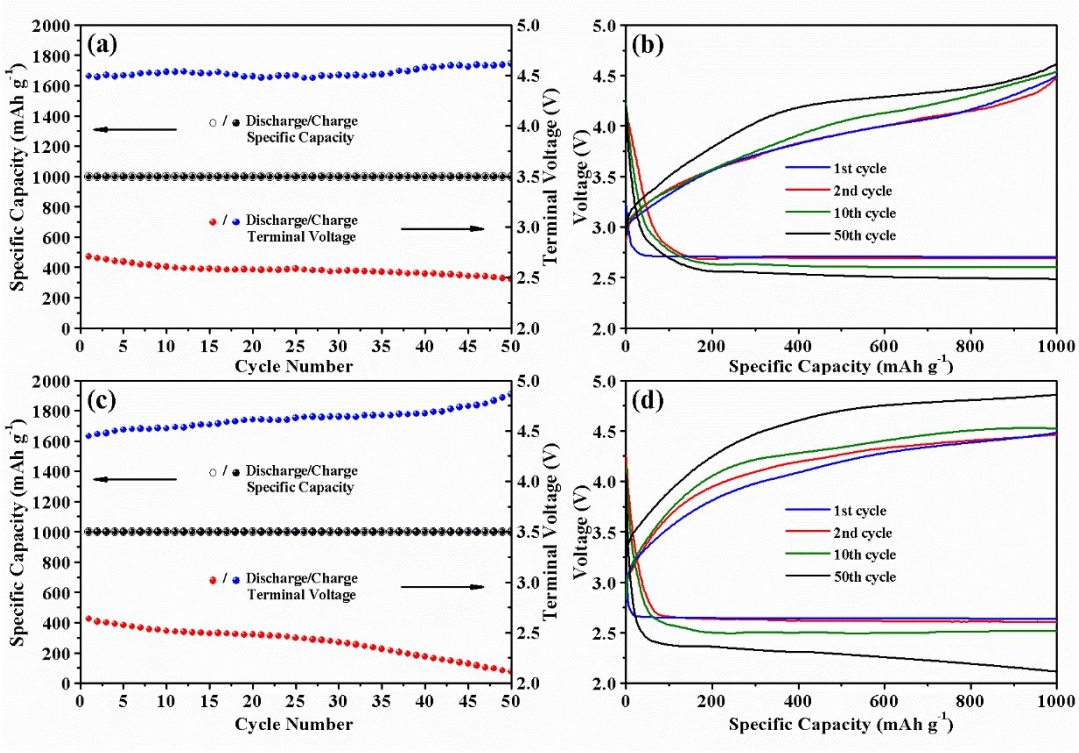

Figure 6.7 Cycling performances (a, c), and the corresponding typical discharge/charge curves (b, d) of the Li-O_2 cells for selected cycles, with (a, b) the MnO_2/GNS composite and (c, d) the GNS cathodes under a capacity limit of 1000 mAh g^{-1} at 100 mA g^{-1}.

Figure 6.7 presents the cycling stability curves of the GNS and MnO_2/GNS cathodes at a current density of 100 mA g^{-1} with a fixed specific capacity of 1000 mAh g^{-1}. In Figure 6.7(a), it is demonstrated that the GNS cathode could be discharged-charged for 50 cycles with a capacity of 1000 mAh g^{-1}. The discharge and charge terminal voltages rise to 2.12 and 4.86 V, respectively, which represent a 22.7 % decrease and a 6.8 % increase of the initial discharge/charge terminal voltages (2.7 and 4.45 V), respectively. Selected discharge/charge profiles are also included in Figure 6.7(b) to portray the differences in detail. In contrast, the discharge/charge terminal voltages of the MnO_2/GNS composite cathode remain almost stable over 50 cycles in Figure 6.7(c), and limited overpotentials can be found in the selected discharge/charge profiles in Figure 6.7(d). These results indicate that the MnO_2/GNS composite cathode presents superior reversible catalytic

activity compared with the GNS cathode. This is because the discharge products can easily form and decompose on the surfaces of the composite cathode, as a result of the substantial MnO_2 catalytic sites for the O_2/Li_2O_2 conversion reactions. In addition, the carbon surfaces are fully covered by the MnO_2 nanoflakes, effectively preventing the formation of irreversible discharge by-products and the decomposition of the electrolyte. In addition, the composite cathode could maintain its structural integrity during cycling. This is because the 3D layered GNS skeleton could reduce the cathode volume expansion caused by the accumulation of the discharge products, and the intimate contact between the GNS and the MnO_2 nanoflakes formed in situ contributes to inhibiting the cathode cracking in the discharge-charge progress. Table 6.1 summarizes the Li-O_2 battery performance of some representative cathodes containing MnO_2 and other metal oxides reported in the literature. It is clearly revealed that the MnO_2/GNS composite cathode outperforms those other metal-based electrocatalysts under similar testing conditions, especially in terms of capacity and cycling stability, making MnO_2/GNS composite a promising material to serve as the cathode catalyst in Li-O_2 batteries.

Table 6.1 Comparison of the Li-O_2 battery performance of MnO_2/GNS cathode with those of some representative metal oxides reported in the literature.

Materials	**Current Density**	**Discharge Capacity[a]**	**Round-Trip Efficiency**	**Cycling Stability**	**Ref.**
MnO_2/GNS	100 mA g^{-1}	5862 mAh g^{-1}	~65%	Stable after 50 cycles	This work
MnO_2/Porous Carbon	100 mA g^{-1}	1400 mAh g^{-1}	~63%	Stable after 55 cycles	[237]
MnO_2/N-Graphite Nanofibers	0.1 mA cm^{-1}	4706 mAh g^{-1}	~63%	Stable after 50 cycles	[238]

MnO_2/MWCNT	32 mA g^{-1}	796 mAh g^{-1}	~63%	-	[236]
Co_3O_4/Carbon Paper	100 mA g^{-1}	2159 mAh g^{-1}	~61%	Stable after 48 cycles	[239]
CoO/Carbon Nanofibers	0.2 mA cm^{-1}	3884 mAh g^{-1}	~67%	Stable after 25 cycles	[240]
RuO_2 Hollow Spheres	100 mA g^{-1}	1380 mAh g^{-1}	~81%	Stable after 50 cycles	[241]
TiO_2 Nanofibers	200 mA g^{-1}	1467 mAh g^{-1}	~65%	Stable after 27 cycles	[242]
Fe_3O_4 Nanoparticles	70 mA g^{-1}	1200 mAh g^{-1}	~61%	Stable after 10 cycles	[112]
CuO Nanoparticles	70 mA g^{-1}	900 mAh g^{-1}	~60%	Stable after 10 cycles	[112]
NiO/Acetylene Black	100 mA g^{-1}	1260 mAh g^{-1}	~67%	Stable after 35 cycles	[243]

[a]The discharge capacities were calculated based on the amount of catalyst in the cathodes.

Ex-situ XRD and FE-SEM were conducted to trace the variations in the composition and morphology of the MnO_2/GNS composite cathode. In Figure 6.8(a), Li_2O_2 characteristic peaks can be detected after the 1st cycle full discharge to 2.35 V, indicating that the solid precipitates coated on the composite cathode in Figure 6.8(b) are Li_2O_2 and that they are definitely the main discharge product. After the composite cathode was fully charged to 4.35 V in the 1st cycle, the Li_2O_2 diffraction peaks vanished, and the composite structure was regained, as shown in Figure 6.8(c). These results demonstrate that no side products exist in the 1st cycle after recharge of the composite cathode, implying that there is no severe electrolyte decomposition during the full discharge/charge processes. Only MnO_2 peaks can be found in Figure 6.8(d) in the XRD pattern of the composite cathode after the 50th fixed-capacity charging process, and its 3D framework is also maintained, which is due to the fact that the MnO_2/GNS catalyst with high catalytic activity could promote more efficient O_2/Li_2O_2 conversion on the surfaces of the composite.

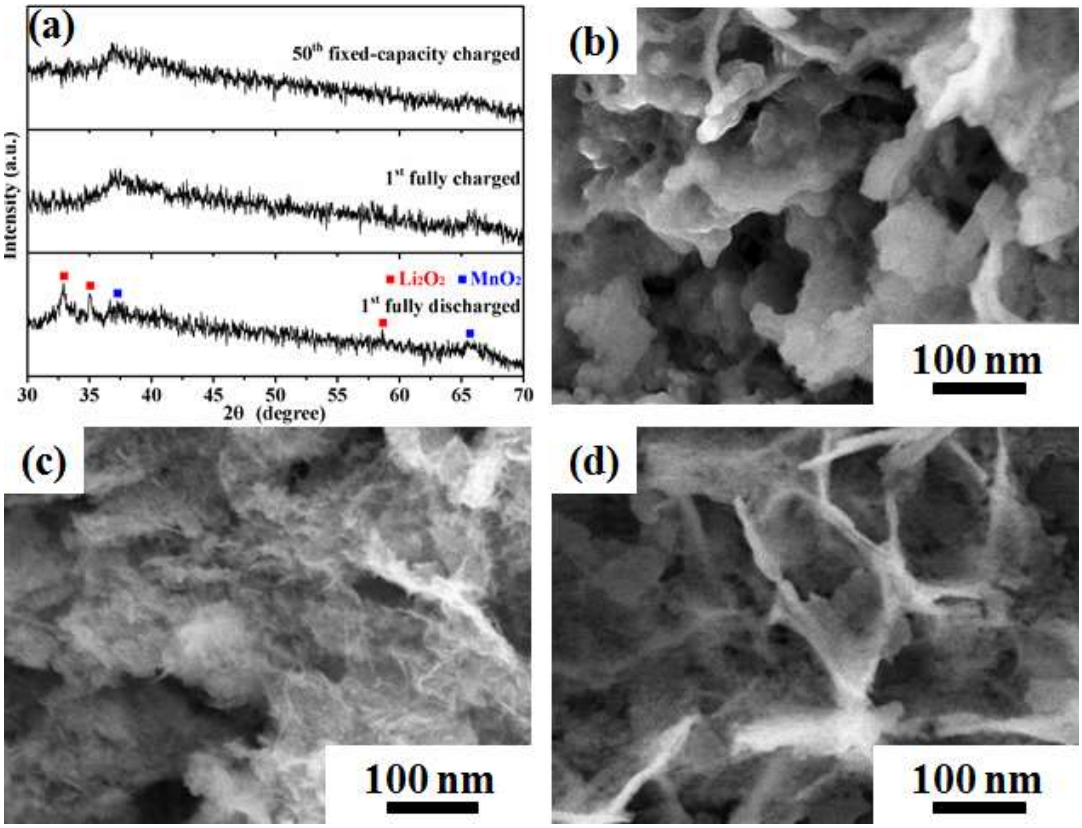

Figure 6.8 (a) XRD patterns at different discharge/charge stages; FE-SEM images of the MnO_2/GNS composite cathode at (b) the 1st cycle, fully discharged (to 2.35 V), (c) the 1st cycle, fully charged (to 4.35 V), and (d) the 50th cycle, after fixed-capacity charged.

6.4 Conclusions

In conclusion, GNS and MnO_2/GNS composite have been prepared via a fast and effective microwave autoclave method, with the MnO_2 nanoflakes grown in situ on the surfaces of the 3D GNS skeleton in the composite. Superior specific capacities, rate performance, and cycling stability can be achieved from the MnO_2/GNS composite cathode. It delivers discharge/charge capacities of 5862/5572 mAh g^{-1}, respectively, with the round-trip efficiency of 64 % at a current density of 100 mA g^{-1} within the voltage

window of 2.35 to 4.35 V. Even at a current density of 600 mA g^{-1}, it exhibits favorable discharge/charge capacities of 3566/2720 mAh g^{-1}, respectively. The cycling stability test results demonstrate that the Li-O_2 cell containing this composite cathode can be continuously discharged and charged without obvious terminal voltage variation at a current density of 100 mA g^{-1}, with a fixed capacity of 1000 mAh g^{-1} within 50 cycles. The combination of the high catalytic activity of MnO_2 nanoflakes with 3D structured GNS delivered superior ORR and OER catalytic performances, due to their excellent conductivity and adequate space to facilitate the catalytic reactions. Therefore, the MnO_2/GNS composite is a promising candidate for use as a cathode catalyst material for LOBs.

CHAPTER 7 A 3D POROUS NITROGEN-DOPED CARBON-NANOFIBER-SUPPORTED PALLADIUM COMPOSITE AS A CATHODE MATERIAL FOR LITHIUM-OXYGEN BATTERIES

7.1 Preface

Since the rechargeable LOBs were first introduced[73], they have triggered worldwide interest as a potential power system for future electric vehicles (EVs) due to their extraordinarily high theoretical energy density and power density, compared with those of conventional LIBs[209, 244, 245]. The LOBs, however, are actually in their developmental infancy now, and their electrochemical performance is constrained by several serious issues that have to be addressed before consideration of practical applications, including low round-trip efficiency (high charge/discharge overpotential), low rate capability, and poor cycling stability[210, 246, 247]. Instability of the electrolyte is likely to be responsible for the poor performance, due to the severe decomposition of the carbonate or linear-chain ether electrolyte, especially under a high voltage[248, 249]. Recently, TEGDME has been widely employed as electrolyte because it can deliver comparatively high stability towards oxygen radicals, inhibiting the side reactions in the discharge/charge processes[250-252].

Even if the pursuit of an ideal stable electrolyte has been achieved, a well-designed architecture for a high performance LOB cathode is still urgently demanded. Typically, a conductive structure with high surface area is essential for a cathode material, so as to facilitate both electron and oxygen transportation. Nanostructured carbon materials have been widely used as catalyst supports, because they tend to increase the electroactive

surface area and the electrical conductivity of the cathode catalyst[253-255]. In addition, an active catalyst material is also necessary because of the sluggish kinetics of the ORR and the OER in the cathode, which is closely related to the poor electrochemical performance of the LOBs[11, 256]. Tremendous efforts have been made to explore a wide range of various catalyst materials with high electrocatalytic activity, such as transition metal oxides[111, 115], perovskites[121, 257], metal nitrides[258, 259] bimetallic nanoparticles[107, 260], and precious metals[261, 262]. It should be noted that palladium (Pd) nanoparticles can promote both the ORR and the OER as a bifunctional catalyst and thus demonstrate exceptional round-trip efficiency, specific capacity, cycling stability, etc.[103, 263, 264], making Pd a promising material to serve as the cathode catalyst in LOBs. Therefore, hybridizations of Pd nanoparticles with nanostructured carbons were expected to introduce excellent electrocatalytic performance.

It was reported by Lei et al.[265] that fine Pd nanoparticles could be deposited on carbon nanoparticle supports via an atomic layer deposition process. Although a uniform Pd dispersion on the carbon substrate could be achieved, the electrochemical behavior demonstrates that the composite catalyst cathode has relatively low specific capacity with high ORR and OER overpotentials. To achieve better electrochemical properties, a general strategy is to construct a cross-linked three-dimensional (3D) structure for the electrode material[95, 266]. This is because the 3D carbon skeleton could not only offer continuous pathways for electron transport, which increases the electrical conductivity of the electrode, but also keep the matrix and the second phase particles in good contact, which aids in enabling more efficient charge transfer and improving the electrochemical kinetics in the batteries[31, 267]. Alegre et al.[268] confirmed this conclusion by comparing a Pd decorated oxygen electrode containing a carbon nanofiber network matrix with that

containing a carbon particle matrix in a three-electrode cell. The electrocatalytic performance demonstrated that this composite electrode possessed favourable cycling stability for potential applications as a bifunctional oxygen catalyst. Apart from the cross-linked 3D structure, porous structure and nitrogen doping have been proved to be effective methods to further improve the electrocatalytic performance of the carbon materials. The porous structure of the carbon materials plays the important role in the uniform dispersion of the second phase particles on them, which prevents their agglomeration on the carbon support and increases the catalytic activity of the active sites[269, 270]. Porous carbon materials with high surface area will also promote electrolyte immersion of their surfaces, which could provide more effective tri-phase (solid-liquid-gas) regions for the electrochemical reactions[271, 272]. Nitrogen doping is also well known to induce beneficial changes in both the electronic and the structural properties of the carbon materials, which could significantly increase their electrical conductivity[273, 274]. It has also been demonstrated that nitrogen atoms on the carbon nanostructures are efficient sites for catalytic reactions, modifying the carbon materials with desirable catalytic activity[221, 275]. In addition, the presence of nitrogen on the carbon materials will also coordinate the second phase particles from the point of view of their dimensions and dispersion, which is beneficial for reaching their full potential as active catalyst sites[276, 277].

Based on these concepts, I designed a Pd/porous nitrogen-doped carbon-nanofiber (Pd/PNCNF) composite catalyst as a cathode material for LOBs. In this work, the novel catalyst cathodes were synthesized by depositing Pd nanoparticles onto the PNCNF skeleton, which was directly derived from KOH treated polypyrrole (PPy) nanofibers. By using this strategy, a unique structure was achieved, in which the 3D

PNCNF network was homogeneously anchored by ultrafine Pd particles. The capacity, reversibility, and rate performance of the cathode catalysts were investigated by electrocatalytic testing, and the results demonstrate that the dramatic improvements in the electrocatalytic performance are attributable to the synergistic effects between the PNCNFs and the Pd nanoparticles in the composite catalyst.

7.2 Experimental

7.2.1 Preparation of Pd/PNCNF Composites

Firstly, the PPy nanofibers were obtained via the polymerization reaction route. 720 mg CTAB was dissolved in 200 mL 1 M HCl solution by constant stirring, and the solution was cooled down to 0-5 ºC in an ice bath. 330 mg distilled pyrrole (Py) monomer was then added into the solution, and vigorous stirring continued for 0.5 h. Meanwhile, 1130 mg APS was completely dispersed in 20 mL distilled water. This solution was dropped into the Py-monomer-containing solution and allowed to react for 24 h. After that, the black precipitate (the PPy nanofibers) was suction filtered and washed several times with 1 M HCl solution and distilled water, followed by drying in a vacuum oven at 80 ºC for 12 h. To prepare the carbon nanofibers with porous nitrogen-doped structure, the as-formed PPy nanofibers were mixed with KOH in a mass ratio of 1 : 2, and the mixture was heated up to 650 ºC for 0.5 h at a heating rate of 3 ºC min^{-1} and then cooled down to room temperature naturally under a N_2 atmosphere. The activated product was successively washed with 1 M HCl solution and distilled water until the filtrate became neutral. The PNCNFs were obtained after drying in a vacuum oven at 80 ºC overnight.

The PNCNFs were added into 50 mL distilled water and ultrasonically treated for 1 h. Subsequently, $PdCl_2$ was dissolved in 10 mL 1 M HCl solution, which was mixed with the PNCNF suspension with strong stirring for 1 h afterwards, and the pH of the above suspension was adjusted to 10 using 1 M NaOH solution. Icy cold aqueous 0.15 M $NaBH_4$ was added dropwise into the precursor solution, and it was further stirred for 12 h. After the reaction, the precipitate was washed with distilled water and ethanol, and then dried in a vacuum oven at 80 ^oC for 12 h. By using this method, three Pd/PNCNF composites were fabricated using 0.1, 0.2, and 0.3 mmol $PdCl_2$ precursors with the same amount of PNCNFs (50 mg). The amounts of $NaBH_4$ solution serving as reduction agent were 10, 30, and 45 mL, and the resulting samples were designated as Pd/PNCNF-1, Pd/PNCNF-2, and Pd/PNCNF-3, respectively. The pure Pd particles used in the characterization for reference were prepared by the same method without the PNCNFs.

7.2.2 Physical Characterization

XRD measurements were conducted on a GBC MMA generator and diffractometer with Cu Kα radiation. Raman spectra were collected on a JOBIN YVON HR800 Confocal system with 632.8 nm diode laser excitation using a 300 lines mm^{-1} grating. TGA was conducted on a SETARAM Thermogravimetric Analyzer (France). XPS was performed on a VG Scientific ESCALAB 2201XL instrument using Al Kα X-ray radiation and fixed analyzer transmission mode. The XPS data were analyzed using CasaXPS software, and all the results were calibrated by C 1s = 284.6 eV. FE-SEM images were collected on a JEOL 7500 microscope, and transmission electron microscope (TEM) experiments were carried out on a JEOL ARM-200F microscope. High angle annular dark-field (HAADF) STEM images and corresponding element mapping images were collected with the same

TEM equipped with a Centurio SSD EDS detector. BET surface area and pore size distribution (PSD) measurements were conducted by N_2 adsorption/desorption at 77 K on a Quantachrome Autosorb-IQ MP instrument.

7.2.3 Electrochemical Measurements

RDE tests were conducted in a standard three electrode cell connected to a computer-controlled potentiostat (Princeton 2273 and 616, Princeton Applied Research) at room temperature. A KCl saturated Ag/AgCl electrode and a platinum wire were used as the reference electrode and the counter electrode, respectively. The working electrodes were prepared by drop-pasting the samples onto a pre-polished GC electrode (5 mm in diameter). In brief, 4 mg catalyst was added into 2 mL Nafion/H_2O/isopropanol (m/m/m = 0.05/10/50) solution and ultrasonicated for 30 min to form a homogeneous catalyst ink (2 mg/mL). A total of 30 μL catalyst ink was then pipetted onto the glassy carbon electrode surface and allowed to dry in a fume cupboard at room temperature for 30 minutes. For comparison, a commercially available Pt/C (20 wt.% Pt on Vulcan XC-72) electrode was also fabricated using the same method described above. To test the ORR performance, LSV data were collected in O_2 saturated 0.1 M KOH solution with different rotation speeds from 400 to 1600 rpm from 0.1 to -0.8 V with a scan rate of 10 mV s^{-1}. The kinetic analysis was performed on the basis of the Koutecky-Levich (K-L) equations [278, 279]:

$$\frac{1}{j} = \frac{1}{j_k} + \frac{1}{j_d} = \frac{1}{j_k} + \frac{1}{B\omega^{\frac{1}{2}}} \tag{7.1}$$

$$B = 0.2nF(D_{O_2})^{\frac{2}{3}}\nu^{\frac{-1}{6}}C_{O_2} \tag{7.2}$$

where j, j_k, and j_d are the measured, kinetically controlled, and diffusion controlled current densities, respectively, and ω is the rotation rate, which is expressed in rpm. n represents the number of electrons transferred in the reduction of one O_2 molecule. F is the Faraday constant (F = 96485 C mol^{-1}), and D_{O2} is the diffusion coefficient of O_2 in 0.1 M KOH solution ($D_{O2} = 1.9 \times 10^{-5}$ cm^2 s^{-1}). v is the kinematic viscosity of the 0.1 M KOH solution (v = 0.01 cm^2 s^{-1}), and C_{O2} is the concentration of O_2 in this solution (C_{O2} =1 .2 $\times 10^{-6}$ mol cm^{-3}). The K-L plots were drawn based on $\omega^{-1/2}$ and j at a potential of -0.6 V in the limiting current potential region. From Equations (7.1) and (7.2), n and J_K (the kinetic-limiting current density) can be calculated from the slope of the linear fit line and the intercept of the K-L plots, respectively[278, 280]. The OER measurements were conducted in N_2 saturated 0.1 M KOH solution from 0.1 to 0.9 V at a scan rate of 10 mV s^{-1}. Cyclic voltammetry (CV) was performed with a scan rate of 10 mV s^{-1} in O_2 saturated 0.1 M KOH solution from 0.10 to -0.90 V and in Li-O_2 cells with the electrolyte consisting of 1 M $LiCF_3SO_3$ in TEGDME from 2.35 to 4.35 V.

For the preparation of the cathodes tested in Li-O_2 cells, 90 wt.% catalyst and 10 wt.% PTFE were mixed in isopropanol to make a catalyst slurry. It was homogeneously coated onto carbon paper and dried at 120 ^oC in a vacuum oven for 12 h. The typical loading of the slurry for the cathode was about 1.0±0.1 mg cm^{-2}. The CR 2032 coin-type cells with holes in their positive top covers were assembled in an Ar-filled Mbraun glove box (Germany) by stacking a glassy fiber separator between the catalyst cathode as the working electrode and the Li foil as the counter electrode. The electrolyte used in assembling the cell was 1 M $LiCF_3SO_3$ in TEGDME. Galvanostatic discharge/charge tests of the Li-O_2 cell were carried out at room temperature on a LAND CT 2001A multi-channel battery tester in an O_2-purged chamber with activated molecular sieves. The

current densities and specific capacities were calculated based on the amount of catalyst in the cathodes.

7.3 Results and Discussion

The synthetic procedure for the Pd/PNCNF composites is as shown in Figure 7.1. Briefly, PPy nanofibers were prepared by the polymerization reaction from pyrrole (Py) monomer. Afterwards, a facile one-step strategy was applied to prepare PNCNFs using PPy nanofibers as precursor and KOH as activating agent to form the porous nitrogen-doped structure. The Pd particles were then reduced and decorated on the surfaces of the PNCNFs.

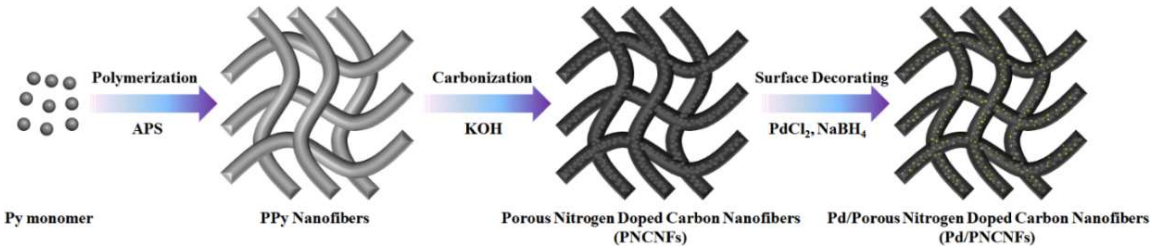

Figure 7.1 Schematic representation of the synthesis process for the 3D Pd/porous nitrogen-doped carbon-nanofiber (Pd/PNCNF) composites.

The weight percentages of the Pd in the Pd/PNCNF composites were acquired by TGA from 25 to 900 ^{o}C with a heating rate of 10 ^{o}C min^{-1} in air, as shown in Figure 7.2. The weight percentage of the pure Pd remains unchanged when the temperature reaches 900 ^{o}C, although it experiences a rise beginning at around 270 ^{o}C and a drop at around 770 ^{o}C, associated with the Pd oxidation and the oxide decomposition, respectively[103]. As for the pure PNCNFs, they all burned out during the heating process. Therefore, it is

concluded that the final mass left in the composites at 900 °C is that of the Pd particles, from which the content of Pd can be calculated. By using this method, the Pd weight percentages of the samples denoted as Pd/PNCNF-1, Pd/PNCNF-2, and Pd/PNCNF-3 can be estimated to be approximately 13, 25, and 38 wt.%, respectively.

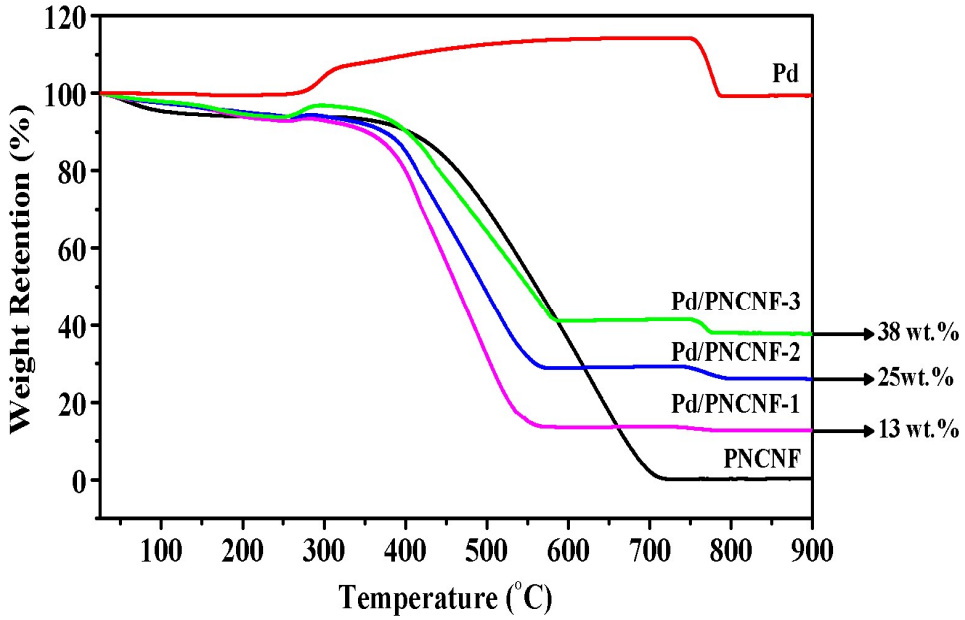

Figure 7.2 TGA curves of the pure PNCNFs, the Pd/PNCNF composites, and the Pd particles.

XRD patterns of the pure PNCNFs, the pure Pd particles, and the Pd/PNCNF composites with different Pd content in Figure 7.3(a) show that all the diffraction peaks agree perfectly with those of the cubic phase with lattice constant a = 0.3891 nm (JCPDS 65-2867), indicating the formation of Pd particles in the composites.

Raman spectroscopy was applied to further characterize the components of the composites in Figure 7.3(b). Two typical graphitic peaks are clearly observed from the pure PNCNFs and the Pd/PNCNF composites at around 1355 cm^{-1} and 1597 cm^{-1},

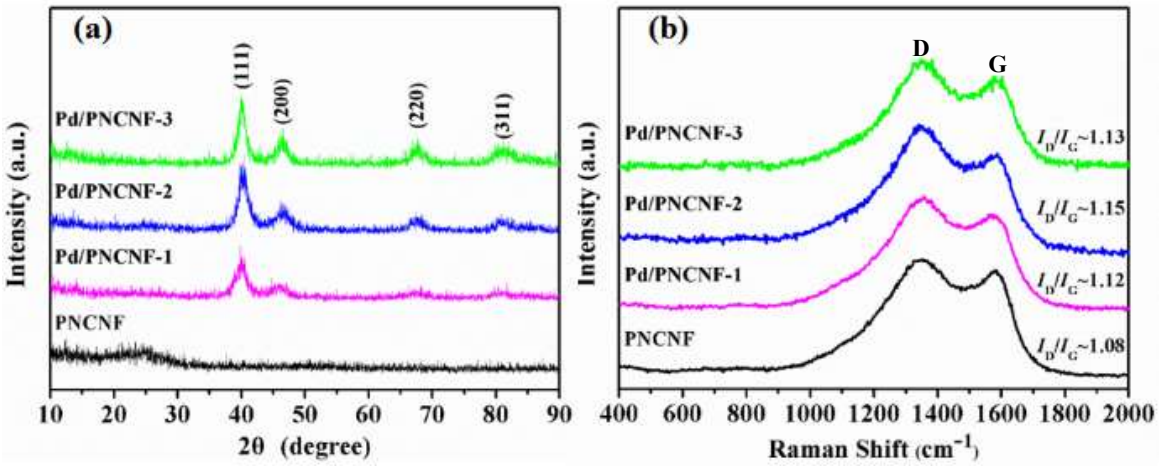

Figure 7.3 (a) XRD patterns, and (b) Raman spectra of the Pd/PNCNF-2 composite.

corresponding to the D band and the G band, respectively[225, 281]. This result, together with the XRD data, demonstrates that the Pd/PNCNF composites were successfully fabricated by the methods described above. As shown in the Raman spectra, the intensities of the D band are evidently higher than those of the G band, which suggests that large amounts of defects were formed in the carbon matrixes, resulting from the incorporation of nitrogen atoms into the carbon atomic layers. The intensity ratio of the D band to the G band (I_D/I_G) is extensively employed to estimate the degree of disorder of carbon materials[225]. It was found that the calculated I_D/I_G values of the Pd/PNCNF composites were larger than that of the pure PNCNFs. The Pd particles on the mesoporous carbon matrix is supposed to lower the degree of graphitization of the composites, because the π electrons in the graphitic carbon atoms are used to coordinate the adjacent Pd particles, enabling a homogeneous dispersion of Pd on the PNCNFs [270]. This is also the reason why there is a higher I_D/I_G value for Pd/PNCNF-2 than for the Pd/PNCNF-1 composite with lower Pd content. Notably, the degree of graphitization of the PNCNFs in the Pd/PNCNF-3 composite is decreased compared with the Pd/PNCNF-2 composite,

probably due to the agglomeration of Pd particles caused by their higher content in the Pd/PNCNF-3 composite.

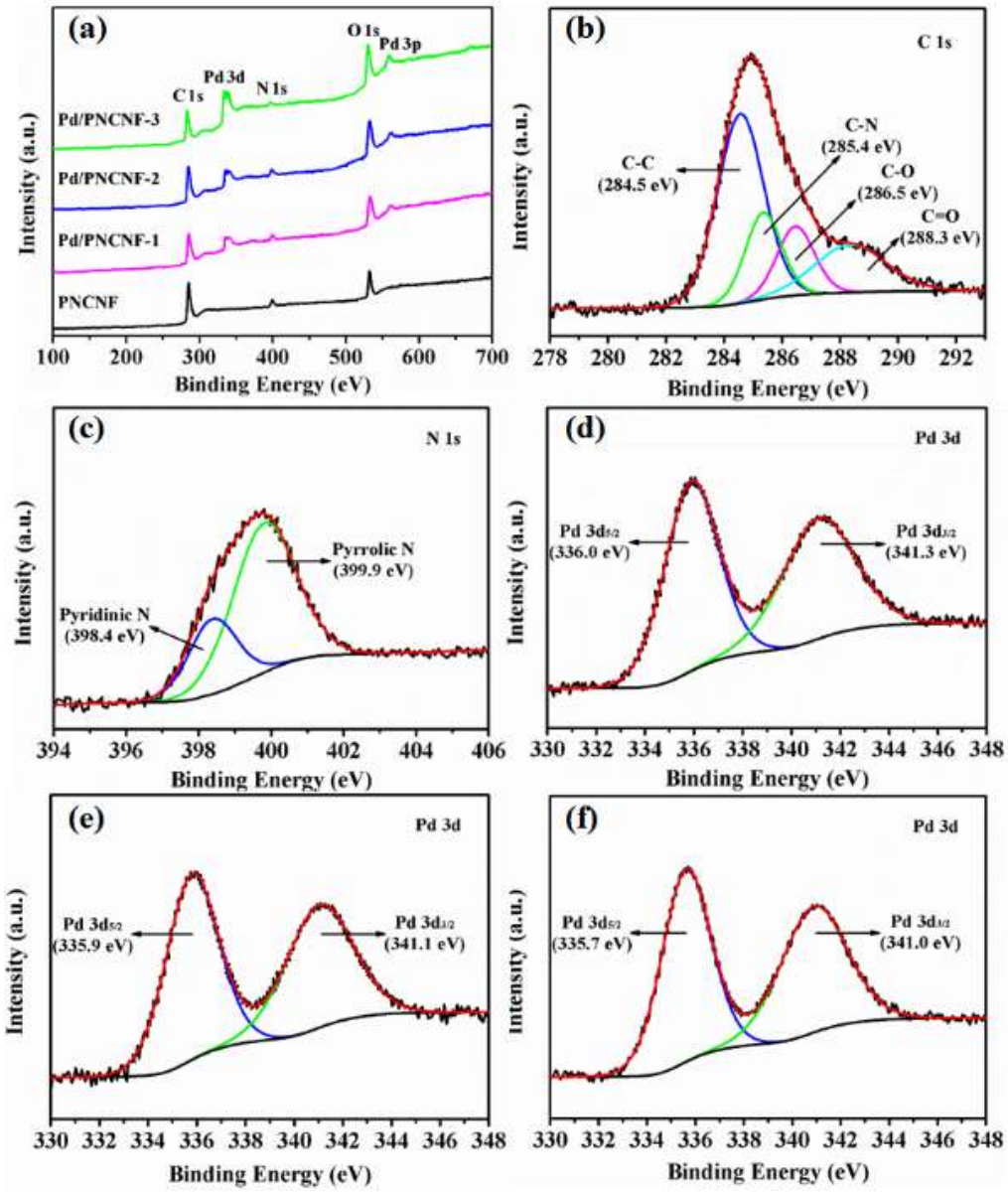

Figure 7.4 (a) XPS survey spectra of the pure PNCNFs, and the Pd/PNCNF composites; High-resolution (b) C 1s, (c) N 1s, and (d) Pd 3d XPS spectra of the Pd/PNCNF-2 composite; High-resolution Pd 3d XPS spectra of (e) the Pd/PNCNF-1, and (f) the Pd/PNCNF-3 composites.

To evaluate the surface chemical compositions and the nature of the elements in the composites, XPS measurements were utilized. As depicted in Figure 7.4 (a), the peaks of

the pure PNCNFs corresponding to C 1s, N 1s, and O 1s can be clearly observed in the survey spectra[282], confirming that the PNCNFs were successfully prepared. O is detected from the oxygenated functional groups on the carbon atoms. Besides these signals mentioned above, the composite spectra reveal the characteristic peaks of Pd 3d, and Pd 3p[282, 283], which further confirms the presence of the Pd in these composites.

Figure 7.4 (b)-(d) presents the high-resolution C 1s, N 1s and Pd 3d spectra of the Pd/PNCNF-2 composite. The high-resolution C 1s spectrum in Figure 7.4 (b) can be deconvoluted into four individual component peaks located at 284.5, 285.4, 286.5, and 288.3 eV, assigned to C-C, C-N, C-O, and C=O bonds, respectively[284]. As can be seen in Figure 7.4 (c), the high-resolution N 1s spectrum displays the coexistence of two N species. Its shape is ascribed to the transformation of part of the pyrrolic nitrogen at 399.9 eV within the five-membered rings of PPy into pyridinic nitrogen at 398.4 eV in the carbonization process for activating PPy nanofibers at a high temperature[272].

The high-resolution Pd 3d spectrum in metallic Pd normally exhibits two asymmetric peaks with binding energies of 335.3 and 340.6 eV, which correspond to the Pd $3d_{5/2}$ and the Pd $3d_{3/2}$ signals, respectively[283]. It is worth noting that a 0.7 eV positive shift of the binding energy takes place in the Pd/PNCNF-2 composite in Figure 7.4 (d) compared with that reported for metallic Pd, giving evidence that the nitrogen functional groups could increase the interaction between the Pd particles and the PNCNFs, and thus contribute to immobilizing the metal particles on the substrate materials[276]. What is more important is that this could promote superior dispersion of Pd nanoparticles on the PNCNFs and effectively prevent agglomeration.

Similarly, a 0.6 eV positive binding energy shift can be found in the Pd/PNCNF-1 composite in Figure 7.4 (e). The positive binding energy shift decreases to 0.4 eV in the Pd/PNCNF-3 composite in Figure 7.4 (f) because there is less effect of the nitrogen atoms on the Pd nanoparticles due to the excessive Pd loading, which was probably responsible for the poor Pd distribution and aggregates in the composite.

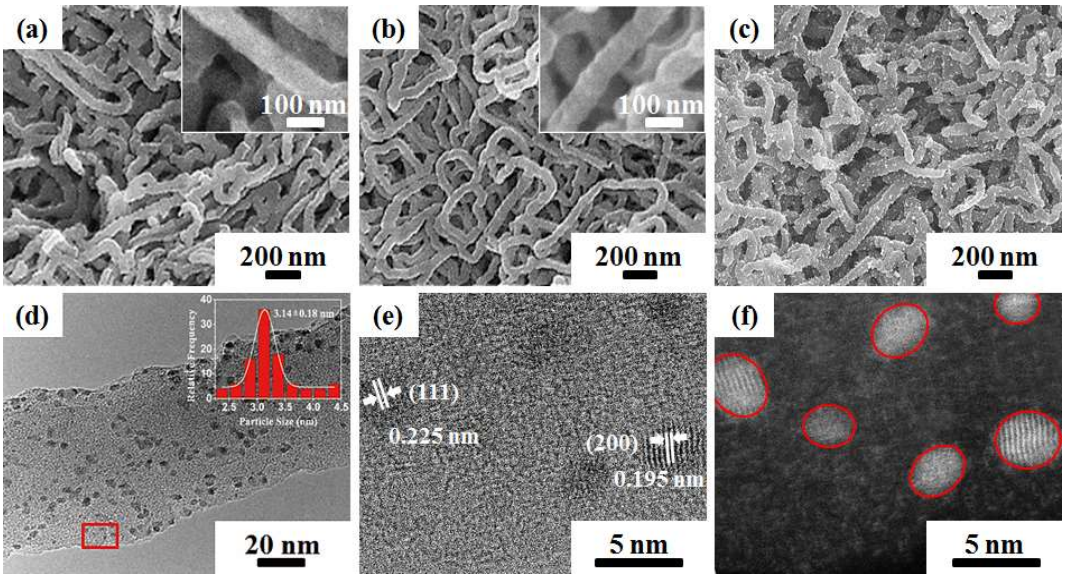

Figure 7.5 FE-SEM images of (a) the PPy nanofibers, with an enlarged area in the inset, (b) pure PNCNFs, with an enlarged area in the inset, (c) the Pd/PNCNF-2 composite; (d) TEM image and Pd particle size distribution (inset) of the Pd/PNCNF-2 composite; (e) high resolution TEM and (f) corresponding STEM images, with the Pd nanoparticles highlighted in the red circles in (f) generated from the area in the red box in (d).

FE-SEM images in Figure 7.5(a)-(b) demonstrate that both the PPy nanofibers and the pure PNCNFs feature a homogeneous cross-linked nanofiber web, with nanofiber diameters in the range of 60-80 nm. It can be observed, however, from the insets in these two images that the surface of the pure PNCNFs has become rougher than that of the PPy

nanofibers, which is due to the porous structure that was formed after the activation of the PPy nanofibers. The Pd nanoparticles are uniformly distributed on the 3D network of the PNCNF matrix in both the Pd/PNCNF-1 composite in Figure 7.6(a) and the Pd/PNCNF-2 composite in Figure 7.5(c), but more Pd nanoparticles can be traced in the Pd/PNCNF-2 composite. The Pd particles appear to have an uneven particle size and severe agglomeration in some parts of the Pd/PNCNF-3 composite in Figure 7.6(b), which is consistent with the Raman and XPS results.

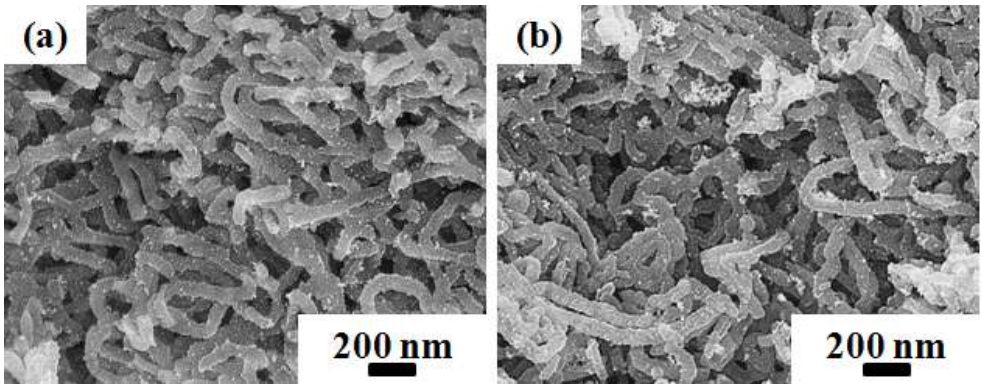

Figure 7.6 FE-SEM images of (a) the Pd/PNCNF-1, and (b) the Pd/PNCNF-3 composites.

The transmission electron microscope (TEM) image of the Pd/PNCNF-2 composite in Figure 7.5(d) confirms the FE-SEM results and illustrates that the PNCNFs are loaded with numerous well-dispersed Pd particles with a narrow size distribution of 3.1 ± 0.18 nm. The detailed morphology and structure of the Pd nanoparticles were further determined by high magnification bright-field (Figure 7.5(e)) and dark-field (Figure 7.5(f)) TEM images, generated from the area in the red box in Figure 7.5(d). These observations show several Pd nanoparticles on the PNCNF matrix with typical interplanar distances of 0.225 and 0.195 nm, in good agreement with the *d*-spacing of the (111) and (200) crystal planes of cubic Pd, respectively.

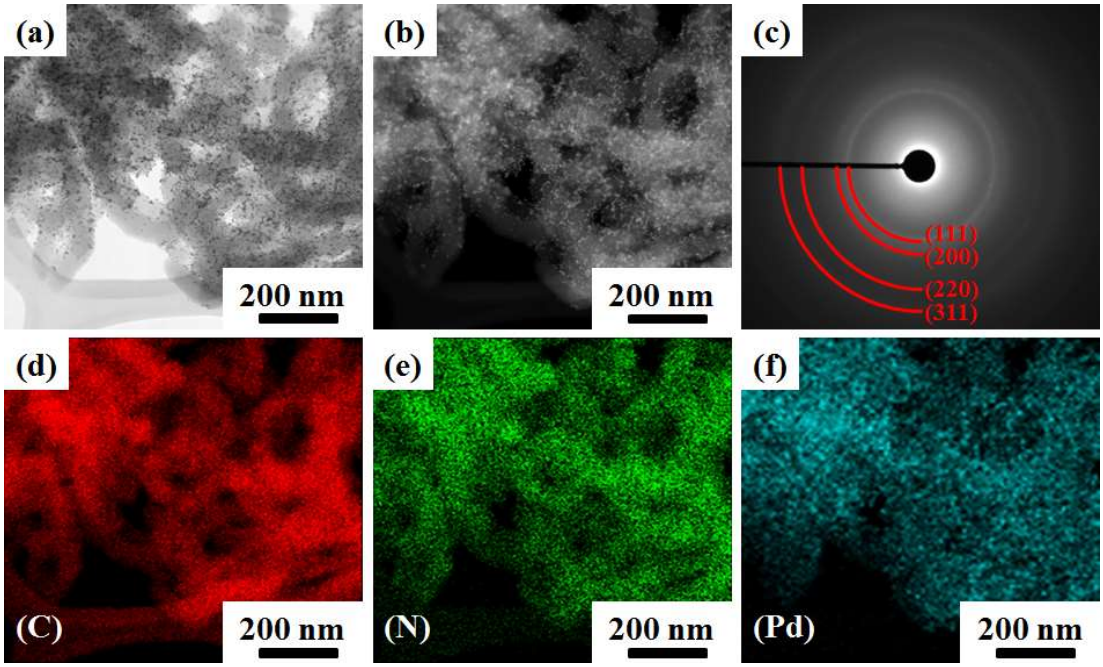

Figure 7.7 (a) TEM and (b) STEM images, (c) associated SAED pattern, and (d)-(f) corresponding element mapping images of the Pd/PNCNF-2 composite.

To verify the uniform Pd nanoparticle coating on the surfaces of the PNCNFs in the Pd/PNCNF-2 composite, overall views were captured in bright-field (Figure 7.7(a)) and dark-field (Figure 7.7(b)) TEM images, coupled with the corresponding selected area electron diffraction (SAED) patterns (Figure 7.7(c)) and EDS mapping images (Figure 7.7(d)-(f)). The indexed diffraction rings in the SAED pattern are assigned to the Pd structural characteristics, illustrating that the growth directions of the Pd nanoparticles are parallel to the (111), (200), (220), and (311) planes. This result is consistent with the XRD data and the structural analysis in the high magnification TEM image of the Pd/PNCNF-2 composite. The red spots in the EDS mapping image correspond to the presence of the element C, and the green spots correspond to the element N, illustrating the nitrogen doping on the PNCNF webs. The light blue spots associated with the element

Pd are distributed evenly throughout the whole area of the composite, providing further evidence that the Pd nanoparticles are well-dispersed onto the surfaces of the PNCNFs.

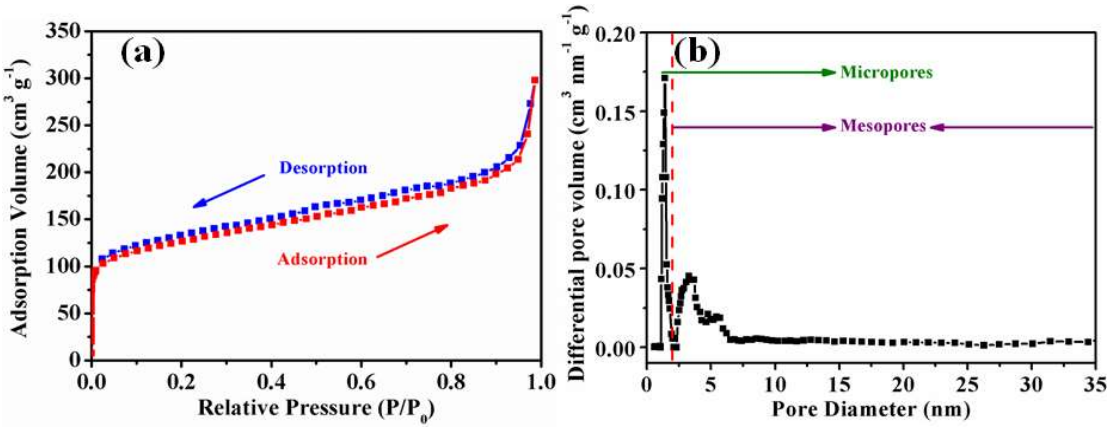

Figure 7.8 (a) N_2 adsorption-desorption isotherms, and (b) pore size distribution of the Pd/PNCNF-2 composite.

To further investigate the porous structure of the Pd/PNCNF-2 composite, N_2 adsorption-desorption isotherms were collected, as shown in Figure 7.8(a). The composite possesses a 561 m^2 g^{-1} BET surface area, and it shows the characteristics of type-IV N_2 isotherms according to the International Union of Pure and Applied Chemistry (IUPAC) classification. A steep increase in low pressure can be found, followed by a hysteresis loop at intermediate pressure, indicating that the composite contains both micropores and mesopores [285]. This result is further confirmed by the pore-size distribution (PSD) curves obtained from the N_2 isotherms using the Saito-Foley (SF) method, and it can be seen in Figure 7.8(b) that there is a sharp micropore peak located at around 1.4 nm, with the predominant mesopore peaks at around 3.2 nm in the Pd/PNCNF-2 composite. The micropores and mesopores are mainly beneficial for promoting electrolyte immersion of the surface of the composite[271, 272], and the mesopores could accommodate the Pd

particles from the point of view of dimensions and dispersion[276]. The porous structure of the composite thus is regarded as favouring the electrocatalytic improvement.

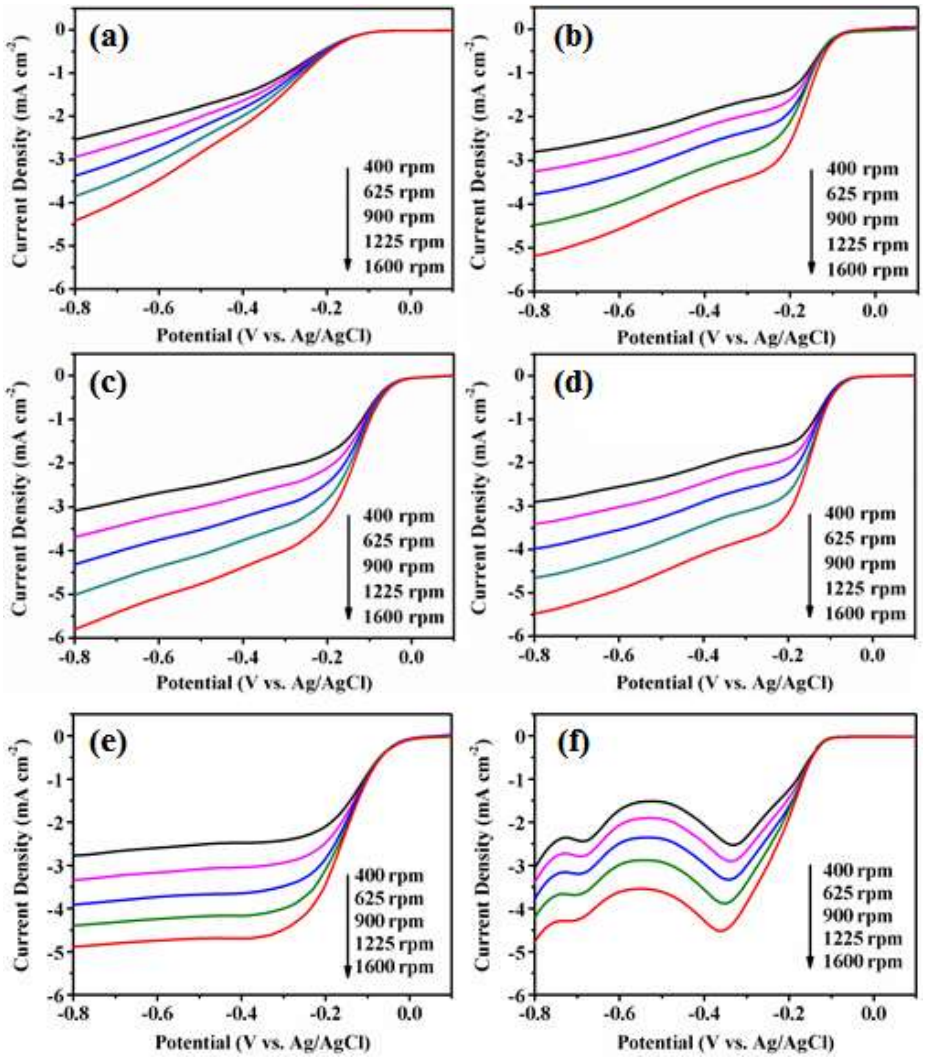

Figure 7.9 ORR LSV profiles of (a) the pure PNCNFs, (b) the Pd/PNCNF-1 composite, (c) the Pd/PNCNF-2 composite, (d) the Pd/PNCNF-3 composite, (e) the commercial 20 wt.% Pt/C, and (f) the pure Pd at different rotation speeds.

The electrocatalytic activity of the pure PNCNFs, the Pd/PNCNF composites, and the commercial 20 wt.% Pt/C towards the ORR/OER in aqueous solution (0.1 M KOH) were

characterized on a RDE. The LSV results of these samples at different rotation speeds are presented in Figure 7.9.

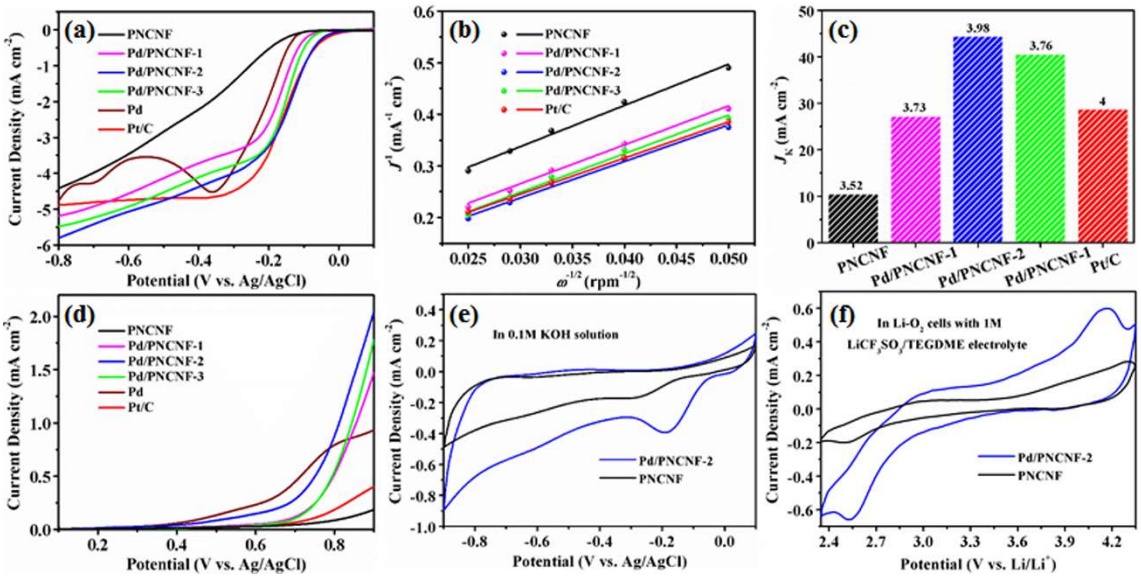

Figure 7.10 (a) ORR LSV profiles for the samples at a rotation speed of 1600 rpm; (b) K-L plots at -0.6 V; (c) kinetic limiting current densities and the corresponding electron-transfer numbers at -0.6 V; (d) OER LSV profiles of the different samples; CV curves of the pure PNCNFs and the Pd/PNCNF-2 composite measured in (e) 0.1 M KOH solution and (f) Li-O_2 cells with 1 M $LiCF_3SO_3$/TEGDME electrolyte.

Figure 7.10(a) provides voltammetric profiles of different samples at a rotation speed of 1600 rpm in O_2-saturated aqueous solution. It can be seen that the all of the Pd/PNCNF composites outperform the pure PNCNFs and the pure Pd in terms of ORR onset potential and current density at -0.8 V. The limiting current plateaus of the PNCNF and composite ORR curves are not as obvious as that for the 20 wt.% Pt/C. This phenomenon has been reported for many porous carbon-based catalysts, which is due to excess residual O_2 reduction on their structure with high surface area[280, 286]. Among these composites, the

Pd/PNCNF-2 composite displays the most positive onset potential of -42.89 mV and the highest current density of -5.81 mA cm^{-2} at -0.8 V. Nevertheless, the onset potential of the Pd/PNCNF-2 composite is close to that for the commercial 20 wt.% Pt/C at -0.8V, and the current density is even larger, indicating the excellent ORR activity of the Pd/PNCNF-2 composite. The pure Pd shows no limiting current behavior at all, which is consistent with the result reported by Al Abass et al.[287] This is because carbon supports could facilitate electron transfer in the catalysts, ensuring efficient electrocatalytic reactions in the RDE testing[288-290].

In Figure 7.10(b), K-L plots of different samples are presented from corresponding curves in Figure 7.9 at -0.6 V in the limiting current potential region, and the electron transfer number and kinetic limiting current density (J_K) have been calculated and are recorded in Figure 7.10(c). Typically, carbon catalysts exhibit low ORR activity with an inefficient two-electron processes[291, 292], while the electron transfer number of the pure PNCNF catalyst is 3.52, indicating that it involves both the two-electron and the four-electron processes. The main reason is that the nitrogen atoms, which were effectively introduced into the carbon matrix, could promote favorable electrocatalytic activity. The quantum mechanics calculations and previous electrocatalytic results give evidence that the improved ORR catalytic activity of the carbon material essentially originated from the active sites of pyridinic and pyrrolic nitrogen atoms[221, 275, 293]. By a simple carbonization method for PPy nanofibers, the PNCNFs with these nitrogen atoms in carbon rings were gained, evidenced by the XPS results, which are helpful to enhance the catalytic property of the pure PNCNFs. After further depositing Pd nanoparticles with high catalytic activity onto this ideal support material, the electron transfer number of the Pd/PNCNF-2 composite reach to 3.98, higher than those for the Pd/PNCNF-1 composite (3.73), and the

Pd/PNCNF-3 composite (3.76), and close to that for the commercial 20 wt.% Pt/C (4), suggesting that the Pd/PNCNF-2 composite delivers a more efficient four-electron transfer process[294]. The highest J_K value of the Pd/PNCNF-2 composite (44.44 mA cm^{-2}) further verifies its outstanding ORR performance among the pure PNCNFs and the other composites.

OER polarization curves measured in N_2-saturated 0.1 M KOH solution are shown in Figure 7.10(d). It is obvious that the commercial 20 wt.% Pt/C displays poor OER activity, and the pure PNCNFs and the pure Pd are also inactive towards the OER. The Pd/PNCNF composites present a more negative onset potential for the OER with a higher current density at 0.9 V, implying the composite catalysts hold superior OER property. Notably, the highest OER activity among the composites is yielded by the Pd/PNCNF-2 composite, which is consistent with the ORR results. Therefore, the outstanding electrocatalytic activities of the Pd/PNCNF-2 composite towards both the ORR and the OER confirm it to be a powerful bifunctional oxygen catalyst.

Figure 7.10(e) compares the cyclic voltammetry (CV) curves of the Pd/PNCNF-2 composite and the pure PNCNFs in O_2-saturated 0.1 M KOH at a scan rate of 10 mV s^{-1}. The Pd/PNCNF-2 composite exhibits a more positive ORR peak potential and higher peak current than those of the pure PNCNFs, which matches well with the results observed in the LSV measurements. In fact, the catalytic reaction mechanisms and measurements in different potential ranges for the oxygen catalysts are typically very different in aqueous and nonaqueous electrolytes. Even so, many previous results show that the catalytic performance characteristics of the catalysts tend to share similarities in these two electrolytes[247, 256]. This correlation implies that the successful application of

one catalyst in aqueous systems could also be extended to application in a nonaqueous Li-O_2 system.

Therefore, the CV differences between the LOBs containing the Pd/PNCNF-2 composite and the pure PNCNFs in $LiCF_3SO_3$/TEGDME electrolyte were studied, as shown in Figure 7.10(f). It should be noted that the Pd/PNCNF-2 composite displays a more positive ORR peak and a more negative OER peak, and the current densities of these peaks are larger than those of the pure PNCNFs. These data demonstrate that the Pd/PNCNF-2 composite not only presents admirable OER/ORR performances in aqueous electrolyte, but also shows promising bifunctional electrocatalytic activity in the non-aqueous electrolyte.

The LOBs performance of the pure PNCNF and the Pd/PNCNF composite cathodes is further evaluated in Figure 7.11. Figure 7.11(a) presents the first galvanostatic discharge/charge profiles at a current density of 100 mA g^{-1} from 2.35 to 4.35 V vs. Li^+/Li. The pure Pd shows high overpotential and low capacity due to the lack of conductive support loading. Note that the discharge/charge capacities of the pure PNCNF cathode are2533/1976 mA h g^{-1} with 59 % round-trip efficiency (the ratio of discharge voltage of 2.53 V to charge voltage of 4.28 V). The cathodes with the PNCNFs decorated by the Pd nanoparticles show dramatically improved round-trip performance and cathodes with the PNCNFs decorated by the Pd nanoparticles show dramatically improved round-trip performance and discharge/charge capacities. Briefly, the Pd/PNCNF-1 and Pd/PNCNF-3 cathodes deliver discharge/charge capacities of 7558/6071 and 8449/7697 mAh g^{-1}, with round-trip efficiencies of 62 % (2.60 V to 4.19 V) and 63 % (2.61 V to 4.14 V), respectively. It is remarkable that the Pd/PNCNF-2 cathode displays the highest

discharge/charge capacities of 10080/9405 mAh g^{-1} with 64 % round-trip efficiency (2.62 V to 4.09 V).

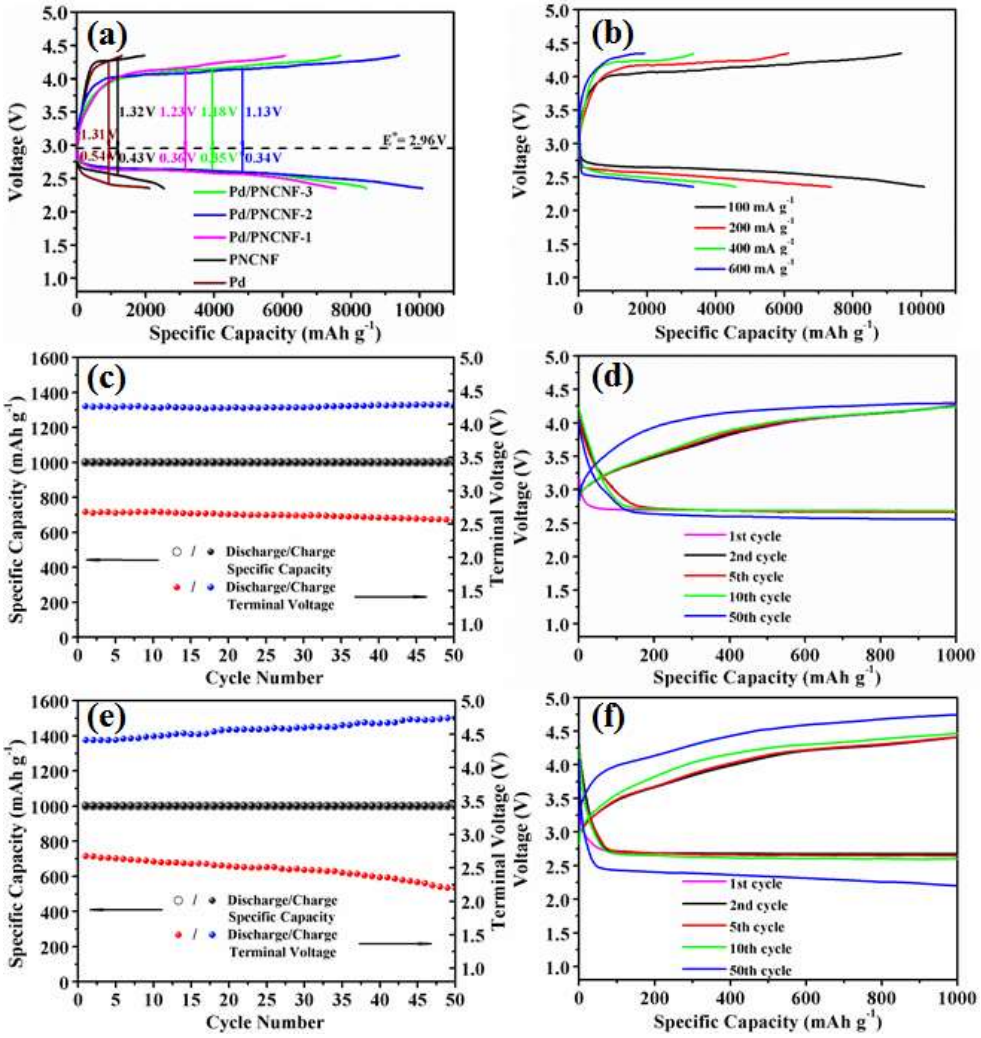

Figure 7.11 Comparison of the initial discharge/charge profiles of the Li-O_2 batteries from 2.35 to 4.35 V for (a) the pure Pd, the pure PNCNF, and the Pd/PNCNF cathodes at 100 mA g^{-1}, and (b) the Pd/PNCNF-2 cathode at different current densities; cycling performances (c, e), and the corresponding typical discharge/charge profiles (d, f) of the Li-O_2 cells for selected cycles, with (c, d) the Pd/PNCNF-2 and (e, f) the pure PNCNF cathodes under a capacity limit of 1000 mAh g^{-1} at 100 mA g^{-1}.

It is evident that all the coulombic efficiencies of the catalyst cathodes in Figure 7.11(a) are less than 100%. This is because most of them could not efficiently promote the catalytic reactions in the discharge and charge processes, and there are irreversible by-products formed by well-known side reactions, probably from the electrolyte decomposition and the corrosion of the carbon support[295-297], as evidenced by the following ex-situ XPS results.

Accordingly, I also assembled a LOB using only carbon paper cathode material, because it delivers capacity by itself, which may affect and confuse the results for the catalyst-containing cells. The current and specific capacities are calculated based on the average weight of the cathode materials, utilizing the same testing conditions. Clearly, the capacities of the carbon paper in Figure 7.12 are quite limited, suggesting that the carbon paper makes a negligible contribution to the catalyst capacity and that it is reasonable to employ carbon paper as the current collector in the research on LOBs.

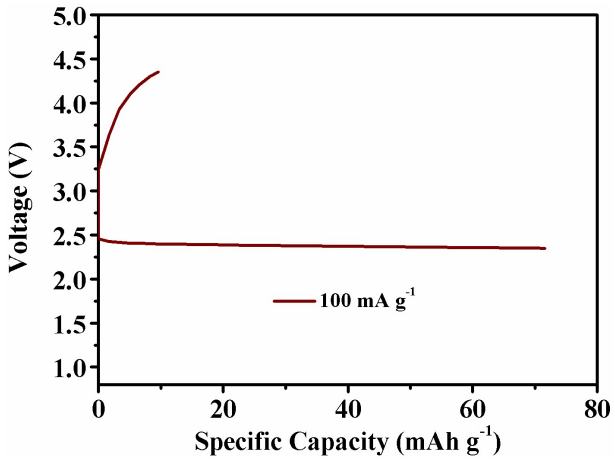

Figure 7.12 Initial discharge/charge profiles of the Li-O_2 batteries from 2.35 to 4.35 V for the carbon paper cathode at 100 mA g^{-1}.

The superior electrocatalytic performance of the Pd/PNCNF cathodes in the LOBs, as well as in the RDE measurements, could be attributed to the synergistic effects from the combination of the PNCNFs and the Pd nanoparticles. The PNCNFs with highly porous structure not only enable enough infiltration of the electrolyte and flow of gases, but also provide some electrocatalytic sites arising from the nitrogen doping for the nucleation of the discharge products. Furthermore, the PNCNFs, acting as a highly electrically conductive web, facilitate efficient electron transfer and the tri-phase reaction throughout the whole cathode. More importantly, after being made into a composite with Pd nanoparticles, the ORR/OER activity of the PNCNF catalyst is extraordinarily enhanced, indicating that the improvement in the performance of the catalyst materials mainly originates from the Pd contribution, in accordance with the reported results on Pd-containing catalyst[103, 265]. In addition, Pd nanoparticles can make full use of their high catalytic activity when they are decorated onto the PNCNF matrix, because the porous structure and nitrogen doping of the carbon nanofibers are assumed to coordinate the Pd particles in terms of dimensions and dispersion, as evidenced in the case of the Pd/PNCNF-2 cathode. The Pd/PNCNF-1 cathode delivers lower specific capacities because of less loading of the active material Pd. The Pd/PNCNF-3 cathode also shows poor electrocatalytic performance, which could possibly be due to the agglomeration and the uneven distribution of Pd particles. These results are in accordance with the data recorded in the aqueous solution, confirming that the optimum Pd content in the composite cathode is 25 wt.%.

Therefore, the electrocatalytic performance of the LOBs with the Pd/PNCNF-2 cathode was further studied. In Figure 7.11(b), as the current density is varied to 200, 400, and 600 mA g^{-1}, the Pd/PNCNF-2 cathode also shows highly attractive discharge/charge

performance of 7378/6119, 4586/3350, and 3350/1926 mAh g^{-1}, respectively. Figure 7.11(c) exhibits the continuously cycled galvanostatic discharge/recharge curves of the Pd/PNCNF-2 cathode at a current density of 100 mA g^{-1}, with a fixed specific capacity of 1000 mAh g^{-1}, including the terminal discharge/charge voltages for each cycle. Selected discharge/charge profiles are displayed in Figure 7.11(d). Favorable cycling stability is demonstrated for the LOB containing the Pd/PNCNF-2 cathode, and the discharge/charge terminal voltages remain stable over 50 cycles. It is believed that the Pd/PNCNF-2 composite displays the ability to perfectly deposit and decompose the discharge products, which is due to the substantial reaction sites in its unique structure for the O_2/Li_2O_2 conversion reactions on the surface of the composite. Because of the low overpotentials of the Pd/PNCNF-2 cathode, the electrolyte decomposition in each cycle is exceedingly limited, which could contribute to an extended device cycle life. For comparison, the cycling stability and selected discharge/charge curves of the pure PNCNF cathode are also included in Figure 7.11(e)-(f). Although it also can be discharged and recharged for 50 cycles, with a capacity of 1000 mAh g^{-1} as well, the discharge terminal voltage drops to 2.2 V, and the charge terminal voltage soars to 4.7 V, a 22.7 % decrease and 6.8 % increase of the initial discharge/charge terminal voltages (2.7/4.4 V), respectively.

Ex-situ XRD and FE-SEM investigations were conducted to identify the changes in the composition and morphology of the Pd/PNCNF-2 cathode. In Figure 7.13(b), the close-packed products have precipitated on the surface of the cathode after the cell was fully-discharged at the 1^{st} cycle to 2.35 V. Afterwards, this solid product disappears, and the fibrous structure of the cathode is regained in Figure 7.13(c) after the cell was fully

charged at the 1st cycle to 4.35 V, and this morphology of the cathode also remained at the 50th cycle, after charging at fixed capacity, as shown in Figure 7.13(d).

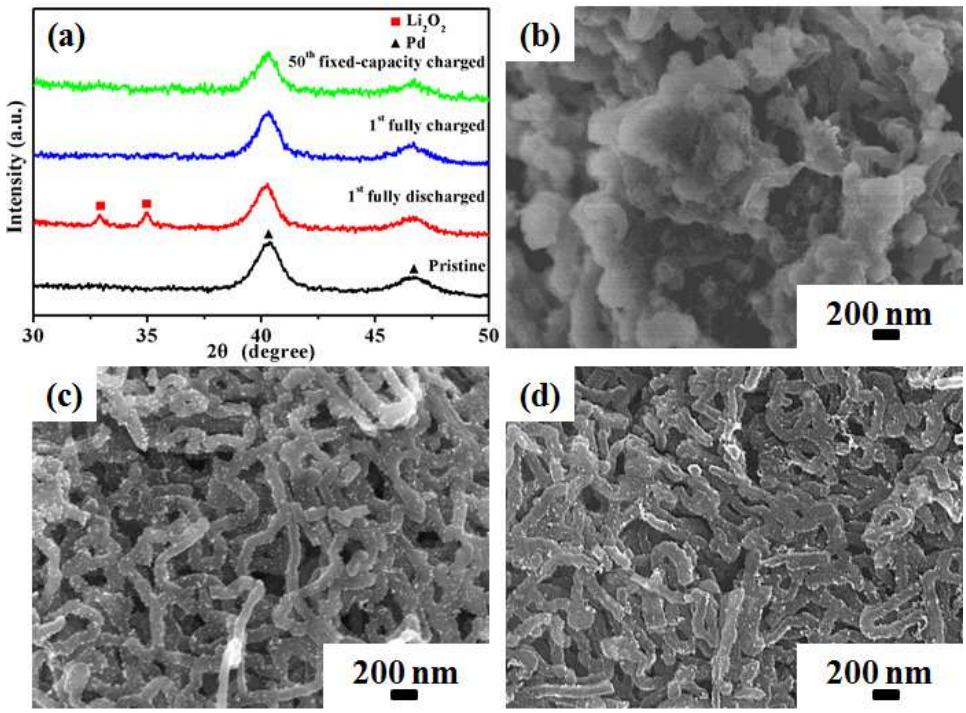

Figure 7.13 (a) XRD patterns at different discharge/charge stages; FE-SEM images of Pd/PNCNF-2 cathodes at (b) the 1st cycle, fully discharged (to 2.35 V), (c) the 1st cycle, fully charged (to 4.35 V), and (d) the 50th cycle, after fixed-capacity charged.

The XRD patterns at different discharge/charge stages give further evidence to support the results above, as shown in Figure 7.13(a). The characteristic Li_2O_2 peaks can be distinctly observed in the cathode after the 1st full discharge, implying that the crystalline part in the solid product in Figure 7.13(b) is Li_2O_2. Afterwards, the Li_2O_2 not be found in the cathode after the 50th fixed-capacity charge either, demonstrating that the Pd/PNCNF-2 cathode could efficiently catalyze the formation and decomposing of the Li_2O_2 during cycling, giving rise to the excellent cycling stability.

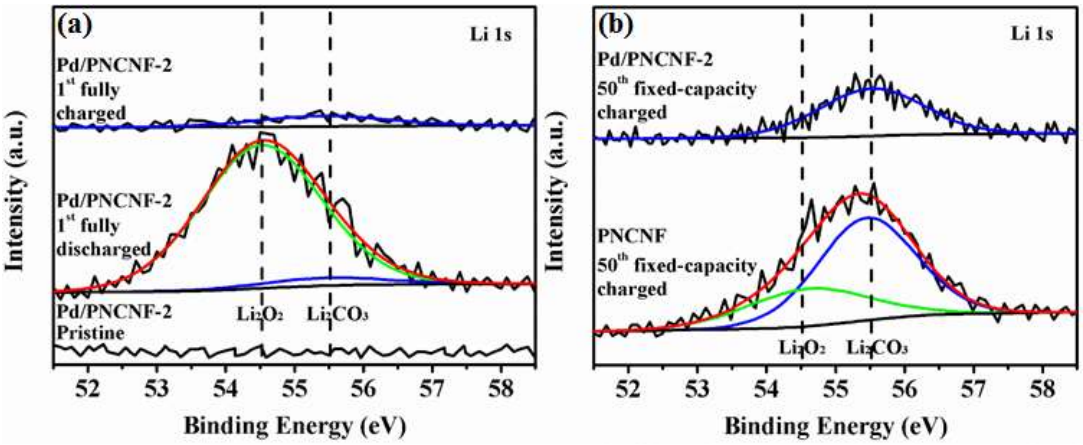

Figure 7.14 High-resolution Li 1s XPS spectra of (a) the Pd/PNCNF-2 cathode before cycling, in the 1st cycle, when fully discharged (to 2.35 V), and in the 1st cycle, when fully charged (to 4.35 V), and (b) the PNCNF and the Pd/PNCNF-2 cathodes in the 50th cycle, after fixed-capacity charging.

To further explore the product components in the charge and discharge process, high-resolution Li 1s XPS spectra of the cycled cathodes are included in Figure 7.14. In Figure 7.14(a), a high intensity Li_2O_2 peak (54.5 eV) could be detected in the spectrum of the Pd/PNCNF-2 cathode after the initial discharge, and the peak disappeared after the initial fixed-capacity charge. It should be noted that a Li_2CO_3 peak (55.5 eV) exists in these spectra, indicating that Li_2CO_3-dominated by-products were formed and could not be decomposed during cycling in the Pd/PNCNF-2 cathode. The by-products are widely reported to be generated by the side reactions from the electrolyte decomposition and the corrosion of the carbon support[295-297]. These by-products show low conductivity and catalytic activity, and their accumulation during cycling will cover the catalytic sites on the cathode, leading to poor electrocatalytic performances.

In Figure 7.14(b), only the Li_2CO_3 peak could be traced in the spectrum of the Pd/PNCNF-2 cathode after the 50th charge, while the spectrum of the PNCNF cathode

after the 50th charge displays two obvious Li_2O_2 and Li_2CO_3 peaks. Although the nitrogen doped carbon cathode could exhibit a certain amount of catalytic activity towards the reversible reactions in the LOBs, it has still been reported that Li_2O_2 was not decomposed completely in the cathode after charging[298, 299], aggravating the side reactions and leading to more by-product formation in the following cycles. The by-products in the PNCNF cathode in the first several cycles, however, are present only in a limited amount and could not significantly affect the catalytic performance, because the side reactions in each cycle could be controlled with a relatively low fixed capacity. As the cycle number increases, the successive accumulation of the by-products in the PNCNF cathode would be much more serious than in the Pd/PNCNF-2 cathode. The insulating by-products could cause cathode passivation and an increase in the discharge and charge overpotentials, leading to eventual failure of the battery containing the PNCNF cathode. Therefore, the overpotential difference for the PNCNF cathode is quite slight in the first several cycles, and it only becomes larger than that of the Pd/PNCNF-2 cathode after repeated cycles.

7.4 Conclusions

In summary, 3D PNCNF webs decorated by Pd nanoparticles were synthesized and present favorable catalytic activity towards both the ORR and the OER. The Pd/PNCNF cathode with optimized weight percentage of 25 Pd nanoparticles could deliver discharge/charge capacities of 10080/9405 mAh g^{-1} with the round-trip efficiency of 64 % at a current density of 100 mA g^{-1}. Even at a current density of 600 mA g^{-1}, discharge/charge capacities of 3350/1926 mAh g^{-1} could be achieved. With a fixed capacity of 1000 mA h g^{-1} over 50 cycles, the LOB containing this composite cathode could be continuously discharged and charged without obvious terminal voltage variation

at a current density of 100 mA g^{-1}. This excellent electrocatalytic performance benefits from the synergistic effects of the well-dispersed Pd nanoparticles with superior catalytic activity and the high porosity and conductivity of the PNCNFs. All these results suggest that the Pd/PNCNF composite is promising for use as a cathode catalyst material for advanced LOBs.

CHAPTER 8 CONCLUSIONS AND OUTLOOK

8.1 Conclusions

In my thesis, two kinds of anode materials for LIBs, including Ge/SWCNT and $PbGeO_3$/GNS composites, and two kinds of cathode materials for LOBs, MnO_2/GNS and Pd/PNCNF composites, have been investigated. The electrode composite materials exhibit superior electrochemical performance compared with those of each individual phase in them. For the LIB anodes, the improvement mainly results from highly enhanced electron or Li ion transport, high surface area, and enhanced stability against pulverization, which are beneficial for efficient Li ion intercalation and deintercalation. For the LOB anodes, the improvements are mainly attributed to abundant catalytic active sites, large surface area, and increased catalytic activity, which are helpful for promoting reversible Li_2O_2 formation and decomposition. These findings could broaden the current understanding of their structural evolution and related electrochemical behaviour. A summary of the results are provided in the following sections.

A vacuum filtration technique was applied to prepare Ge/SWCNT composite anode materials for LIBs, in which SWCNTs form robust three-dimensional architectures with nanosized Ge particles uniformly deposited on the surfaces of the SWCNTs. The composite anode material with 32 wt.% Ge showed a favourable discharge capacity of 417 mAh g^{-1} after 40 cycles. This superior electrochemical performance is due to the good distribution of high capacity Ge in the SWCNT network. The structure could enhance its electrical conductivity and offer void space to buffer the Ge nanoparticle volume changes,

which is helpful for enabling more channels for the Li ion insertion and deinsertion during the charge-discharge processes.

$PbGeO_3$/GNS composites were prepared by an efficient one-step, in-situ hydrothermal method, in which $PbGeO_3$ nanowires are embedded in conductive and interconnected GNS networks. The main electrochemical reaction mechanism proposed is that $PbGeO_3$ decomposes into Pb, Ge, and Li_2O, resulting in reversible lithiation and de-lithiation for Pb and Ge, with a partial Ge oxidation process. The composite anode with 20 wt.% GNS for LIBs could deliver a discharge capacity of 607 mAh g^{-1} at 100 mA g^{-1} after 50 cycles. Even at a high current density of 1600 mA g^{-1}, a capacity of 406 mAh g^{-1} can be obtained. The results are mainly attributed to the GNS matrix, which could maintain the anode structural integrity and provide more efficient tunnels for electron or Li ion transport, enhancing the cell's electrochemical activities during cycling.

A fast and effective microwave autoclave method was used to prepare MnO_2/GNS composite, in which MnO_2 nanoflakes were decorated on the surfaces of the 3D GNS skeleton. The MnO_2/GNS composite cathode for LOBs could deliver discharge/charge capacities of 5862/5572 mAh g^{-1}, respectively, with round-trip efficiency of 64 % at 100 mA g^{-1}. Even at a high current density of 600 mA g^{-1}, it exhibited discharge/charge capacities of 3566/2720 mAh g^{-1}, respectively. With a fixed capacity of 1000 mAh g^{-1}, this cathode could be cycled with low overpotentials over 50 cycles. It showed superior ORR and OER catalytic performances, mainly because of its excellent conductivity and adequate space to promote the catalytic reactions.

Pd/PNCNF composite were prepared and investigated as cathode catalyst material for LOBs. The cathode with 25 wt.% Pd nanoparticles could deliver discharge/charge capacities of 10080/9405 mAh g^{-1} with round-trip efficiency of 64 % at 100 mA g^{-1}. Even at a high current density of 600 mA g^{-1}, discharge/charge capacities of 3350/1926 mAh g^{-1} could be obtained. With a fixed capacity of 1000 mA h g^{-1} over 50 cycles, the cathode displayed stable cycling behaviour at 100 mA g^{-1}. Its remarkable performance results from the synergistic effects of the well-dispersed Pd nanoparticles with good catalytic activity, and the high porosity and conductivity of the PNCNF matrix.

8.2 Outlook

This thesis has mainly focused on anode materials for LIBs and cathode materials for LOBs. Cathode materials for LIBs, anode materials for LOBs, and their electrolytes and binders also need to be developed to promote the commercialization of the next generation of batteries. In addition to these, some further research efforts could be conducted based on the thesis as follows:

Flexible LIB batteries are arousing more interest because of the market demand for bendable electronic devices. Free-standing Ge/SWCNT composite anodes have been investigated in this thesis, and the results showed that they are a suitable candidate for the anode material. To optimize their battery performance, more work should be conducted, including adjusting the film thickness and preparing Ge nanoparticles with different particle sizes. Furthermore, a promising film cathode should be selected to couple with these free-standing anodes for the fabrication of fully bendable batteries.

The hydrothermal method is a widely used method to prepare nanosized materials, and the microwave autoclave assisted hydrothermal method is a novel synthesis strategy that features fast, high productivity, low temperature, environmental friendliness, and energy saving. $PbGeO_3$/GNS and MnO_2/GNS composite materials were obtained by these techniques, respectively. Actually, both methods could perfectly tune the chemical composition, particle shape, and crystallite size in a simple and effective way. The reaction conditions could be adjusted, including by changing the amount, concentration, and pH of the precursor solution, the reaction temperature, and the duration time, to form nanoparticles with designed morphologies and structures, which can strongly regulate the electrochemical performance of the electrode material.

Catalyst materials with different preferred planes have been proved to have different electrocatalytic activities. The preferred planes of MnO_2 and Pd nanoparticles could be adjusted to yield the best performance.

In-situ characterization methods, including in-situ Raman spectroscopy, in-situ TEM, and synchrotron radiation and neutron techniques, are essential for investigating the intermediates, surface kinetics, chemical bonding, and the related structural and compositional variations in the discharge and charge processes. Moreover, a combined computational and experimental approach is also needed to systematically study the electrode materials. Additionally, the disadvantages of nanomaterials owing to their high surface area need to be considered. The nanomaterials normally display low density and high reactivity in terms of side reactions, leading to large irreversible capacity and electrolyte decomposition. Surface modification could be used to minimize this effect of nanomaterials.

In conclusion, the author is firmly convinced that the existing problems are being slowly overcome and that research is advancing in the right direction, so that the future for the next generation of batteries is likely to be brighter ahead.

REFERENCES

[1] B. Dunn, H. Kamath, J.-M. Tarascon, Electrical energy storage for the grid: a battery of choices, Science 2011, 334, 928.

[2] M. Meinshausen, N. Meinshausen, W. Hare, S. C. Raper, K. Frieler, R. Knutti, D. J. Frame, M. R. Allen, Greenhouse-gas emission targets for limiting global warming to 2 ^{o}C, Nature 2009, 458, 1158.

[3] M. Z. Jacobson, M. A. Delucchi, Providing all global energy with wind, water, and solar power, Part I: Technologies, energy resources, quantities and areas of infrastructure, and materials, Energy Policy 2011, 39, 1154.

[4] M. S. Whittingham, Lithium batteries and cathode materials, Chemical Reviews 2004, 104, 4271.

[5] L. Ji, Z. Lin, M. Alcoutlabi, X. Zhang, Recent developments in nanostructured anode materials for rechargeable lithium-ion batteries, Energy & Environmental Science 2011, 4, 2682.

[6] Y. P. Wu, C. Jiang, C. Wan, R. Holze, Anode materials for lithium ion batteries by oxidative treatment of common natural graphite, Solid State Ionics 2003, 156, 283.

[7] Y. Idota, T. Kubota, A. Matsufuji, Y. Maekawa, T. Miyasaka, Tin-based amorphous oxide: a high-capacity lithium-ion storage material, Science 1997, 276, 1395.

[8] G. M. Zhou, F. Li, H. M. Cheng, Progress in flexible lithium batteries and future prospects, Energy & Environmental Science 2014, 7, 1307.

[9] O. K. Park, Y. Cho, S. Lee, H.-C. Yoo, H.-K. Song, J. Cho, Who will drive electric vehicles, olivine or spinel?, Energy & Environmental Science 2011, 4, 1621.

[10]V. Etacheri, R. Marom, R. Elazari, G. Salitra, D. Aurbach, Challenges in the development of advanced Li-ion batteries: a review, Energy & Environmental Science 2011, 4, 3243.

[11]Z. Y. Wen, C. Shen, Y. Lu, Air Electrode for the Lithium-Air Batteries: Materials and Structure Designs, ChemPlusChem 2015, 80, 270.

[12]J.-W. Jung, C.-L. Lee, S. Yu, I.-D. Kim, Electrospun nanofibers as a platform for advanced secondary batteries: a comprehensive review, Journal of Materials Chemistry A 2016, 4, 703.

[13]J.-M. Tarascon, M. Armand, Issues and challenges facing rechargeable lithium batteries, Nature 2001, 414, 359.

[14]J. B. Goodenough, Y. Kim, Challenges for rechargeable Li batteries, Chemistry of Materials 2009, 22, 587.

[15]M. S. Whittingham, Electrical energy storage and intercalation chemistry, Science 1976, 192, 1126.

[16]K. Mizushima, P. Jones, P. Wiseman, J. B. Goodenough, Li_xCoO_2 ($0<x<-1$): A new cathode material for batteries of high energy density, Materials Research Bulletin 1980, 15, 783.

[17]H. Ikeda, K. Narukawa, H. Nakashima, Sanyo Patent, Japanese 1769661, 1981.

[18]J. B. Goodenough, K.-S. Park, The Li-ion rechargeable battery: a perspective, Journal of the American Chemical Society 2013, 135, 1167.

[19]B. Song, H. Liu, Z. Liu, P. Xiao, M. O. Lai, L. Lu, High rate capability caused by surface cubic spinels in Li-rich layer-structured cathodes for Li-ion batteries, Scientific Reports 2013, 3, 3094.

[20]Z. Lu, L. Beaulieu, R. Donaberger, C. Thomas, J. Dahn, Synthesis, Structure, and Electrochemical Behavior of $Li[Ni_xLi_{1/3-2x/3}Mn_{2/3-x/3}]O_2$, Journal of The Electrochemical Society 2002, 149, A778.

[21]W. Y. Li, H. B. Yao, K. Yan, G. Y. Zheng, Z. Liang, Y.-M. Chiang, Y. Cui, The synergetic effect of lithium polysulfide and lithium nitrate to prevent lithium dendrite growth, Nature Communications 2015, 6.

[22]K. J. Harry, D. T. Hallinan, D. Y. Parkinson, A. A. MacDowell, N. P. Balsara, Detection of subsurface structures underneath dendrites formed on cycled lithium metal electrodes, Nature Materials 2014, 13, 69.

[23]M. Winter, J. O. Besenhard, M. E. Spahr, P. Novak, Insertion electrode materials for rechargeable lithium batteries, Advanced Materials 1998, 10, 725.

[24]M. S. Mauter, M. Elimelech, Environmental applications of carbon-based nanomaterials, Environmental Science & Technology 2008, 42, 5843.

[25]L. Dai, D. W. Chang, J. B. Baek, W. Lu, Carbon nanomaterials for advanced energy conversion and storage, Small 2012, 8, 1130.

[26]A. C. Neto, F. Guinea, N. M. Peres, Drawing conclusions from graphene, Physics World 2006, 19, 33.

[27]K. Persson, V. A. Sethuraman, L. J. Hardwick, Y. Hinuma, Y. S. Meng, A. van der Ven, V. Srinivasan, R. Kostecki, G. Ceder, Lithium Diffusion in Graphitic Carbon, The Journal of Physical Chemistry Letters 2010, 1, 1176.

[28]N. Jayaprakash, J. Shen, S. S. Moganty, A. Corona, L. A. Archer, Porous Hollow Carbon@Sulfur Composites for High-Power Lithium-Sulfur Batteries, Angewandte Chemie International Edition 2011, 123, 6026.

[29]S. Augustin, V. Hennige, G. Hörpel, C. Hying, Ceramic but flexible: new ceramic membrane foils for fuel cells and batteries, Desalination 2002, 146, 23.

[30] S. Y. Chew, S. H. Ng, J. Wang, P. Novák, F. Krumeich, S. L. Chou, J. Chen, H. K. Liu, Flexible free-standing carbon nanotube films for model lithium-ion batteries, Carbon 2009, 47, 2976.

[31] J. Wang, J. Wang, Z. Sun, X. Gao, C. Zhong, S. Chou, H. Liu, A germanium/single-walled carbon nanotube composite paper as a free-standing anode for lithium-ion batteries, Journal of Materials Chemistry A 2014, 2, 4613.

[32] S. Klink, E. Ventosa, W. Xia, F. La Mantia, M. Muhler, W. Schuhmann, Tailoring of CNT surface oxygen groups by gas-phase oxidation and its implications for lithium ion batteries, Electrochemistry Communications 2012, 15, 10.

[33] K. S. Novoselov, A. K. Geim, S. Morozov, D. Jiang, Y. Zhang, S. a. Dubonos, I. Grigorieva, A. Firsov, Electric field effect in atomically thin carbon films, Science 2004, 306, 666.

[34] X. Wang, G. Sun, P. Routh, D.-H. Kim, W. Huang, P. Chen, Heteroatom-doped graphene materials: syntheses, properties and applications, Chemical Society Reviews 2014, 43, 7067.

[35] V. Georgakilas, M. Otyepka, A. B. Bourlinos, V. Chandra, N. Kim, K. C. Kemp, P. Hobza, R. Zboril, K. S. Kim, Functionalization of graphene: covalent and non-covalent approaches, derivatives and applications, Chemical Reviews 2012, 112, 6156.

[36] W. S. Hummers, R. E. Offeman, Preparation of Graphitic Oxide, Journal of the American Chemical Society 1958, 80, 1339.

[37] G. Wang, X. Shen, J. Yao, J. Park, Graphene nanosheets for enhanced lithium storage in lithium ion batteries, Carbon 2009, 47, 2049.

[38] J. Z. Wang, C. Zhong, D. Wexler, N. H. Idris, Z. X. Wang, L. Q. Chen, H. K. Liu, Graphene-Encapsulated Fe_3O_4 Nanoparticles with 3D Laminated Structure as Superior Anode in Lithium Ion Batteries, Chemistry-A European Journal 2011, 17, 661.

[39] Y. Shi, J. Z. Wang, S. L. Chou, D. Wexler, H. J. Li, K. Ozawa, H. K. Liu, Y. P. Wu, Hollow structured Li_3VO_4 wrapped with graphene nanosheets in situ prepared by a one-pot template-free method as an anode for lithium-ion batteries, Nano Letters 2013, 13, 4715.

[40] A. Dey, Electrochemical alloying of lithium in organic electrolytes, Journal of The Electrochemical Society 1971, 118, 1547.

[41] M. R. Palacin, Recent advances in rechargeable battery materials: a chemist's perspective, Chemical Society Reviews 2009, 38, 2565.

[42] C. J. Wen, R. A. Huggins, Thermodynamic Study of the Lithium-Tin System, Journal of The Electrochemical Society 1981, 128, 1181.

[43] H. Wu, Y. Cui, Designing nanostructured Si anodes for high energy lithium ion batteries, Nano Today 2012, 7, 414.

[44] W. Weydanz, M. Wohlfahrt-Mehrens, R. Huggins, A room temperature study of the binary lithium-silicon and the ternary lithium-chromium-silicon system for use in rechargeable lithium batteries, Journal of Power Sources 1999, 81, 237.

[45] X. H. Liu, S. Huang, S. T. Picraux, J. Li, T. Zhu, J. Y. Huang, Reversible nanopore formation in Ge nanowires during lithiation-delithiation cycling: An in situ transmission electron microscopy study, Nano Letters 2011, 11, 3991.

[46] D. J. Xue, S. Xin, Y. Yan, K. C. Jiang, Y. X. Yin, Y. G. Guo, L. J. Wan, Improving the electrode performance of Ge through Ge@C core-shell nanoparticles and graphene networks, Journal of the American Chemical Society 2012, 134, 2512.

[47] W. H. Li, Z. Z. Yang, J. X. Cheng, X. W. Zhong, L. Gu, Y. Yu, Germanium nanoparticles encapsulated in flexible carbon nanofibers as self-supported electrodes for high performance lithium-ion batteries, Nanoscale 2014, 6, 4532.

[48]N. Rudawski, B. Yates, M. Holzworth, K. Jones, R. Elliman, A. Volinsky, Ion beam-mixed Ge electrodes for high capacity Li rechargeable batteries, Journal of Power Sources 2013, 223, 336.

[49]G. L. Cui, L. Gu, L. J. Zhi, N. Kaskhedikar, P. A. van Aken, K. Müllen, J. Maier, A germanium-carbon nanocomposite material for lithium batteries, Advanced Materials 2008, 20, 3079.

[50]M.-H. Seo, M. Park, K. T. Lee, K. Kim, J. Kim, J. Cho, High performance Ge nanowire anode sheathed with carbon for lithium rechargeable batteries, Energy & Environmental Science 2011, 4, 425.

[51]M.-H. Park, K. Kim, J. Kim, J. Cho, Flexible Dimensional Control of High-Capacity Li-Ion-Battery Anodes: From 0D Hollow to 3D Porous Germanium Nanoparticle Assemblies, Advanced Materials 2010, 22, 415.

[52]Y. Xiao, M. Cao, L. Ren, C. Hu, Hierarchically porous germanium-modified carbon materials with enhanced lithium storage performance, Nanoscale 2012, 4, 7469.

[53]H. Lee, M. G. Kim, C. H. Choi, Y.-K. Sun, C. S. Yoon, J. Cho, Surface-stabilized amorphous germanium nanoparticles for lithium-storage material, The Journal of Physical Chemistry B 2005, 109, 20719.

[54]M. G. Kim, J. Cho, Nanocomposite of amorphous Ge and Sn nanoparticles as an anode material for Li secondary battery, Journal of The Electrochemical Society 2009, 156, A277.

[55]X. Gao, Novel germanium/polypyrrole composite for high power lithium-ion batteries, Scientific Reports 2014, 4, 6095.

[56]D. Li, K. H. Seng, D. Shi, Z. Chen, H. K. Liu, Z. Guo, A unique sandwich-structured C/Ge/graphene nanocomposite as an anode material for high power lithium ion batteries, Journal of Materials Chemistry A 2013, 1, 14115.

[57]S. Jin, C. Wang, Synthesis and first investigation of excellent lithium storage performances of Fe_2GeO_4/reduced graphene oxide nanocomposite, Nano Energy 2014, 7, 63.

[58]Z. Chen, Y. Yan, S. Xin, W. Li, J. Qu, Y. G. Guo, W. G. Song, Copper germanate nanowire/reduced graphene oxide anode materials for high energy lithium-ion batteries, Journal of Materials Chemistry A 2013, 1, 11404.

[59]W. Li, X. Wang, B. Liu, S. Luo, Z. Liu, X. Hou, Q. Xiang, D. Chen, G. Shen, Highly reversible lithium storage in hierarchical $Ca_2Ge_7O_{16}$ nanowire arrays/carbon textile anodes, Chemistry-A European Journal 2013, 19, 8650.

[60]F. Zou, X. L. Hu, L. Qie, Y. Jiang, X. Q. Xiong, Y. Qiao, Y. H. Huang, Facile synthesis of sandwiched Zn_2GeO_4-graphene oxide nanocomposite as a stable and high-capacity anode for lithium-ion batteries, Nanoscale 2014, 6, 924.

[61]P. Poizot, S. Laruelle, S. Grugeon, L. Dupont, J. Tarascon, Nano-sized transition-metal oxides as negative-electrode materials for lithium-ion batteries, Nature 2000, 407, 496.

[62]L. W. Ji, Z. Lin, M. Alcoutlabi, X. W. Zhang, Recent developments in nanostructured anode materials for rechargeable lithium-ion batteries, Energy & Environmental Science 2011, 4, 2682.

[63]M. Reddy, G. Subba Rao, B. Chowdari, Metal oxides and oxysalts as anode materials for Li ion batteries, Chemical Reviews 2013, 113, 5364.

[64]J. P. Gabano, V. Déchenaux, G. Gerbier, J. Jammet, D-Size Lithium Cupric Sulfide Cells, Journal of The Electrochemical Society 1972, 119, 459.

[65]M. S. Whittingham, Chemistry of intercalation compounds: metal guests in chalcogenide hosts, Progress in Solid State Chemistry 1978, 12, 41.

[66]T. Kaun, P. Nelson, L. Redey, D. Vissers, G. Henriksen, High temperature lithium/sulfide batteries, Electrochimica acta 1993, 38, 1269.

[67]J. Xiao, D. Choi, L. Cosimbescu, P. Koech, J. Liu, J. P. Lemmon, Exfoliated MoS_2 nanocomposite as an anode material for lithium ion batteries, Chemistry of Materials 2010, 22, 4522.

[68]C. Feng, L. Huang, Z. Guo, H. Liu, Synthesis of tungsten disulfide (WS_2) nanoflakes for lithium ion battery application, Electrochemistry Communications 2007, 9, 119.

[69]Z. Zhang, Development of advanced materials for rechargeable lithium-ion batteries, University of Wollongong Thesis Collection, 2015.

[70]R. Black, B. Adams, L. Nazar, Non-Aqueous and Hybrid Li-O_2 Batteries, Advanced Energy Materials 2012, 2, 801.

[71]J. Lu, L. Li, J.-B. Park, Y.-K. Sun, F. Wu, K. Amine, Aprotic and aqueous Li-O_2 batteries, Chemical Reviews 2014, 114, 5611.

[72]K. F. Blurton, A. F. Sammells, Metal/air batteries: Their status and potential-a review, Journal of Power Sources 1979, 4, 263.

[73]K. M. Abraham, Z. Jiang, A Polymer Electrolyte-Based Rechargeable Lithium/Oxygen Battery, Journal of The Electrochemical Society 1996, 143, 1.

[74]J. Read, Ether-based electrolytes for the lithium/oxygen organic electrolyte battery, Journal of The Electrochemical Society 2006, 153, A96.

[75]T. Ogasawara, A. Debart, M. Holzapfel, P. Novak, P. G. Bruce, Rechargeable Li_2O_2 electrode for lithium batteries, Journal of the American Chemical Society 2006, 128, 1390.

[76]Z. Ma, X. X. Yuan, L. Li, Z. F. Ma, D. P. Wilkinson, L. Zhang, J. J. Zhang, A review of cathode materials and structures for rechargeable lithium-air batteries, Energy & Environmental Science 2015, 8, 2144.

[77]M. Park, H. Sun, H. Lee, J. Lee, J. Cho, Lithium-Air Batteries: Survey on the Current Status and Perspectives Towards Automotive Applications from a Battery Industry Standpoint, Advanced Energy Materials 2012, 2, 780.

[78]H. He, W. Niu, N. M. Asl, J. Salim, R. Chen, Y. Kim, Effects of aqueous electrolytes on the voltage behaviors of rechargeable Li-air batteries, Electrochimica Acta 2012, 67, 87.

[79]Y. Wang, H. Zhou, A lithium-air battery with a potential to continuously reduce O_2 from air for delivering energy, Journal of Power Sources 2010, 195, 358.

[80]S. Hasegawa, N. Imanishi, T. Zhang, J. Xie, A. Hirano, Y. Takeda, O. Yamamoto, Study on lithium/air secondary batteries-Stability of NASICON-type lithium ion conducting glass-ceramics with water, Journal of Power Sources 2009, 189, 371.

[81]C. O. Laoire, S. Mukerjee, K. Abraham, E. J. Plichta, M. A. Hendrickson, Influence of nonaqueous solvents on the electrochemistry of oxygen in the rechargeable lithium-air battery, The Journal of Physical Chemistry C 2010, 114, 9178.

[82]J. Wang, Y. Li, X. Sun, Challenges and opportunities of nanostructured materials for aprotic rechargeable lithium-air batteries, Nano Energy 2013, 2, 443.

[83]Y. Shao, S. Park, J. Xiao, J. G. Zhang, Y. Wang, J. Liu, Electrocatalysts for Nonaqueous Lithium-Air Batteries: Status, Challenges, and Perspective, ACS Catalysis 2012, 2, 844.

[84]J. Liu, Charging graphene for energy, Nature Nanotechnology 2014, 9, 739.

[85]Y. Sun, Q. Wu, G. Shi, Graphene based new energy materials, Energy & Environmental Science 2011, 4, 1113.

[86]Y. Li, J. Wang, X. Li, D. Geng, R. Li, X. Sun, Superior energy capacity of graphene nanosheets for a nonaqueous lithium-oxygen battery, Chemical Communications 2011, 47, 9438.

[87]J. Xiao, D. H. Mei, X. L. Li, W. Xu, D. Wang, G. L. Graff, W. D. Bennett, Z. M. Nie, L. V. Saraf, I. A. Aksay, J. Liu, J. G. Zhang, Hierarchically Porous Graphene as a Lithium-Air Battery Electrode, Nano Letters 2011, 11, 5071.

[88]Y. Li, J. Wang, X. Li, D. Geng, M. N. Banis, Y. Tang, D. Wang, R. Li, T.-K. Sham, X. Sun, Discharge product morphology and increased charge performance of lithium-oxygen batteries with graphene nanosheet electrodes: the effect of sulphur doping, Journal of Materials Chemistry 2012, 22, 20170.

[89]H.-G. Jung, Y. S. Jeong, J.-B. Park, Y.-K. Sun, B. Scrosati, Y. J. Lee, Ruthenium-Based Electrocatalysts Supported on Reduced Graphene Oxide for Lithium-Air Batteries, ACS Nano 2013, 7, 3532.

[90]Y. Cao, Z. Wei, J. He, J. Zang, Q. Zhang, M. Zheng, Q. Dong, α-MnO_2 nanorods grown in situ on graphene as catalysts for Li-O_2 batteries with excellent electrochemical performance, Energy & Environmental Science 2012, 5, 9765.

[91]W. H. Ryu, T. H. Yoon, S. H. Song, S. Jeon, Y. J. Park, I. D. Kim, Bifunctional composite catalysts using Co_3O_4 nanofibers immobilized on nonoxidized graphene nanoflakes for high-capacity and long-cycle Li-O_2 batteries, Nano Letters 2013, 13, 4190.

[92]T. H. Yoon, Y. J. Park, Carbon nanotube/Co_3O_4 composite for air electrode of lithium-air battery, Nanoscale Research Letters 2012, 7, 1.

[93]Y. Shen, D. Sun, L. Yu, W. Zhang, Y. Shang, H. Tang, J. Wu, A. Cao, Y. Huang, A high-capacity lithium-air battery with Pd modified carbon nanotube sponge cathode working in regular air, Carbon 2013, 62, 288.

[94]H. D. Lim, K. Y. Park, H. Song, E. Y. Jang, H. Gwon, J. Kim, Y. H. Kim, M. D. Lima, R. O. Robles, X. Lepró, Enhanced Power and Rechargeability of a Li-O_2 Battery Based on a Hierarchical-Fibril CNT Electrode, Advanced Materials 2013, 25, 1348.

[95]R. R. Mitchell, B. M. Gallant, C. V. Thompson, Y. Shao-Horn, All-carbon-nanofiber electrodes for high-energy rechargeable Li-O_2 batteries, Energy & Environmental Science 2011, 4, 2952.

[96]J. L. Shui, F. Du, C. Xue, Q. Li, L. Dai, Vertically Aligned N-doped Coral-like Carbon Fiber Arrays as Efficient Air Electrodes for High-Performance Nonaqueous Li-O_2 Batteries, ACS Nano 2014, 8, 3015.

[97]H.-D. Lim, H. Song, H. Gwon, K.-Y. Park, J. Kim, Y. Bae, H. Kim, S.-K. Jung, T. Kim, Y. H. Kim, X. Lepró, R. Ovalle-Robles, R. H. Baughman, K. Kang, A new catalyst-embedded hierarchical air electrode for high-performance Li-O_2 batteries, Energy & Environmental Science 2013, 6, 3570.

[98]H. W. Park, D. U. Lee, M. G. Park, R. Ahmed, M. H. Seo, L. F. Nazar, Z. Chen, Perovskite-Nitrogen-Doped Carbon Nanotube Composite as Bifunctional Catalysts for Rechargeable Lithium-Air Batteries, ChemSusChem 2015.

[99]Y. J. Kim, H. Lee, D. J. Lee, J. K. Park, H. T. Kim, Reduction of Charge and Discharge Polarization by Cobalt Nanoparticles-Embedded Carbon Nanofibers for Li-O_2 Batteries, ChemSusChem 2015, 8, 2496.

[100] L. Li, S. Liu, A. Manthiram, Co_3O_4 nanocrystals coupled with O- and N-doped carbon nanoweb as a synergistic catalyst for hybrid Li-air batteries, Nano Energy 2014.

[101] J. L. Shui, N. K. Karan, M. Balasubramanian, S. Y. Li, D. J. Liu, Fe/N/C Composite in Li-O_2 Battery: Studies of Catalytic Structure and Activity toward Oxygen Evolution Reaction, Journal of the American Chemical Society 2012, 134, 16654.

[102] X. Ren, S. S. Zhang, D. T. Tran, J. Read, Oxygen reduction reaction catalyst on lithium/air battery discharge performance, Journal of Materials Chemistry 2011, 21, 10118.

[103] J. J. Xu, Z. L. Wang, D. Xu, L. L. Zhang, X. B. Zhang, Tailoring deposition and morphology of discharge products towards high-rate and long-life lithium-oxygen batteries, Nature Communications 2013, 4, 2438.

[104] Y. S. Jeong, J. B. Park, H. G. Jung, J. Kim, X. Luo, J. Lu, L. Curtiss, K. Amine, Y. K. Sun, B. Scrosati, Y. J. Lee, Study on the Catalytic Activity of Noble Metal Nanoparticles on Reduced Graphene Oxide for Oxygen Evolution Reactions in Lithium-Air Batteries, Nano Letters 2015.

[105] Y. C. Lu, H. A. Gasteiger, Y. Shao-Horn, Catalytic activity trends of oxygen reduction reaction for nonaqueous Li-air batteries, Journal of the American Chemical Society 2011, 133, 19048.

[106] J. Yin, B. Fang, J. Luo, B. Wanjala, D. Mott, R. Loukrakpam, M. S. Ng, Z. Li, J. Hong, M. S. Whittingham, C. J. Zhong, Nanoscale alloying effect of gold-platinum nanoparticles as cathode catalysts on the performance of a rechargeable lithium-oxygen battery, Nanotechnology 2012, 23.

[107] B. G. Kim, H.-J. Kim, S. Back, K. W. Nam, Y. Jung, Y.-K. Han, J. W. Choi, Improved reversibility in lithium-oxygen battery: Understanding elementary reactions and surface charge engineering of metal alloy catalyst, Scientific Reports 2014, 4, 4225.

[108] M. H. Lu, D. Y. Chen, C. H. Xu, Y. Zhan, J. Y. Lee, Enhancing the performance of catalytic AuPt nanoparticles in nonaqueous lithium-oxygen batteries, Nanoscale 2015, 7, 12906.

[109] Z. M. Cui, L. J. Li, A. Manthiram, J. B. Goodenough, Enhanced Cycling Stability of Hybrid Li-Air Batteries Enabled by Ordered PdFe Intermetallic Electrocatalyst, Journal of the American Chemical Society 2015.

[110] R. Choi, J. Jung, G. Kim, K. Song, Y.-I. Kim, S. C. Jung, Y.-K. Han, H. Song, Y.-M. Kang, Ultra-low overpotential and high rate capability in Li-O_2 batteries through

surface atom arrangement of PdCu nanocatalysts, Energy & Environmental Science 2014, 7, 1362.

[111] A. Debart, A. J. Paterson, J. Bao, P. G. Bruce, α-MnO_2 Nanowires: A Catalyst for the O_2 Electrode in Rechargeable Lithium Batteries, Angewandte Chemie International Edition 2008, 47, 4521.

[112] A. Débart, J. Bao, G. Armstrong, P. G. Bruce, An O_2 cathode for rechargeable lithium batteries: the effect of a catalyst, Journal of Power Sources 2007, 174, 1177.

[113] F. Wu, X. X. Zhang, T. L. Zhao, R. J. Chen, Y. S. Ye, M. Xie, L. Li, Hierarchical mesoporous/macroporous Co_3O_4 ultrathin nanosheets as free-standing catalysts for rechargeable lithium-oxygen batteries, Journal of Materials Chemistry A 2015, 3, 17620.

[114] J. K. Zhang, P. F. Li, Z. H. Wang, J. S. Qiao, D. Rooney, W. Sun, K. N. Sun, Three-dimensional graphene-Co_3O_4 cathodes for rechargeable Li-O_2 batteries, Journal of Materials Chemistry A 2015, 3, 1504.

[115] Z. Jian, P. Liu, F. Li, P. He, X. Guo, M. Chen, H. Zhou, Core-shell-structured CNT@RuO_2 composite as a high-performance cathode catalyst for rechargeable Li-O_2 batteries, Angewandte Chemie International Edition 2014, 53, 442.

[116] P. Tan, W. Shyy, T. S. Zhao, X. B. Zhu, Z. H. Wei, A RuO_2 nanoparticle-decorated buckypaper cathode for non-aqueous lithium-oxygen batteries, Journal of Materials Chemistry A 2015.

[117] Y. Lee, J. Suntivich, K. J. May, E. E. Perry, Y. Shao-Horn, Synthesis and activities of rutile IrO_2 and RuO_2 nanoparticles for oxygen evolution in acid and alkaline solutions, The Journal of Physical Chemistry Letters 2012, 3, 399.

[118] K. Guo, Y. Li, T. Yuan, X. W. Dong, X. W. Li, H. Yang, Ultrafine IrO_2 nanoparticle-decorated carbon as an electrocatalyst for rechargeable Li-O_2 batteries with

enhanced charge performance and cyclability, Journal of Solid State Electrochemistry 2015, 19, 821.

[119] J. J. Xu, D. Xu, Z. L. Wang, H. G. Wang, L. L. Zhang, X. B. Zhang, Synthesis of perovskite-based porous $La_{0.75}Sr_{0.25}MnO_3$ nanotubes as a highly efficient electrocatalyst for rechargeable lithium-oxygen batteries, Angewandte Chemie International Edition 2013, 52, 3887.

[120] Z. H. Wei, T. S. Zhao, X. B. Zhu, L. An, P. Tan, Integrated Porous Cathode made of Pure Perovskite Lanthanum Nickel Oxide for Nonaqueous Lithium-Oxygen Batteries, Energy Technology 2015, 3, 1093.

[121] D. W. Zhang, Y. F. Song, Z. Z. Du, L. Wang, Y. T. Li, J. B. Goodenough, Active $LaNi_{1-x}Fe_xO_3$ bifunctional catalysts for air cathodes in alkaline media, Journal of Materials Chemistry A 2015, 3, 9421.

[122] J. Hassoun, H. G. Jung, D. J. Lee, J. B. Park, K. Amine, Y. K. Sun, B. Scrosati, A metal-free, lithium-ion oxygen battery: a step forward to safety in lithium-air batteries, Nano Letters 2012, 12, 5775.

[123] Z. Y. Guo, X. L. Dong, Y. G. Wang, Y. Y. Xia, A lithium air battery with a lithiated Al-carbon anode, Chemical Communications 2015, 51, 676.

[124] Q. C. Liu, J. J. Xu, S. Yuan, Z. W. Chang, D. Xu, Y. B. Yin, L. Li, H. X. Zhong, Y. S. Jiang, J. M. Yan, X. B. Zhang, Artificial Protection Film on Lithium Metal Anode toward Long-Cycle-Life Lithium-Oxygen Batteries, Advanced Materials 2015, 27, 5241.

[125] G. Y. Aleshin, D. A. Semenenko, A. I. Belova, T. K. Zakharchenko, D. M. Itkis, E. A. Goodilin, Y. D. Tretyakov, Protected anodes for lithium-air batteries, Solid State Ionics 2011, 184, 62.

[126] D. J. Lee, H. Lee, J. Song, M.-H. Ryou, Y. M. Lee, H.-T. Kim, J.-K. Park, Composite protective layer for Li metal anode in high-performance lithium-oxygen batteries, Electrochemistry Communications 2014, 40, 45.

[127] Y. Y. Shao, F. Ding, J. Xiao, J. Zhang, W. Xu, S. Park, J. G. Zhang, Y. Wang, J. Liu, Making Li-Air Batteries Rechargeable: Material Challenges, Advanced Functional Materials 2013, 23, 987.

[128] Z. Ma, X. X. Yuan, L. Li, Z. F. Ma, D. P. Wilkinson, L. Zhang, J. J. Zhang, A review of cathode materials and structures for rechargeable lithium-air batteries, Energy & Environmental Science 2015, 8, 2144.

[129] W. Xu, V. V. Viswanathan, D. Wang, S. A. Towne, J. Xiao, Z. M. Nie, D. H. Hu, J. G. Zhang, Investigation on the charging process of Li_2O_2-based air electrodes in Li-O_2 batteries with organic carbonate electrolytes, Journal of Power Sources 2011, 196, 3894.

[130] S. A. Freunberger, Y. H. Chen, Z. Q. Peng, J. M. Griffin, L. J. Hardwick, F. Bardé, P. Novák, P. G. Bruce, Reactions in the rechargeable lithium-O_2 battery with alkyl carbonate electrolytes, Journal of the American Chemical Society 2011, 133, 8040.

[131] S. A. Freunberger, Y. Chen, N. E. Drewett, L. J. Hardwick, F. Bardé, P. G. Bruce, The Lithium-Oxygen Battery with Ether-Based Electrolytes, Angewandte Chemie International Edition 2011, 50, 8609.

[132] R. S. Assary, J. Lu, P. Du, X. Luo, X. Zhang, Y. Ren, L. A. Curtiss, K. Amine, The Effect of Oxygen Crossover on the Anode of a Li-O_2 Battery using an Ether-Based Solvent: Insights from Experimental and Computational Studies, ChemSusChem 2013, 6, 51.

[133] B. D. McCloskey, A. Valery, A. C. Luntz, S. R. Gowda, G. M. Wallraff, J. M. Garcia, T. Mori, L. E. Krupp, Combining accurate O_2 and Li_2O_2 assays to separate

discharge and charge stability limitations in nonaqueous Li-O_2 batteries, The Journal of Physical Chemistry Letters 2013, 4, 2989.

[134] D. Xu, Z. L. Wang, J. J. Xu, L. L. Zhang, L. M. Wang, X. B. Zhang, A stable sulfone based electrolyte for high performance rechargeable Li-O_2 batteries, Chemical Communications 2012, 48, 11674.

[135] Y. H. Chen, S. A. Freunberger, Z. Q. Peng, F. Bardé, P. G. Bruce, Li-O_2 battery with a dimethylformamide electrolyte, Journal of the American Chemical Society 2012, 134, 7952.

[136] W. Walker, V. Giordani, J. Uddin, V. S. Bryantsev, G. V. Chase, D. Addison, A rechargeable Li-O_2 battery using a lithium nitrate/N, N-dimethylacetamide electrolyte, Journal of the American Chemical Society 2013, 135, 2076.

[137] D. Zhang, R. S. Li, T. Huang, A. S. Yu, Novel composite polymer electrolyte for lithium air batteries, Journal of Power Sources 2010, 195, 1202.

[138] T. Zhang, H. S. Zhou, From Li-O_2 to Li-air batteries: carbon nanotubes/ionic liquid gels with a tricontinuous passage of electrons, ions, and oxygen, Angewandte Chemie International Edition 2012, 124, 11224.

[139] A. V. Murugan, T. Muraliganth, A. Manthiram, One-pot microwave-hydrothermal synthesis and characterization of carbon-coated $LiMPO_4$ (M= Mn, Fe, and Co) cathodes, Journal of The Electrochemical Society 2009, 156, A79.

[140] J. S. Wang, K. Matyjaszewski, Controlled/"living" radical polymerization. atom transfer radical polymerization in the presence of transition-metal complexes, Journal of the American Chemical Society 1995, 117, 5614.

[141] R. M. d. Carvalho, J. C. Pereira, M. Yoshiyama, D. H. Pashley, A review of polymerization contraction: The influence of stress development versus stress relief, Operative Dentistry 1995, 21, 17.

[142] E. Vivaldo Lima, P. E. Wood, A. E. Hamielec, A. Penlidis, An updated review on suspension polymerization, Industrial & Engineering Chemistry Research 1997, 36, 939.

[143] J. M. G. Cowie, *Polymers: Chemistry and Physics of Modern Materials*, Chapman and Hall, 1991.

[144] G. D. Du, Nanostructured anode materials for lithium-ion batteries, University of Wollongong Thesis Collection, 2011.

[145] M. J. Lindsay, Data analysis and anode materials for lithium ion batteries, University of Wollongong Thesis Collection, 2004.

[146] A. S. Arico, P. Bruce, B. Scrosati, J.-M. Tarascon, W. van Schalkwijk, Nanostructured materials for advanced energy conversion and storage devices, Nature Materials 2005, 4, 366.

[147] D. W. Liu, G. Z. Cao, Engineering nanostructured electrodes and fabrication of film electrodes for efficient lithium ion intercalation, Energy & Environmental Science 2010, 3, 1218.

[148] J. Z. Wang, L. Lu, M. Lotya, J. N. Coleman, S. L. Chou, H. K. Liu, A. I. Minett, J. Chen, Development of MoS_2-CNT Composite Thin Film from Layered MoS_2 for Lithium Batteries, Advanced Energy Materials 2013, 3, 798.

[149] L. B. Hu, Y. Cui, Energy and environmental nanotechnology in conductive paper and textiles, Energy & Environmental Science 2012, 5, 6423.

[150] X. L. Jia, Z. Chen, A. Suwarnasarn, L. Rice, X. L. Wang, H. Sohn, Q. Zhang, B. M. Wu, F. Wei, Y. F. Lu, High-performance flexible lithium-ion electrodes based on robust network architecture, Energy & Environmental Science 2012, 5, 6845.

[151] L. Noerochim, J. Z. Wang, D. Wexler, M. M. Rahman, J. Chen, H. K. Liu, Impact of mechanical bending on the electrochemical performance of bendable lithium

batteries with paper-like free-standing V_2O_5-polypyrrole cathodes, Journal of Materials Chemistry 2012, 22, 11159.

[152] J. Z. Wang, S. L. Chou, J. Chen, S. Y. Chew, G. X. Wang, K. Konstantinov, J. Wu, S. X. Dou, H. K. Liu, Paper-like free-standing polypyrrole and polypyrrole-$LiFePO_4$ composite films for flexible and bendable rechargeable battery, Electrochemistry Communications 2008, 10, 1781.

[153] C. M. Schauerman, M. J. Ganter, G. Gaustad, C. W. Babbitt, R. P. Raffaelle, B. J. Landi, Recycling single-wall carbon nanotube anodes from lithium ion batteries, Journal of Materials Chemistry 2012, 22, 12008.

[154] S. H. Ng, J. Z. Wang, Z. P. Guo, J. Chen, G. X. Wang, H. K. Liu, Single wall carbon nanotube paper as anode for lithium-ion battery, Electrochimica Acta 2005, 51, 23.

[155] B. J. Landi, M. J. Ganter, C. D. Cress, R. A. DiLeo, R. P. Raffaelle, Carbon nanotubes for lithium ion batteries, Energy & Environmental Science 2009, 2, 638.

[156] J. Wang, L. L. Li, C. L. Wong, S. Madhavi, Flexible single-walled carbon nanotube/polycellulose papers for lithium-ion batteries, Nanotechnology 2012, 23, 495401.

[157] S. L. Chou, Y. Zhao, J. Z. Wang, Z. X. Chen, H. K. Liu, S. X. Dou, Silicon/Single-Walled Carbon Nanotube Composite Paper as a Flexible Anode Material for Lithium Ion Batteries, The Journal of Physical Chemistry C 2010, 114, 15862.

[158] K. Fu, O. Yildiz, H. Bhanushali, Y. X. Wang, K. Stano, L. G. Xue, X. W. Zhang, P. D. Bradford, Aligned Carbon Nanotube-Silicon Sheets: A Novel Nano-architecture for Flexible Lithium Ion Battery Electrodes, Advanced Materials 2013, 25, 5109.

[159] G. M. Zhou, D. W. Wang, P. X. Hou, W. S. Li, N. Li, C. Liu, F. Li, H. M. Cheng, A nanosized Fe_2O_3 decorated single-walled carbon nanotube membrane as a high-

performance flexible anode for lithium ion batteries, Journal of Materials Chemistry 2012, 22, 17942.

[160] Z. Y. Cao, B. Q. Wei, α-Fe_2O_3/single-walled carbon nanotube hybrid films as high-performance anodes for rechargeable lithium-ion batteries, Journal of Power Sources 2013, 241, 330.

[161] L. Noerochim, J. Z. Wang, S. L. Chou, D. Wexler, H. K. Liu, Free-standing single-walled carbon nanotube/SnO_2 anode paper for flexible lithium-ion batteries, Carbon 2012, 50, 1289.

[162] J. W. Qin, Q. Zhang, Z. Y. Cao, X. Li, C. W. Hu, B. Q. Wei, MnO_x/SWCNT macro-films as flexible binder-free anodes for high-performance Li-ion batteries, Nano Energy 2013, 2, 733.

[163] K. H. Seng, M.-H. Park, Z. P. Guo, H. K. Liu, J. Cho, Self-Assembled Germanium/Carbon Nanostructures as High-Power Anode Material for the Lithium-Ion Battery, Angewandte Chemie International Edition 2012, 51, 5657.

[164] G. Jo, I. Choi, H. Ahn, M. J. Park, Binder-free Ge nanoparticles-carbon hybrids for anode materials of advanced lithium batteries with high capacity and rate capability, Chemical Communications 2012, 48, 3987.

[165] R. A. DiLeo, M. J. Ganter, B. J. Landi, R. P. Raffaelle, Germanium-single-wall carbon nanotube anodes for lithium ion batteries, Journal of Materials Research 2010, 25, 1441.

[166] J.-Y. Eom, H.-S. Kwon, Effects of the chemical etching of single-walled carbon nanotubes on their lithium storage properties, Materials Chemistry and Physics 2011, 126, 108.

[167] H. S. Oktaviano, K. Yamada, K. Waki, Nano-drilled multiwalled carbon nanotubes: characterizations and application for LIB anode materials, Journal of Materials Chemistry 2012, 22, 25167.

[168] W. X. Chen, J. Y. Lee, Z. Liu, The nanocomposites of carbon nanotube with Sb and $SnSb_{0.5}$ as Li-ion battery anodes, Carbon 2003, 41, 959.

[169] A. M. Chockla, M. G. Panthani, V. C. Holmberg, C. M. Hessel, D. K. Reid, T. D. Bogart, J. T. Harris, C. B. Mullins, B. A. Korgel, Electrochemical Lithiation of Graphene-Supported Silicon and Germanium for Rechargeable Batteries, The Journal of Physical Chemistry C 2012, 116, 11917.

[170] C. Zhong, J. Z. Wang, X. W. Gao, D. Wexler, H. K. Liu, In situ one-step synthesis of a 3D nanostructured germanium-graphene composite and its application in lithium-ion batteries, Journal of Materials Chemistry A 2013, 1, 10798.

[171] S. Yoon, C.-M. Park, H.-J. Sohn, Electrochemical Characterizations of Germanium and Carbon-Coated Germanium Composite Anode for Lithium-Ion Batteries, Electrochemical and Solid-State Letters 2008, 11, A42.

[172] Z. J. Zhang, J. Z. Wang, S. L. Chou, H. K. Liu, K. Ozawa, H. J. Li, Polypyrrole-coated α-$LiFeO_2$ nanocomposite with enhanced electrochemical properties for lithium-ion batteries, Electrochimica Acta 2013, 108, 820.

[173] X. W. Gao, J. Z. Wang, S. L. Chou, H. K. Liu, Synthesis and electrochemical performance of LiV_3O_8/polyaniline as cathode material for the lithium battery, Journal of Power Sources 2012, 220, 47.

[174] M. Armand, J.-M. Tarascon, Building better batteries, Nature 2008, 451, 652.

[175] P. G. Bruce, B. Scrosati, J.-M. Tarascon, Nanomaterials for Rechargeable Lithium Batteries, Angewandte Chemie International Edition 2008, 47, 2930.

[176] H. Li, Z. Wang, L. Chen, X. Huang, Research on Advanced Materials for Li-ion Batteries, Advanced Materials 2009, 21, 4593.

[177] L. P. Tan, Z. Y. Lu, H. T. Tan, J. X. Zhu, X. H. Rui, Q. Y. Yan, H. H. Hng, Germanium nanowires-based carbon composite as anodes for lithium-ion batteries, Journal of Power Sources 2012, 206, 253.

[178] C. K. Chan, X. F. Zhang, Y. Cui, High Capacity Li Ion Battery Anodes Using Ge Nanowires, Nano Letters 2008, 8, 307.

[179] I.-S. Hwang, J.-C. Kim, S.-D. Seo, S. Lee, J.-H. Lee, D.-W. Kim, A binder-free Ge-nanoparticle anode assembled on multiwalled carbon nanotube networks for Li-ion batteries, Chemical Communications 2012, 48, 7061.

[180] L. C. Yang, Q. S. Gao, L. Li, Y. Tang, Y. P. Wu, Mesoporous germanium as anode material of high capacity and good cycling prepared by a mechanochemical reaction, Electrochemistry Communications 2010, 12, 418.

[181] C. H. Kim, Y. S. Jung, K. T. Lee, J. H. Ku, S. M. Oh, The role of in situ generated nano-sized metal particles on the coulombic efficiency of $MGeO_3$ (M = Cu, Fe, and Co) electrodes, Electrochimica Acta 2009, 54, 4371.

[182] J. K. Feng, M. O. Lai, L. Lu, Zn_2GeO_4 Nanorods synthesized by low-temperature hydrothermal growth for high-capacity anode of lithium battery, Electrochemistry Communications 2011, 13, 287.

[183] Q. M. Pan, Z. J. Wang, J. Liu, G. P. Yin, M. Gu, PbO@C core-shell nanocomposites as an anode material of lithium-ion batteries, Electrochemistry Communications 2009, 11, 917.

[184] J. Shu, R. Ma, L. Y. Shao, M. Shui, D. J. Wang, K. G. Wu, N. B. Long, Y. L. Ren, Hydrothermal fabrication of lead hydroxide chloride as a novel anode material for lithium-ion batteries, Electrochimica Acta 2013, 102, 381.

[185] J. K. Feng, L. J. Ci, Y. X. Qi, N. Lun, S. L. Xiong, Y. T. Qian, Low temperature synthesis of lead germanate ($PbGeO_3$)/polypyrrole (PPy) nanocomposites and their lithium storage performance, Materials Research Bulletin 2014, 57, 238.

[186] H. Kim, K. Y. Park, J. Hong, K. Kang, All-graphene-battery: bridging the gap between supercapacitors and lithium ion batteries, Scientific Reports 2014, 4, 5278.

[187] C. Zhong, J. Z. Wang, D. Wexler, H. K. Liu, Microwave autoclave synthesized multi-layer graphene/single-walled carbon nanotube composites for free-standing lithium-ion battery anodes, Carbon 2014, 66, 637.

[188] J. Zhu, G. H. Zhang, X. Z. Yu, Q. H. Li, B. G. Lu, Z. Xu, Graphene double protection strategy to improve the SnO_2 electrode performance anodes for lithium-ion batteries, Nano Energy 2014, 3, 80.

[189] Y. X. Wang, Y.-G. Lim, M.-S. Park, S. L. Chou, J. H. Kim, H. K. Liu, S. X. Dou, Y.-J. Kim, Ultrafine SnO_2 nanoparticle loading onto reduced graphene oxide as anodes for sodium-ion batteries with superior rate and cycling performances, Journal of Materials Chemistry A 2014, 2, 529.

[190] B. H. Zhang, Y. Liu, Z. Chang, Y. Q. Yang, Z. B. Wen, Y. P. Wu, R. Holze, Nanowire $Na_{0.35}MnO_2$ from a hydrothermal method as a cathode material for aqueous asymmetric supercapacitors, Journal of Power Sources 2014, 253, 98.

[191] B. H. Zhang, Y. Liu, Z. Chang, Y. Q. Yang, Z. B. Wen, Y. P. Wu, Nanowire $K_{0.19}MnO_2$ from hydrothermal method as cathode material for aqueous supercapacitors of high energy density, Electrochimica Acta 2014, 130, 693.

[192] L. J. Cote, F. Kim, J. X. Huang, Langmuir-Blodgett Assembly of Graphite Oxide Single Layers, Journal of the American Chemical Society 2009, 131, 1043.

[193] H. L. Guo, X. F. Wang, Q. Y. Qian, F. B. Wang, X. H. Xia, A Green Approach to the Synthesis of Graphene Nanosheets, ACS Nano 2009, 3, 2653.

[194] Y. Shi, S.-L. Chou, J.-Z. Wang, H.-J. Li, H.-K. Liu, Y.-P. Wu, In-situ hydrothermal synthesis of graphene woven VO_2 nanoribbons with improved cycling performance, Journal of Power Sources 2013, 244, 684.

[195] J. S. Zhou, H. H. Song, L. L. Ma, X. H. Chen, Magnetite/graphene nanosheet composites: interfacial interaction and its impact on the durable high-rate performance in lithium-ion batteries, RSC Advances 2011, 1, 782.

[196] K. Karthikeyan, D. Kalpana, S. Amaresh, Y. S. Lee, Microwave synthesis of graphene/magnetite composite electrode material for symmetric supercapacitor with superior rate performance, RSC Advances 2012, 2, 12322.

[197] S. H. Ng, J. Z. Wang, K. Konstantinov, D. Wexler, J. Chen, H. K. Liu, Spray Pyrolyzed PbO-Carbon Nanocomposites as Anode for Lithium-Ion Batteries, Journal of The Electrochemical Society 2006, 153, A787.

[198] K. H. Seng, M.-h. Park, Z. P. Guo, H. K. Liu, J. Cho, Catalytic Role of Ge in Highly Reversible GeO_2/Ge/C Nanocomposite Anode Material for Lithium Batteries, Nano Letters 2013, 13, 1230.

[199] W. W. Li, X. F. Wang, B. Liu, J. Xu, B. Liang, T. Luo, S. J. Luo, D. Chen, G. Z. Shen, Single-crystalline metal germanate nanowire-carbon textiles as binder-free, self-supported anodes for high-performance lithium storage, Nanoscale 2013, 5, 10291.

[200] Z. Y. Yuan, Z. B. Peng, Y. D. Chen, H. W. Liu, Synthesis and electrochemical performance of nanosized tin lead composite oxides as lithium storage materials, Materials Chemistry and Physics 2010, 120, 331.

[201] L. L. Garza Tovar, P. A. Connor, F. Belliard, L. M. Torres-Martínez, J. T. S. Irvine, Investigation of lead tin fluorides as possible negative electrodes for Li-ion batteries, Journal of Power Sources 2001, 97-98, 258.

[202] M. Martos, J. Morales, L. Sánchez, Lead-based systems as suitable anode materials for Li-ion batteries, Electrochimica Acta 2003, 48, 615.

[203] S. L. Chou, J. Z. Wang, D. Wexler, K. Konstantinov, C. Zhong, H. K. Liu, S. X. Dou, High-surface-area α-Fe_2O_3/carbon nanocomposite: one-step synthesis and its highly reversible and enhanced high-rate lithium storage properties, Journal of Materials Chemistry 2010, 20, 2092.

[204] X. W. Gao, C. Q. Feng, S. L. Chou, J. Z. Wang, J. Z. Sun, M. Forsyth, D. R. MacFarlane, H. K. Liu, $LiNi_{0.5}Mn_{1.5}O_4$ spinel cathode using room temperature ionic liquid as electrolyte, Electrochimica Acta 2013, 101, 151.

[205] Z. J. Zhang, Q. Y. Zeng, S. L. Chou, X. J. Li, H. J. Li, K. Ozawa, H. K. Liu, J. Z. Wang, Tuning three-dimensional TiO_2 nanotube electrode to achieve high utilization of Ti substrate for lithium storage, Electrochimica Acta 2014, 133, 570.

[206] M. M. Ottakam Thotiyl, S. A. Freunberger, Z. Q. Peng, Y. H. Chen, Z. Liu, P. G. Bruce, A stable cathode for the aprotic Li-O_2 battery, Nature Materials 2013, 12, 1050.

[207] Q. C. Liu, J. J. Xu, D. Xu, X. B. Zhang, Flexible lithium-oxygen battery based on a recoverable cathode, Nature Communications 2015, 6, 7892.

[208] Z. Q. Peng, S. A. Freunberger, Y. H. Chen, P. G. Bruce, A Reversible and Higher-Rate Li-O_2 Battery, Science 2012, 337, 563.

[209] P. G. Bruce, S. A. Freunberger, L. J. Hardwick, J. M. Tarascon, Li-O_2 and Li-S batteries with high energy storage, Nature Materials 2012, 11, 19.

[210] L. Grande, E. Paillard, J. Hassoun, J. B. Park, Y. J. Lee, Y. K. Sun, S. Passerini, B. Scrosati, The lithium/air battery: still an emerging system or a practical reality?, Advanced Materials 2015, 27, 784.

[211] H. L. Wang, L. F. Cui, Y. Yang, H. Sanchez Casalongue, J. T. Robinson, Y. Y. Liang, Y. Cui, H. J. Dai, Mn_3O_4-Graphene Hybrid as a High-Capacity Anode Material for Lithium Ion Batteries, Journal of the American Chemical Society 2010, 132, 13978.

[212] Z. J. Fan, J. Yan, T. Wei, L. J. Zhi, G. Q. Ning, T. Y. Li, F. Wei, Asymmetric Supercapacitors Based on Graphene/MnO_2 and Activated Carbon Nanofiber Electrodes with High Power and Energy Density, Advanced Functional Materials 2011, 21, 2366.

[213] X. F. Hu, X. P. Han, Y. X. Hu, F. Y. Cheng, J. Chen, ε-MnO_2 nanostructures directly grown on Ni foam: a cathode catalyst for rechargeable Li-O_2 batteries, Nanoscale 2014, 6, 3522.

[214] P. Zhang, D. F. Sun, M. He, J. W. Lang, S. Xu, X. B. Yan, Synthesis of Porous δ-MnO_2 Submicron Tubes as Highly Efficient Electrocatalyst for Rechargeable Li-O_2 Batteries, ChemSusChem 2015, 8, 1972.

[215] S. Stankovich, D. A. Dikin, G. H. B. Dommett, K. M. Kohlhaas, E. J. Zimney, E. A. Stach, R. D. Piner, S. T. Nguyen, R. S. Ruoff, Graphene-based composite materials, Nature 2006, 442, 282.

[216] K. P. Loh, Q. L. Bao, P. K. Ang, J. X. Yang, The chemistry of graphene, Journal of Materials Chemistry 2010, 20, 2277.

[217] C. G. Liu, Z. N. Yu, D. Neff, A. Zhamu, B. Z. Jang, Graphene-Based Supercapacitor with an Ultrahigh Energy Density, Nano Letters 2010, 10, 4863.

[218] J. Wang, C. Q. Feng, Z. Q. Sun, S. L. Chou, H. K. Liu, J. Z. Wang, In-situ One-step Hydrothermal Synthesis of a Lead Germanate-Graphene Composite as a Novel Anode Material for Lithium-Ion Batteries, Scientific Reports 2014, 4, 7030.

[219] J. B. Hou, Y. Y. Shao, M. W. Ellis, R. B. Moore, B. L. Yi, Graphene-based electrochemical energy conversion and storage: fuel cells, supercapacitors and lithium ion batteries, Physical Chemistry Chemical Physics 2011, 13, 15384.

[220] B. Sun, B. Wang, D. W. Su, L. D. Xiao, H. Ahn, G. X. Wang, Graphene nanosheets as cathode catalysts for lithium-air batteries with an enhanced electrochemical performance, Carbon 2012, 50, 727.

[221] G. Wu, N. H. Mack, W. Gao, S. G. Ma, R. Q. Zhong, J. T. Han, J. K. Baldwin, P. Zelenay, Nitrogen-Doped Graphene-Rich Catalysts Derived from Heteroatom Polymers for Oxygen Reduction in Nonaqueous Lithium-O_2 Battery Cathodes, ACS Nano 2012, 6, 9764.

[222] T. T. Lee, J. R. Hong, W. C. Lin, C. C. Hu, P. W. Wu, Y. Y. Li, Synthesis of Petal-Like Carbon Nanocapsule@MnO_2 Core-Shell Particles and Their Application in Supercapacitors, Journal of The Electrochemical Society 2014, 161, H598.

[223] C. Z. Yang, M. Zhou, Q. Xu, Three-dimensional ordered macroporous MnO_2/carbon nanocomposites as high-performance electrodes for asymmetric supercapacitors, Physical Chemistry Chemical Physics 2013, 15, 19730.

[224] Y. X. Wang, L. Huang, L. C. Sun, S. Y. Xie, G. L. Xu, S. R. Chen, Y. F. Xu, J. T. Li, S. L. Chou, S. X. Dou, S. G. Sun, Facile synthesis of a interleaved expanded graphite-embedded sulphur nanocomposite as cathode of Li-S batteries with excellent lithium storage performance, Journal of Materials Chemistry 2012, 22, 4744.

[225] Y. X. Wang, S. L. Chou, H. K. Liu, S. X. Dou, Reduced graphene oxide with superior cycling stability and rate capability for sodium storage, Carbon 2013, 57, 202.

[226] Y. Shi, S. L. Chou, J. Z. Wang, H. J. Li, H. K. Liu, Y. P. Wu, In-situ hydrothermal synthesis of graphene woven VO_2 nanoribbons with improved cycling performance, J. Power Sources 2013, 244, 684.

[227] Y. J. Zhang, K. Fugane, T. Mori, L. Niu, J. H. Ye, Wet chemical synthesis of nitrogen-doped graphene towards oxygen reduction electrocatalysts without high-temperature pyrolysis, Journal of Materials Chemistry 2012, 22, 6575.

[228] Y. Z. Liu, Y. F. Li, M. Zhong, Y. G. Yang, W. Yuefang, M. Z. Wang, A green and ultrafast approach to the synthesis of scalable graphene nanosheets with Zn powder for electrochemical energy storage, Journal of Materials Chemistry 2011, 21, 15449.

[229] C. Z. Zhu, S. J. Guo, Y. X. Fang, S. J. Dong, Reducing Sugar: New Functional Molecules for the Green Synthesis of Graphene Nanosheets, ACS Nano 2010, 4, 2429.

[230] X. B. Wang, H. Q. Tang, S. S. Huang, L. H. Zhu, Fast and facile microwave-assisted synthesis of graphene oxide nanosheets, RSC Advances 2014, 4, 60102.

[231] X. X. Liu, D. Zhan, D. L. Chao, B. C. Cao, J. H. Yin, J. P. Zhao, Y. Li, J. Y. Lin, Z. X. Shen, Microwave-assisted production of giant graphene sheets for high performance energy storage applications, Journal of Materials Chemistry A 2014, 2, 12166.

[232] S. Liu, Y. Zhu, J. Xie, Y. Huo, H. Y. Yang, T. Zhu, G. Cao, X. Zhao, S. Zhang, Direct Growth of Flower-Like δ-MnO_2 on Three-Dimensional Graphene for High-Performance Rechargeable Li-O_2 Batteries, Advanced Energy Materials 2014, 4, 1301960.

[233] P. Zhang, M. He, S. Xu, X. B. Yan, The controlled growth of porous δ-MnO_2 nanosheets on carbon fibers as a bi-functional catalyst for rechargeable lithium-oxygen batteries, Journal of Materials Chemistry A 2015, 3, 10811.

[234] J. Zhang, C. Guo, L. Zhang, C. M. Li, Direct growth of flower-like manganese oxide on reduced graphene oxide towards efficient oxygen reduction reaction, Chemical Communications 2013, 49, 6334.

[235] H. Xia, Y. Wang, J. Y. Lin, L. Lu, Hydrothermal synthesis of MnO_2/CNT nanocomposite with a CNT core/porous MnO_2 sheath hierarchy architecture for supercapacitors, Nanoscale Research Letters 2012, 7, 33.

[236] J. X. Li, N. Wang, Y. Zhao, Y. H. Ding, L. H. Guan, MnO_2 nanoflakes coated on multi-walled carbon nanotubes for rechargeable lithium-air batteries, Electrochemistry Communications 2011, 13, 698.

[237] Y. Qin, J. Lu, P. Du, Z. H. Chen, Y. Ren, T. P. Wu, J. T. Miller, J. G. Wen, D. J. Miller, Z. C. Zhang, In situ fabrication of porous-carbon-supported α-MnO_2 nanorods at room temperature: application for rechargeable Li-O_2 batteries, Energy & Environmental Science 2013, 6, 519.

[238] A. Zahoor, M. Christy, H. Jang, K. S. Nahm, Y. S. Lee, Increasing the reversibility of Li-O_2 batteries with caterpillar structured α-MnO_2/N–GNF bifunctional electrocatalysts, Electrochimica Acta 2015, 157, 299.

[239] Q. C. Liu, J. J. Xu, Z. W. Chang, X. B. Zhang, Direct electrodeposition of cobalt oxide nanosheets on carbon paper as free-standing cathode for Li-O_2 battery, Journal of Materials Chemistry A 2014, 2, 6081.

[240] B. W. Huang, L. Li, Y. J. He, X. Z. Liao, Y. S. He, W. Zhang, Z. F. Ma, Enhanced Electrochemical Performance of Nanofibrous CoO/CNF Cathode Catalyst for Li-O_2 Batteries, Electrochim. Acta 2014, 137, 183.

[241] F. Li, D.-M. Tang, T. Zhang, K. Liao, P. He, D. Golberg, A. Yamada, H. Zhou, Superior Performance of a Li-O_2 Battery with Metallic RuO_2 Hollow Spheres as the Carbon-Free Cathode, Advanced Energy Materials 2015, 1500294.

[242] D. A. Agyeman, K. Song, S. H. Kang, M. R. Jo, E. Cho, Y.-M. Kang, An improved catalytic effect of nitrogen-doped TiO_2 nanofibers for rechargeable Li-O_2 batteries; the role of oxidation states and vacancies on the surface, Journal of Materials Chemistry A 2015, 3, 22557.

[243] S. F. Tong, M. B. Zheng, Y. Lu, Z. X. Lin, J. Li, X. P. Zhang, Y. Shi, P. He, H. S. Zhou, Mesoporous NiO single-crystalline utilized as noble metal-free catalyst for non-aqueous Li-O_2 battery, Journal of Materials Chemistry A 2015, 3, 16177.

[244] A. C. Luntz, B. D. McCloskey, Nonaqueous Li-air batteries: a status report, Chemical Reviews 2014, 114, 11721.

[245] J. Xie, X. H. Yao, Q. M. Cheng, I. P. Madden, P. Dornath, C.-C. Chang, W. Fan, D. W. Wang, Three Dimensionally Ordered Mesoporous Carbon as a Stable, High-Performance Li-O_2 Battery Cathode, Angewandte Chemie International Edition 2015, 54, 1.

[246] F. J. Li, T. Zhang, H. S. Zhou, Challenges of non-aqueous Li-O_2 batteries: electrolytes, catalysts, and anodes, Energy & Environmental Science 2013, 6, 1125.

[247] F. Y. Cheng, J. Chen, Metal-air batteries: from oxygen reduction electrochemistry to cathode catalysts, Chemical Society Reviews 2012, 41, 2172.

[248] M. M. Ottakam Thotiyl, S. A. Freunberger, Z. Peng, P. G. Bruce, The Carbon Electrode in Nonaqueous Li-O_2 Cells, Journal of the American Chemical Society 2013, 135, 494.

[249] M. Balaish, A. Kraytsberg, Y. Ein-Eli, A critical review on lithium-air battery electrolytes, Physical Chemistry Chemical Physics 2014, 16, 2801.

[250] H. G. Jung, J. Hassoun, J. B. Park, Y. K. Sun, B. Scrosati, An improved high-performance lithium-air battery, Nature Chemistry 2012, 4, 579.

[251] W.-J. Kwak, K. C. Lau, C.-D. Shin, K. Amine, L. A. Curtiss, Y.-K. Sun, A Mo_2C/Carbon Nanotube Composite Cathode for Lithium Oxygen Batteries with High Energy Efficiency and Long Cycle Life, ACS Nano 2015, 9, 4129.

[252] M. Lu, J. Qu, Q. Yao, C. Xu, Y. Zhan, J. Xie, J. Y. Lee, Exploring Metal Nanoclusters for Lithium-Oxygen Batteries, ACS Applied Materials & Interfaces 2015, 7, 5488.

[253] Y. Chen, F. J. Li, D. M. Tang, Z. L. Jian, C. Liu, D. Golberg, A. Yamada, H. S. Zhou, Multi-walled carbon nanotube papers as binder-free cathodes for large capacity and reversible non-aqueous Li-O_2 batteries, Journal of Materials Chemistry A 2013, 1, 13076.

[254] E. Yoo, H. S. Zhou, Li-Air Rechargeable Battery Based on Metal-free Graphene Nanosheet Catalysts, ACS Nano 2011, 5, 3020.

[255] J. Li, H. M. Zhang, Y. N. Zhang, M. R. Wang, F. X. Zhang, H. J. Nie, A hierarchical porous electrode using a micron-sized honeycomb-like carbon material for high capacity lithium-oxygen batteries, Nanoscale 2013, 5, 4647.

[256] Z. L. Wang, D. Xu, J. J. Xu, X. B. Zhang, Oxygen electrocatalysts in metal-air batteries: from aqueous to nonaqueous electrolytes, Chemical Society Reviews 2014, 43, 7746.

[257] X. P. Han, Y. X. Hu, J. G. Yang, F. Y. Cheng, J. Chen, Porous perovskite $CaMnO_3$ as an electrocatalyst for rechargeable Li-O_2 batteries, Chemical Communications 2014, 50, 1497.

[258] J. Park, Y.-S. Jun, W.-r. Lee, J. A. Gerbec, K. A. See, G. D. Stucky, Bimodal Mesoporous Titanium Nitride/Carbon Microfibers as Efficient and Stable Electrocatalysts for Li-O_2 Batteries, Chemistry of Materials 2013, 25, 3779.

[259] K. J. Zhang, L. X. Zhang, X. Chen, X. He, X. G. Wang, S. M. Dong, L. Gu, Z. H. Liu, C. H. Huang, G. L. Cui, Molybdenum nitride/N-doped carbon nanospheres for lithium-O_2 battery cathode electrocatalyst, ACS Applied Materials & Interfaces 2013, 5, 3677.

[260] Y. C. Lu, Z. C. Xu, H. A. Gasteiger, S. Chen, K. Hamad-Schifferli, Y. Shao-Horn, Platinum-Gold Nanoparticles: A Highly Active Bifunctional Electrocatalyst for Rechargeable Lithium-Air Batteries, Journal of the American Chemical Society 2010, 132, 12170.

[261] J. Lu, L. Cheng, K. C. Lau, E. Tyo, X. Y. Luo, J. G. Wen, D. Miller, R. S. Assary, H. H. Wang, P. Redfern, H. M. Wu, J. B. Park, Y. K. Sun, S. Vajda, K. Amine, L. A. Curtiss, Effect of the size-selective silver clusters on lithium peroxide morphology in lithium-oxygen batteries, Nature Communications 2014, 5, 4895.

[262] X. Huang, H. Yu, H. Tan, J. Zhu, W. Zhang, C. Wang, J. Zhang, Y. Wang, Y. Lv, Z. Zeng, D. Liu, J. Ding, Q. Zhang, M. Srinivasan, P. M. Ajayan, H. H. Hng, Q. Yan, Carbon Nanotube-Encapsulated Noble Metal Nanoparticle Hybrid as a Cathode Material for Li-Oxygen Batteries, Advanced Functional Materials 2014, 24, 6516.

[263] D. Zhu, L. Zhang, M. Song, X. F. Wang, Y. G. Chen, An in situ formed Pd nanolayer as a bifunctional catalyst for Li-air batteries in ambient or simulated air, Chemical Communications 2013, 49, 9573.

[264] A. K. Thapa, Y. Hidaka, H. Hagiwara, S. Ida, T. Ishihara, Mesoporous β-MnO_2 Air Electrode Modified with Pd for Rechargeability in Lithium-Air Battery, Journal of The Electrochemical Society 2011, 158, A1483.

[265] Y. Lei, J. Lu, X. Y. Luo, T. P. Wu, P. Du, X. Y. Zhang, Y. Ren, J. G. Wen, D. J. Miller, J. T. Miller, Y. K. Sun, J. W. Elam, K. Amine, Synthesis of Porous Carbon Supported Palladium Nanoparticle Catalysts by Atomic Layer Deposition: Application for Rechargeable Lithium-O_2 battery, Nano Letters 2013, 13, 4182.

[266] G. Q. Zhang, J. P. Zheng, R. Liang, C. Zhang, B. Wang, M. Hendrickson, E. J. Plichta, Lithium-Air Batteries Using SWNT/CNF Buckypapers as Air Electrodes, Journal of The Electrochemical Society 2010, 157, A953.

[267] S. H. Park, W. J. Lee, Hierarchically mesoporous CuO/carbon nanofiber coaxial shell-core nanowires for lithium ion batteries, Scientific Reports 2015, 5, 9754.

[268] C. Alegre, E. Modica, C. Lo Vecchio, D. Sebastián, M. J. Lázaro, A. S. Aricò, V. Baglio, Carbon Nanofibers as Advanced Pd Catalyst Supports for the Air Electrode of Alkaline Metal-Air Batteries, ChemPlusChem 2015, 80, 1384.

[269] X. L. Ji, K. T. Lee, R. Holden, L. Zhang, J. J. Zhang, G. A. Botton, M. Couillard, L. F. Nazar, Nanocrystalline intermetallics on mesoporous carbon for direct formic acid fuel cell anodes, Nature Chemistry 2010, 2, 286.

[270] J. G. Li, C. Y. Tsai, S. W. Kuo, Fabrication and Characterization of Inorganic Silver and Palladium Nanostructures within Hexagonal Cylindrical Channels of Mesoporous Carbon, Polymers 2014, 6, 1794.

[271] Z. Y. Guo, D. D. Zhou, X. L. Dong, Z. J. Qiu, Y. G. Wang, Y. Y. Xia, Ordered hierarchical mesoporous/macroporous carbon: a high-performance catalyst for rechargeable Li-O_2 batteries, Advanced Materials 2013, 25, 5668.

[272] L. Qie, W. M. Chen, Z. H. Wang, Q. G. Shao, X. Li, L. X. Yuan, X. L. Hu, W. X. Zhang, Y. H. Huang, Nitrogen-Doped Porous Carbon Nanofiber Webs as Anodes for Lithium Ion Batteries with a Superhigh Capacity and Rate Capability, Advanced Materials 2012, 24, 2047.

[273] Z. R. Ismagilov, A. E. Shalagina, O. Y. Podyacheva, A. V. Ischenko, L. S. Kibis, A. I. Boronin, Y. A. Chesalov, D. I. Kochubey, A. I. Romanenko, O. B. Anikeeva, T. I. Buryakov, E. N. Tkachev, Structure and electrical conductivity of nitrogen-doped carbon nanofibers, Carbon 2009, 47, 1922.

[274] Y. H. Xue, J. Liu, H. Chen, R. G. Wang, D. Q. Li, J. Qu, L. M. Dai, Nitrogen-Doped Graphene Foams as Metal-Free Counter Electrodes in High-Performance Dye-Sensitized Solar Cells, Angewandte Chemie International Edition 2012, 51, 12124.

[275] R. Mi, S. M. Li, X. C. Liu, L. M. Liu, Y. C. Li, J. Mei, Y. G. Chen, H. Liu, H. Wang, H. Yan, W.-M. Lau, Electrochemical performance of binder-free carbon nanotubes with different nitrogen amounts grown on the nickel foam as cathodes in Li-O_2 batteries, Journal of Materials Chemistry A 2014, 2, 18746.

[276] L. Perini, C. Durante, M. Favaro, V. Perazzolo, S. Agnoli, O. Schneider, G. Granozzi, A. Gennaro, Metal-Support Interaction in Platinum and Palladium Nanoparticles Loaded on Nitrogen Doped Mesoporous Carbon for Oxygen Reduction Reaction, ACS Applied Materials & Interfaces 2015, 7, 1170.

[277] Z. Zhang, L. W. Su, M. Yang, M. Hu, J. Bao, J. P. Wei, Z. Zhou, A composite of Co nanoparticles highly dispersed on N-rich carbon substrates: an efficient electrocatalyst for Li-O_2 battery cathodes, Chemical Communications 2014, 50, 776.

[278] J. T. Zhang, Z. H. Zhao, Z. H. Xia, L. M. Dai, A metal-free bifunctional electrocatalyst for oxygen reduction and oxygen evolution reactions, Nature Nanotechnology 2015, 10, 444.

[279] T. Sharifi, G. Z. Hu, X. E. Jia, T. Wågberg, Formation of Active Sites for Oxygen Reduction Reactions by Transformation of Nitrogen Functionalities in Nitrogen-Doped Carbon Nanotubes, ACS Nano 2012, 6, 8904.

[280] Y. Zhao, C. G. Hu, L. Song, L. X. Wang, G. Q. Shi, L. M. Dai, L. T. Qu, Functional graphene nanomesh foam, Energy & Environmental Science 2014, 7, 1913.

[281] M. M. Storm, M. Overgaard, R. Younesi, N. E. A. Reeler, T. Vosch, U. G. Nielsen, K. Edström, P. Norby, Reduced graphene oxide for Li-air batteries: The effect of oxidation time and reduction conditions for graphene oxide, Carbon 2015, 85, 233.

[282] S. D. Yang, J. Dong, Z. H. Yao, C. M. Shen, X. Z. Shi, Y. Tian, S. X. Lin, X. G. Zhang, One-Pot Synthesis of Graphene-Supported Monodisperse Pd Nanoparticles as Catalyst for Formic Acid Electro-oxidation, Scientific Reports 2014, 4, 4501.

[283] H. Meng, F. Y. Xie, J. Chen, P. K. Shen, Electrodeposited palladium nanostructure as novel anode for direct formic acid fuel cell, Journal of Materials Chemistry A 2011, 21, 11352.

[284] L. Qie, W. M. Chen, H. H. Xu, X. Q. Xiong, Y. Jiang, F. Zou, X. L. Hu, Y. Xin, Z. L. Zhang, Y. H. Huang, Synthesis of functionalized 3D hierarchical porous carbon for high-performance supercapacitors, Energy & Environmental Science 2013, 6, 2497.

[285] K. Sakaushi, S. J. Yang, T. P. Fellinger, M. Antonietti, Impact of large-scale meso- and macropore structures in adenosine-derived affordable noble carbon on efficient reversible oxygen electrocatalytic redox reactions, Journal of Materials Chemistry A 2015, 11720.

[286] I.-Y. Jeon, S. Zhang, L. Zhang, H.-J. Choi, J.-M. Seo, Z. Xia, L. Dai, J.-B. Baek, Edge-Selectively Sulfurized Graphene Nanoplatelets as Efficient Metal-Free Electrocatalysts for Oxygen Reduction Reaction: The Electron Spin Effect, Advanced Materials 2013, 25, 6138.

[287] N. A. Al Abass, G. Denuault, D. Pletcher, The unexpected activity of Pd nanoparticles prepared using a non-ionic surfactant template, Physical Chemistry Chemical Physics 2014, 16, 4892.

[288] S. Chen, J. J. Duan, M. Jaroniec, S. Z. Qiao, Three-Dimensional N-Doped Graphene Hydrogel/NiCo Double Hydroxide Electrocatalysts for Highly Efficient Oxygen Evolution, Angewandte Chemie International Edition 2013, 52, 13567.

[289] Y. Zhao, R. Nakamura, K. Kamiya, S. Nakanishi, K. Hashimoto, Nitrogen-doped carbon nanomaterials as non-metal electrocatalysts for water oxidation, Nature Communications 2013, 4, 2309.

[290] J. W. D. Ng, M. Tang, T. F. Jaramillo, A carbon-free, precious-metal-free, high-performance O_2 electrode for regenerative fuel cells and metal-air batteries, Energy & Environmental Science 2014, 7, 2017.

[291] S. Y. Wang, D. S. Yu, L. M. Dai, Polyelectrolyte Functionalized Carbon Nanotubes as Efficient Metal-free Electrocatalysts for Oxygen Reduction, Journal of the American Chemical Society 2011, 133, 5182.

[292] I.-Y. Jeon, H.-J. Choi, M. Choi, J.-M. Seo, S.-M. Jung, M.-J. Kim, S. Zhang, L. P. Zhang, Z. H. Xia, L. M. Dai, N. Park, J.-B. Baek, Facile, scalable synthesis of edge-halogenated graphene nanoplatelets as efficient metal-free eletrocatalysts for oxygen reduction reaction, Scientific Reports 2013, 3, 1810.

[293] K. P. Gong, F. Du, Z. H. Xia, M. Durstock, L. M. Dai, Nitrogen-Doped Carbon Nanotube Arrays with High Electrocatalytic Activity for Oxygen Reduction, Science 2009, 323, 760.

[294] M. Wang, J. Z. Wang, Y. Y. Hou, D. Q. Shi, D. Wexler, S. D. Poynton, R. C. Slade, W. M. Zhang, H. K. Liu, J. Chen, N-doped crumpled graphene derived from vapor phase deposition of PPy on graphene aerogel as an efficient oxygen reduction reaction electrocatalyst, ACS Applied Materials & Interfaces 2015, 7, 7066.

[295] K. P. C. Yao, D. G. Kwabi, R. A. Quinlan, A. N. Mansour, A. Grimaud, Y.-L. Lee, Y. C. Lu, Y. Shao-Horn, Thermal Stability of Li_2O_2 and Li_2O for Li-Air Batteries: In Situ XRD and XPS Studies, Journal of The Electrochemical Society 2013, 160, A824.

[296] F. F. Tu, J. Xie, S. C. Zhang, G. S. Cao, T. J. Zhu, X. B. Zhao, Mushroom-like Au/$NiCo_2O_4$ nanohybrids as high-performance binder-free catalytic cathodes for lithium-oxygen batteries, Journal of Materials Chemistry A 2015, 3, 5714.

[297] D. Y. Kim, M. Kim, D. W. Kim, J. Suk, O. O. Park, Y. Kang, Flexible binder-free graphene paper cathodes for high-performance Li-O_2 batteries, Carbon 2015, 93, 625.

[298] Z. Zhang, J. Bao, C. He, Y. N. Chen, J. P. Wei, Z. Zhou, Hierarchical Carbon-Nitrogen Architectures with Both Mesopores and Macrochannels as Excellent Cathodes for Rechargeable Li-O_2 Batteries, Advanced Functional Materials 2014, 24, 6826.

[299] J.-H. Kim, A. G. Kannan, H.-S. Woo, D.-G. Jin, W. Kim, K. Ryu, D.-W. Kim, A bi-functional metal-free catalyst composed of dual-doped graphene and mesoporous carbon for rechargeable lithium-oxygen batteries, Journal of Materials Chemistry A 2015, 3, 18456.

APPENDIX A: LIST OF PUBLICATIONS

1*. **J. Wang**, J. Z. Wang, Z. Q. Sun, X. W. Gao, C. Zhong, S. L. Chou, and H. K. Liu, A germanium/single-walled carbon nanotube composite paper as a free-standing anode for lithium-ion batteries, Journal of Materials Chemistry A, 2014, 2, 4613. (IF: 7.443)

2*. **J. Wang**, C. Q. Feng, Z. Q. Sun, S. L. Chou, H. K. Liu, and J. Z. Wang, In-situ one-step hydrothermal synthesis of a lead germanate-graphene composite as a novel anode material for lithium-ion batteries, Scientific Reports, 2014, 4, 7030. (IF: 5.578)

3*. **J. Wang**, L.L. Liu, C. M. Subramaniyam, S. L Chou, H. K. Liu, and J. Z. Wang, A Microwave Autoclave Synthesized δ-MnO_2 /Graphene Composite as a Cathode Material for Lithium-Oxygen Batteries, Journal of Applied Electrochemistry, 2016, DOI: 10.1007/s10800-016-0956-y. (IF: 2.41)

4*. **J. Wang**, L. L. Liu, S. L. Chou, H. K. Liu, and J. Z. Wang, A 3D Porous Nitrogen-Doped Carbon-Nanofiber-Supported Palladium Composite as a Cathode Material for Lithium-Oxygen Batteries. (Submitted to Nano Letters)

5. L. L. Liu, Y. Y. Hou, **J. Wang**, J. Chen, H. K. Liu, Y. P. Wu and J. Z. Wang, Nanofibrous Co_3O_4/PPy Hybrid with Synergistic Effect as Bifunctional Catalyst for Lithium-Oxygen Batteries, Advanced Materials Interfaces, 2016, DOI: 10.1002/admi.201600030. (IF: Pending)

6. L. L. Liu, **J. Wang**, Y. Y. Hou, J. Chen, H. K. Liu, J. Z. Wang, and Y. P. Wu, Self-assembled 3D foam-like $NiCo_2O_4$ prepared from a green starch template as efficient catalyst for lithium oxygen batteries, Small, 2016, 12, 602. (IF: 8.368)

7. B. Y. Ruan, **J. Wang**, D. Q. Shi, Y. F. Xu, S. L. Chou, H. K. Liu, and J. Z. Wang, Phosphorus/N-doped carbon nanofiber composite as anode material for sodium-ion batteries, Journal of Materials Chemistry A, 2015, 3, 19011. (IF: 7.443)

8. L. Lin, C. Q. Feng, Z. Hao, **J. Wang**, J. Z. Wang, and P. X. He, Synthesis and electrochemical properties of $Li[Ni_{1/3}Co_{1/3}Mn_{1/3}]O_2$ for lithium ion batteries, Science of Advanced Materials, 2015, 7, 1. (IF: 2.598)

9. H. Zheng, S. Q. Wang, J. Z. Wang, **J. Wang**, L. Li, Y. Yang, C. Q. Feng, and Z. Q. Sun, 3D $Fe_2(MoO_4)_3$ microspheres with nanosheet constituents as high-capacity anode materials for lithium-ion batteries, Journal of Nanoparticle Research, 2015, 17, 449. (IF: 2.184)

10. L. L. Zhao, X. L. Wang, F. F. Yun, J. Y. Wang, Z. X. Cheng, S. X. Dou, **J. Wang**, and G. Jeffrey Snyder, High thermoelectric and mechanical performance in highly dense $Cu_{2-x}S$ bulks prepared by a melt-solidification technique, Journal of Materials Chemistry A, 2015, 3, 9432. (IF: 7.443)

11. L. L. Zhao, X. L. Wang, J. Y. Wang, Z. X. Cheng, S. X. Dou, **J. Wang**, and L. Q. Liu, Superior intrinsic thermoelectric performance with *zT* of 1.8 in single-crystal and melt-quenched highly dense $Cu_{2-x}Se$ bulks, Scientific Reports, 2015, 5, 7671. (IF: 5.578)

12. L. L. Zhao, X. L. Wang, J. Y. Wang, Z. X. Cheng, **J. Wang**, N. Yin, Z. G. Gai, A. Jalalian, and S. X. Dou, Cobalt doping effects on photoluminescence, Raman scattering, crystal structure, and magnetic and piezoelectric properties in ZnO single crystals grown from molten hydrous LiOH and NaOH solutions, Journal of Alloys and Compounds, 2015, 628, 303. (IF: 2.999)

13. L. L. Zhao, X. L. Wang, F. F. Yun, J. Y. Wang, Z. X. Cheng, S. X. Dou, **J. Wang**, and G. Jeffrey Snyder, The effects of Te^{2-} and I^- substitutions on the electronic structures, thermoelectric performance, and hardness in melt-quenched highly dense $Cu_{2-x}Se$, Advanced Electronic Materials, 2015, 1, 1400015. (IF: Pending)

14. R M Kottegoda, X. W. Gao, L. D C Nayanajith, C. H Manorathne, J. Wang, and Jiazhao Wang, Comparison of few-layer graphene prepared from natural graphite through

fast synthesis approach, Journal of Materials Science & Technology, 2015, 31, 907. (IF: 2.999)

Papers listed are all during PhD study. Impact factor (IF) is from 2014.

The publications with an asterisk mark are exclusively related to this thesis.